

Modelling of High Strain Rate Plasticity and Metal Cutting

Dan Wedberg



Modelling of high strain rate plasticity and metal cutting

Dan Wedberg

Luleå University of Technology
Department of Engineering Sciences and Mathematics
Division of Mechanics of Solid Materials

Printed by Universitetstryckeriet, Luleå 2013

ISSN: 1402-1544

ISBN 978-91-7439-670-6 (print)

ISBN 978-91-7439-671-3 (pdf)

Luleå 2013

www.ltu.se

Abstract

Metal cutting is one of the most frequently used forming processes in the manufacturing industry. Extensive effort is made to improve its process and simulation has become an integrated part, not only in the product development process but also in the customer relations. However, simulation of metal cutting is complex both from numerical as well as physical point of view. Furthermore, modelling the material behaviour has shown to be crucial. Errors in the material model cannot be reduced by the numerical procedures. The magnitudes of strain and strain rate involved in metal cutting may reach values of 1-10 and 10^3 - 10^6 s⁻¹. The dissipative plastic work together with the chip tool friction also leads to locally high temperatures. These extreme ranges of conditions imply that a diversity of physical phenomena is involved and it is a challenge to develop a material model with adequate accuracy over the whole loading range. Furthermore, this intense and severe deformation represents thermo-mechanical behaviour far from what is generated from conventional material compression and tension testing. A highly desirable feature is also a material model that can be extrapolated outside the calibration range. This is not trivial since materials exhibit different strain hardening and softening characteristics at different strains, strain rates and temperatures. Models based on modelling some aspects of the underlying physical process, e.g. the generation of dislocations, are expected to have a larger range of validity than engineering models. Though, engineering models are the far most common models used in metal cutting simulations.

The scope of this work includes development of validated models for metal cutting simulations of AISI 316L stainless steel. Particular emphasis is placed on the material modeling and high strain rate plasticity phenomena. The focus has been on a physically based material model. The approach has been to review the literature about flow stress models and phenomena and particularly at high strain rates. A previous variant of a dislocation density model has thereafter been extended into high strain rate regimes by applying different mechanisms. Some of the models have been implemented in commercial finite element software for orthogonal cutting simulations. Experimental measurements and evaluations that include SHPB-measurements, cutting force measurements, quick-stop measurements and some microstructural examinations has been conducted for calibration and validation. The compression tests, within a temperature and strain rate range of 20-950 °C and 0.01-9000 s⁻¹ respectively, showed that the flow stress increased much more rapidly within the dynamic loading range and hence depends on the strain rate. The dynamic strain aging (DSA) that has been observed at lower strain rates is non-existent at higher strain rates. The temperature and strain-rate evolution is such that the DSA is not necessary to include when modelling this process. Furthermore the magnetic balance measurements indicate that the martensite transformation-strengthening effect is insignificant within the dynamic loading range. In the present work the concept of motion of dislocations, their resistance to motion and substructure evolution are used as underlying motivation for description of the flow stress. A coupled set of evolution equations for dislocation density and mono vacancy concentration is used rendering a formulation of a rate-dependent yield limit in context of rate-independent plasticity. Dislocation drag due to phonon and electron drag, a strain rate dependent model of the subcell formation, a strain rate and temperature dependent recovery function and a structural dependent thermally activated stress component have among others been considered. Best predictability was obtained with a strain rate dependent subcell formulation. Dislocation drag did not improve the predictability within the measured testing range. Although showed to have a greater influence outside the range of calibration when extrapolated. It has been shown that extrapolation is uncertain. Results from experiments and modelling of material behaviour and metal cutting together with the literature indicate that the predictability of the material behaviour within and outside the measured testing range can be further tuned by implementing models of the phenomenon mechanical twinning and recrystallization.

Keywords: Metal cutting, SHPB, FE-simulation, constitutive modelling, dislocation density model, high strain rate, 316L stainless steel.

List of appended papers

This thesis consists of an introduction and the following appended papers:

Paper A

Lindgren L.-E., D. Wedberg and A. Svoboda, *Verification and validation of machining simulations for sufficient accuracy*, International Conference on Computational Plasticity, 2009.

Paper B

Svoboda A., D. Wedberg and L.-E. Lindgren, *Simulation of metal cutting using a physically based plasticity model*, Modelling and Simulation in Materials Science and Engineering, 2010, **18**: p.1-19.

Paper C

Kalhari V., D. Wedberg and L.-E. Lindgren, *Simulation of mechanical cutting using a physical based material model*, International Journal of Material Forming, 2010, **3**: p.511-514.

Paper D

Wedberg D. and L.-E. Lindgren, *Predictive capability of constitutive model outside the range of calibration*, International Conference on Computational Plasticity, 2011.

Paper E

Wedberg D., A. Svoboda and L.-E. Lindgren, *Modelling high strain rate phenomena in metal cutting simulation*, Modelling and Simulation in Materials Science and Engineering, 2012, **20**: p.1-19.

Paper F

Wedberg D. and L.-E. Lindgren, *Modelling flow stress of AISI 316L at high strain rates*.

Preface

This work has been carried out at AB Sandvik Coromant and at Luleå University of Technology with Professor Lars-Erik Lindgren as supervisor and PhD Ales Svoboda as co-supervisor. The financial support was provided by the Swedish Research Council and AB Sandvik Coromant and is gratefully acknowledged. It is highly appreciated to have been giving the opportunity to work with this research project. Thank you all who have been involved and enabled this.

This summary is organized in 13 chapters. The reader will notice that the summary has become unusual long. However, a number of years have passed and a large amount of literature has been looked through. I found it useful for the learning process as well as good for future researches in this area to sum up some of this literature. Though, some topics are considered more deeply while others are only considered superficially.

There are many people who in one way or another have contributed to the work of this thesis. To mention everyone is hardly possible, but I wish to express my gratitude to all of you who contributed. However, there are some people to whom I especially would like to express my thanks. First of all I want to thank my supervisor Professor Lars-Erik Lindgren for his enthusiasm, support and friendship during this work. Then I would like to thank my co-authors PhD Ales Svoboda and PhD Vahid Kalhori. Many interesting discussions have taken place. I would also like to thank Professor Veli-Tapani Kuokkala and his research group at the Tampere University of Technology. Special thanks to M.Sc Jari Rämö for good collaboration and sharing of knowledge and experience around the Split-Hopkinson. Also, many thanks to Mikael Lundblad, manager metal cutting research at AB Sandvik Coromant, for the understanding and persistent waiting for me to complete this work. Thanks also to PhD John Ion for linguistic revision of paper E. I also wish to thank the PhD-student Bijish Babu, who like me has an interest in material behaviour and modelling, for meaningful discussions and sharing of knowledge.

Before finishing these lines, I would like to thank my beloved wife Ulrika for her love and patience during this work.

Dan Wedberg

Graz, April 2013

Table of Contents

Introduction	1
1.1 Scope of this work	2
Mechanics of metal cutting	3
2.1 Cutting forces	4
2.2 Tool and chip interaction	5
2.3 Heat generation in metal cutting	6
2.4 Chip formation	6
Stainless steels	8
3.1 Ferritic stainless steels	9
3.2 Martensitic stainless steels	9
3.3 Austenitic-ferritic stainless steels	9
3.4 Precipitation hardening stainless steels	10
3.5 Austenitic stainless steels	10
Plastic behaviour of solid polycrystals	11
4.1 Defects in solid polycrystals	11
4.1.1 Point defects	12
4.1.2 Line defects	12
4.1.3 Planar defects	13
4.2 Deformation mechanism	13
4.2.1 Deformation by slip and climb of dislocations	14
4.2.2 Deformation by twinning	16
4.2.3 Deformation via martensite transformation	17
4.3 Intersection of dislocations	19
4.4 Consequences of the deformation mechanisms	20
4.4.1 Hardening	20
4.4.2 Softening	21
Strengthening at high strain rates	23
5.1 Dislocation drag	23
5.2 Strain rate effects on dislocation substructure	25
5.3 Strain rate effects on martensitic transformation	27
5.3.1 Martensitic transformation in AISI 316L	28
5.4 Strain rate effects on twinning	28
5.4.1 Twin formation in AISI 316L	30
Constitutive material models	31
6.1 Engineering models	31
6.2 Physically based models	33
Dislocation density based model	34
7.1 Flow stress	34
7.2 Evolution of immobile dislocation density	37
7.2.1 Hardening	37
7.2.2 Recovery	38

7.2.3	Generation and migration of vacancies	38
7.2.4	Diffusion of solutes	39
7.3	Stress update algorithm	40
Determination of mechanical properties at high strain rates		42
8.1	Expanding ring test	43
8.2	Taylor impact tests	44
8.3	Machining tests	44
8.4	Split-Hopkinson	44
8.4.1	Split Hopkinson - One dimensional wave equation	46
8.4.2	Dispersion effects and corrections to the one-dimensional wave equation	48
8.4.3	Geometric constraints on dimensions of test specimen in SPHB	50
Distribution of work and summary of appended papers		52
9.1	Paper A	52
9.2	Paper B	53
9.3	Paper C	53
9.4	Paper D	53
9.5	Paper E	54
9.6	Paper F	54
Results		56
10.1	Results – material testing experiments	56
10.2	Results – material modelling	60
10.3	Results – simulation of metal cutting	64
10.4	Results – sufficient accuracy of models	66
Conclusions		68
Future work		69
References		70

Chapter 1

Introduction

Metal cutting is one of the most commonly occurring manufacturing processes within the industry to produce components based on specific requirements. Demand for new products with increased customer value in terms of accessibility, quality, productivity and profitability along with demands for a shorter time to market has led to that simulation are given a central role in product development cycle. However, simulation of metal cutting has shown to be far from trivial. Metal cutting is a chip-forming process that is complex in its nature. The chip is formed under severe and rapid deformation in combination with increased temperature due to plastic dissipated energy and friction from the workpiece/tool contacts. An overview of typical strains and strain rates in different manufacturing process by Guo (2003) showed that the strains and the strain rates in metal cutting may reach values of 1-10 and 10^3 - 10^6 s⁻¹ respectively. Furthermore the homologous temperature (T/T_m) may reach values of 0.16-0.9. These extreme ranges of conditions indicate that simulation of metal cutting is complex both in terms of numeric and physics. Hence, the simulation model must handle physical phenomenon as large elasto-plastic deformation under rapid process, thermo-mechanical coupling, microstructural changes, nontrivial interface between chip and tool and chip formation mechanisms. It follows that the material model must be able to adequately represent the deformation behaviour as hardening and softening under a great range of strains, strain rates and temperatures. Correct description of material behaviour is therefore crucial for simulation of metal cutting in order of reliable results for prediction of chip shape, cutting forces, temperature distribution, wear, and surface integrity including residual stresses.

There exist a large number of different material models and many are designed to take into account various phenomena in different length and time scale. Though, material models can be divided into empirical and physically based material models. Empirical models do not take the underlying physical phenomena in account. Equations and parameters are adapted to experimental data by curve fitting. Johnson & Cook power law model is one of the most frequently used models for description of material behaviour in simulation of metal cutting. Physical models are on the other hand models based on knowledge of the underlying physical phenomena and are expected to have a larger domain of validity. This is necessary for simulation of metal cutting where strains, strain rates and temperatures vary over a wide range.

Plastic deformation of crystalline metals may occur by different mechanisms and is complex when considering all the different physical processes involved. Slip is the most common dominating deformation mechanism where the plastic flow is governed by the motion of dislocations, Hull and Bacon (2001). Results from experimental tests in the literature reveal that the stress increases slowly with the logarithm of strain rate for low strain rates up to about 1000 s⁻¹. A marked increase in the stress and the strain rate sensitivity has however been

noticed in excess of approximately 1000 s^{-1} , Regazzoni *et al.* (1987). This change in rate dependency may be attributed to a change of rate controlling mechanisms. The most common explanation is that dislocation drag becomes dominant. This example illustrates that a model based on a given physics cannot be stretched to a larger strain rates without adding the relevant mechanism. However, it is expected to be valid outside its calibration range provided the mechanisms it has been calibrated for are still dominating.

Characterization of the mechanical behaviour of metals and alloys are important because of the interplay between modelling, theory and experiments. Characterization of thermo-mechanical properties can be done by different methods and machines. Conventional testing with screw or servo hydraulic machines are mainly used for quasi-static tests in strain rates range 10^{-4} - 1 s^{-1} , Hokka (2008), while the Taylor test, the Split Hopkinson pressure bar (SHPB) test and the expanding ring test are used for high strain rates. The most widely used test method for high strain rates is SHPB.

1.1 Scope of this work

The aim of this work is to develop validated models for metal cutting simulations. Particular emphasis is placed on the material modelling, which is crucial for metal cutting simulations. The material model affects the computed cutting forces and even more the chip formation. The focus has been on use of physical based material models. The current work has been limited to a stainless steel, AISI 316L, although the models can be calibrated for other metals and alloys. The approach has been to review the literature about flow stress models and phenomena and particularly at high strain rates. Furthermore, experimental work has been done to calibrate and validate material models. Experiments have also been performed on orthogonal cutting in order to validate the metal cutting models.

Chapter 2

Mechanics of metal cutting

Metal cutting occurs frequently within the manufacturing industry and can be regarded as the most common and widely used machining operations. The main objective of metal cutting can be described by generation of newly created work surface through removal of unwanted material by a chip removal process. Several industrial applications of metal cutting exist for e.g. turning, milling and drilling. However the principal of metal cutting is the same regardless of application. Generally, a wedge-shaped tool with a cutting edge is moving relative a workpiece material with an overlap. The material that flows towards the cutting edge is instantaneous forced to change flow direction and forming a chip. The wedge-shaped tool consists basically of a tool face (rake face) along which the created chip flows and a flank on the other side of the cutting edge. However, various micro-geometric designs exist. The positioning of the cutting edge is described in relation to the movement of the cutting tool. When the cutting edge is perpendicular to the movement of the tool orthogonal cutting is performed. Otherwise the metal cutting is referred to as oblique cutting, see Figure 2.1.

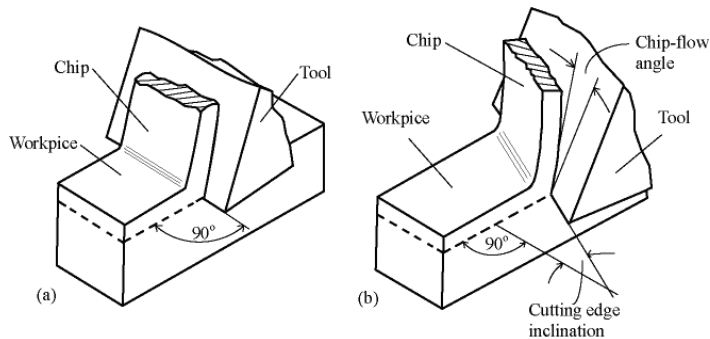


Figure 2.1 – a) Orthogonal and b) oblique cutting, from Boothroyd and Winston (2006).

Earlier theories assumed that the chip formation was due to a crack in front of the cutting edge, which separated the chip from the workpiece material like in splitting of wood Boothroyd and Winston (2006) and Moore (1975). However it is well recognized today that fundamentals of chip formation are restricted to the two major deformations zones referred to as the primary deformation zone and the secondary deformation zone, see Figure 2.2. The former region extends from the cutting edge of the cutting tool to the transition between the work-piece material and the chip. When work-piece material enters this region it is forced to instantaneous change direction. The material undergoes severe shear plastic straining under

high strain rates and the heat generated due to plastic deformation will all together influence supremely the behaviour of the work-piece material. Hardening and softening will interact. The secondary deformation zone occurs at the interface between the tool face and the chip and is oriented behind the primary deformation zone. Hence, the work-piece material is first deformed in the primary zone and then in the secondary zone. The heat in secondary zone is generated through plastic deformation but also through friction. Hence, the maximum temperature occurs along the tool face and usually in the sliding region. Since the heat transfer depends on the cutting velocity the time for heat conduction is insignificant except at very low cutting speeds and adiabatic conditions are usually assumed, Vaz *et al.* (2007).

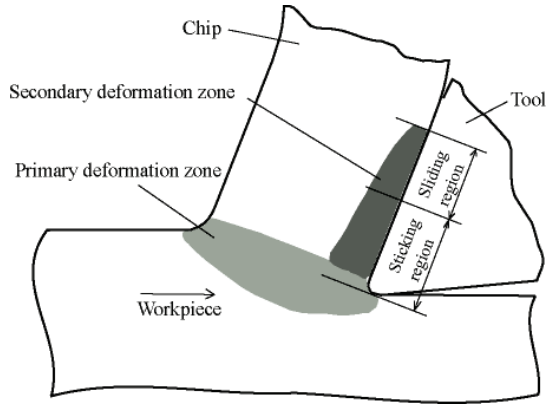


Figure 2.2 – Definition of the primary and secondary deformation zone.

Metal cutting can be said to be a chip-formation process and it is not hard to imagine that the geometry of the wedge-shaped tool, the properties of the insert including the coatings, the cutting process parameter and the workpiece material have a great impact on the behaviour of the system. Hence, understanding of the metal removing process are important to successively develop new cutting tools as well as utilizing the cutting tool in order to meet the requirements on surface integrity, dimensional accuracy and production efficiency. This section aims to introduce the basic of metal cutting.

2.1 Cutting forces

Cutting forces have a great impact on the cutting system and are therefore of great interest. For e.g. cutting forces causes deflections and provide energy to the cutting system which in turn may raise the cutting temperature and/or excite one of the structural modes of the system causing vibrations. The latter may be detrimental for the cutting tool and the machined surface. The cutting speed, the feed and the tool angles are some important factors that influence the cutting forces, Kalhori (2001), Vaz *et al.* (2007) and Saoubi *et al.* (1999).

The acting force on the cutting tool during the cutting process is distributed over the chip-workpiece-cutting tool contact area and may for a turning lathe commonly be divided into three force components, cutting force F_c , feed force F_f and a force in the radial direction. The latter is the smallest of the force components and strive to push the cutting tool outwards in the radial directions. The largest force component is usually the cutting force which acts in the same direction as the cutting velocity. The feed force acts in the direction of the feed. Figure 2.3 shows the orientation of the forces.

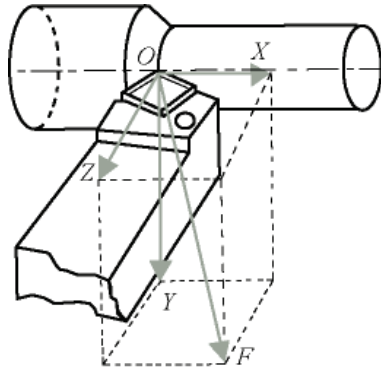


Figure 2.3 – Acting cutting forces on the tool in oblique cutting, Z-radial force, Y-cutting force, X-feed force, Kalhori (2001).

Cutting tools are not perfectly sharp and some kind of transition, cutting edge, exists. Hence the force in orthogonal cutting is variable distributed along the chip-workpiece-cutting tool contact area. However, the force that acts over the cutting edge and the flank is referred as ploughing force and will not contribute to the chip formation, Boothroyd and Winston (2006). This effect become more and more pronounced as the feed is reduced.

2.2 Tool and chip interaction

The interaction between tool and chip along their common interface is complex. It is difficult to study and model. Experiments for studying this process in detail and under similar conditions as during cutting, are currently not possible. The relative motion between two bodies in contact is opposed by the friction force in the area of contact where the friction behaviour is referred to the work by Amonton and subsequent Coulomb. The works states that the friction is proportional to the normal load, independent of the apparent area of contact and independent on the speed of sliding, Boothroyd and Winston (2006) and Trent (1991). However, the mean coefficient of friction in metal cutting has been observed to vary with rake angle and cutting speed indicating a behaviour that does not follow the classical friction models.

The real area of contact, A_r , under ordinary loading conditions is established between the asperities of the irregular contact surfaces. This area is usually much smaller than the apparent contact area, A_a , giving rise to a metallic contact. The normal pressure is extremely high in case of metal cutting, especially around the tool edge. Pressure up to several GPa has been observed. These circumstances influence the area of contact so that the real area of contact approaches the apparent contact area, $A_r / A_a \rightarrow 1$. The real area of contact becomes independent of the normal load and the ordinary laws of friction are no longer valid. Hence the frictional force will be independent of the normal load. Under these extreme conditions the frictional force becomes the force needed to shear the weaker of the two materials along the apparent area of contact, not at asperities. The interface region where this appears in metal cutting is referred to as the sticking region, Boothroyd and Winston (2006) and Kalhori (2001), and occurs adjacent to the tool edge where the normal stress is high. A well-established model of the chip-tool friction is shown in Figure 2.4. Further up the tool face where both the normal and the shear stress are lower and have a declining profile a sliding region appears. It should also be mentioned that the interface between the chip and the tool affects the heat transfer and thus the amount of heat that may flow into the tool. Good heat transfer is obtained if the real area in the contact interface is large.

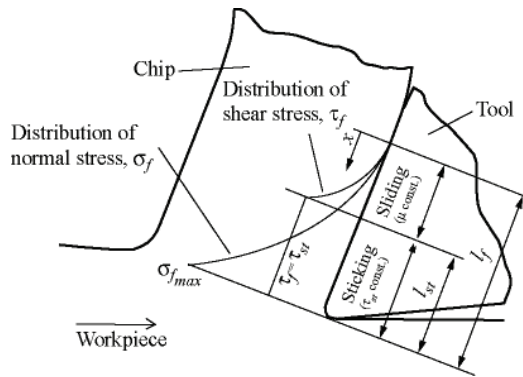


Figure 2.4 – Interaction model between chip and tool in orthogonal cutting where σ_f is the normal stress distribution, τ_f is the shear stress distribution, l_f is the chip-tool contact length, l_{st} is the length of the sticking region, Boothroyd and Winston (2006).

2.3 Heat generation in metal cutting

Most of the energy used to deform a material plastically is converted into heat. Since metal cutting causes large plastic strains, part of the plastic dissipated energy will be converted into heat and increase the temperature in the cutting zone. This will affect the behaviour of the work piece material and most probably will its strength and ductility decrease respectively increase and thereby change the metal cutting conditions. Conversion of energy into heat occurs mainly in the primary deformation and the secondary deformation zones. Shear stress from the friction will also contribute to generation of heat in the latter deformation zone. The generated heat will usually dissipate by heat conduction, convection and radiation. However the cutting velocity has a strong influence on the heat conduction in metal cutting. As the cutting speed increases, the time for heat conduction reduces. This produces adiabatic conditions, with sometimes high local temperatures.

2.4 Chip formation

The chip formed in metal cutting depends among others on the cutting process parameter, tool geometry and of the workpiece material being machined - the mechanical properties as well as the thermal properties. The cutting tool thermal conductivity has also shown to have an influence on the cutting forces, contact length, chip form and chip breaking due to temperature gradient in the contact zone, Balaji *et al.* (1999). Hence the cutting forces, temperature and strains are directly related to the chip formation and flow, Fang *et al.* (2001), and thus chip control is necessary. Although there exist many different shapes of chips and they are generally classified as continuous, continuous with built up edge (BUE), discontinuous, and shear-localized, Boothroyd and Winston (2006), Kalhori (2001), Vaz *et al.* (2007). Formation of continuous chips occurs basically when machining ductile materials under steady-state conditions at relatively high cutting speeds, Boothroyd and Winston (2006) and Kalhori (2001), for e.g. mild steel, copper and aluminium. The chip does not move straight up, instead it turns off and goes on sliding along the rake (tool) face before it curls away. Reducing the cutting speed increases the risk of continuous chip with built up edge. In this case the workpiece material welds itself to the tool face that in turn obstruct the following materials and a pile of materials is formed in front of the insert, see Figure 2.5. Hence cutting is now performed outside the cutting edge of the tool with a created cutting edge of the accumulated material and this will most likely leave detrimental footprints on the machined

surface and increase the cutting forces, Boothroyd and Winston (2006). A common action to overcome this is to increase the cutting speed so the built up edge become unstable, breaks down and is carried away by the chip.

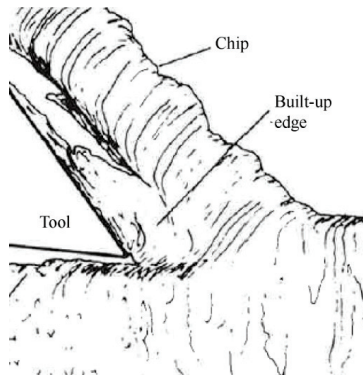


Figure 2.5 – Schematic view of BUE, Boothroyd and Winston (2006).

The work piece material in the cutting zone undergoes severe strains. These will, in combination with discontinuities, continuously break the chip into small segments when the critical fracture strain is reached. This is referred to as discontinuous chip formation. This chip form appears usually when machining brittle materials and/or machining with low cutting speeds and high feeds, Boothroyd and Winston (2006). The final shape, the shear localized chips have a well appearance serrated form on their free surface. These chips contain heavily recurrent deformed shear bands which are a consequence of thermo-plasticity instability. Shear localization starts usually at discontinuities and when the generated heat doesn't dissipate quickly enough the material softens and a localized straining occurs leading to failure. Materials with low thermal conductivity and heat capacity have an increased capability to form these kinds of chips, Boothroyd and Winston (2006) and Shaw (1997). Likewise machining at very high cutting speed may also cause this chip formation.

Chip formation is fundamental in metal cutting and comprises severe plastic deformations under high strain rates and heat generation. Therefore, the modelling of the plastic behaviour, discussed in the next chapter, is important. Sometimes it is desirable to examine the workpiece material in the vicinity of the cutting edge in order to study the chip morphology. One useful technique is the quick-stop technique where the cutting process is "frozen" by instantaneous removal of the cutting tool. This technique is usually based on shear-pin design which breaks and removes the tool under an impact load, Chern (2005). Quick-stop test based on the shear-pin design has been used within this work.

Chapter 3

Stainless steels

Stainless steels are steels with a chemical composition forming a protecting layer on the surface. The main alloying elements in stainless steels are chromium and nickel. Nickel is an austenitic stabilizer while chromium is a ferrite stabilizer. The chromium content in stainless steels should be at least 10.5 % and the maximum contents of carbon should be 1.2 %, Swedish standards institute (2000). By high contents of chromium, >11 %, a thin passive chromium oxide layer is form on the surface under oxidizing condition improving the corrosion resistance. The layer is self-healed when damaged. Nickel and molybdenum are other alloying elements contributing to enhanced corrosion resistance. The latter has the properties of decreasing the required oxidizing environment to form a passive protected layer and increasing the resistance to chloride induced pitting, Hedström (2005). Carbon is an alloying element that strongly contribute to the strength and which has the devastating property of forming chromium carbides. Depending on type of steel, the carbon contents may vary from really low value to high.

However, stainless steels may be subdivided into ferritic, martensitic, austenitic, austenitic-ferritic (duplex) and precipitation hardening steels after their microstructure Hedström (2005) and Swedish standards institute (2005). It is well known that the alloying elements and the quantity influence the microstructure. A convenient way of estimate the effects of various alloying element and their quantity on the microstructure is by a Schaeffler-diagram where the ferritic and austenitic forming effects are calculated by chromium respectively a nickel equivalent. The diagram was originally designated for prediction of the microstructure after welding, Ring Groth (1998). Several equations exist in the literature but following Honeycombe and Bhadeshia (1995) the equivalents are calculated by

$$Cr_{equivalent} = Cr + 2Si + 1.5Mo + 5V + 5.5Al + 1.75Nb + 1.5Ti + 0.75W \quad (3.1)$$

$$Ni_{equivalent} = Ni + Co + 0.5Mn + 0.3Cu + 25N + 30C$$

where the individual concentrations are in weight percentage. As can be seen nitrogen and carbon are the greatest austenite stabilizing alloying elements and have a great influence on the nickel equivalent. Carbon and nitrogen have also a strong effect on the strength by interstitially solution, Hedström (2005), Marshall (1994). Nitrogen has also the characteristics of forming Cr_2N and thereby reduces the depletion of chromium in the grain boundaries by reducing the precipitation of $Cr_{23}C_6$. The intergranular corrosion (IGC) is somewhat reduced. Nickel on the other hand increases the susceptibility to intergranular corrosion, Marshall (1984). A chromium-depleted zone increases the susceptible of stress corrosion cracking (SCC) and austenitic steels are known to be susceptible to SCC by intergranular stress

corrosion cracking (IGSCC) and transgranular cracking (TGSCC), Marshall (1984). Figure 3.1 shows the effect of various alloying elements.

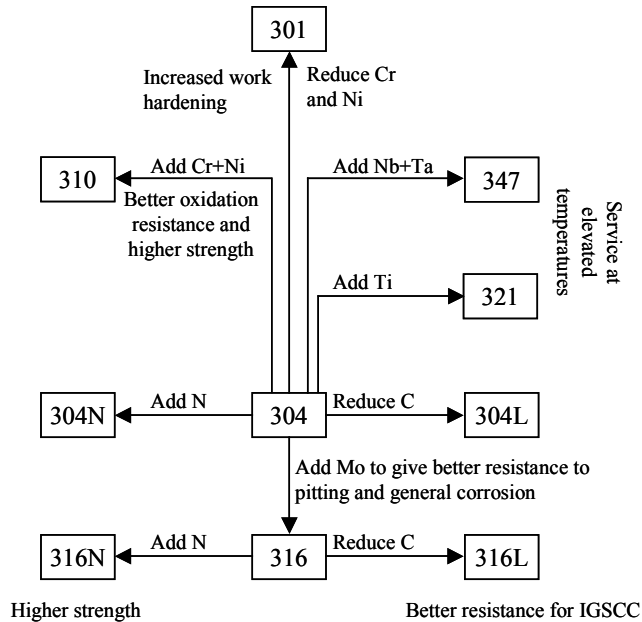


Figure 3.1 – Flow diagram of steels and alloying elements impact.

3.1 Ferritic stainless steels

Ferritic stainless steels have a ferritic microstructure made up by a BCC-structure, are magnetic and have a rather high brittle-fracture transition temperature which strongly depends on the level of carbon and nitrogen. These alloys are somewhat less ductile than the austenitic steels and are not hardenable by heat treatments.

3.2 Martensitic stainless steels

Martensite is magnetic and has a high strength and may be formed during cooling or cold working. Martensitic steels have traditionally high carbon contents ranging from 0.08 to 1 % and may be hardened and tempered. In case of high contents of ferrite in the microstructure the steels are called martensitic-ferritic. The weldability decreases with increasing carbon contents. However, steels with a martensitic and austenitic microstructure exist where the carbon content is maximum 0.06 %, Swedish standards institute (2005). Steels with this two-phase microstructure are usually called martensitic-austenitic stainless steels. Martensitic steels with really low carbon content, maximum 0.030 %, have been developed for high strength and good impact strength and weldability.

3.3 Austenitic-ferritic stainless steels

Austenitic-ferritic steels have a two-phase microstructure and are commonly called duplex. The apportionments of the individual phases are generally 30-50 % ferrite and the rest is austenite, Swedish standards institute (2005). All modern duplex steels have low carbon contents and the contents of nickel are low.

3.4 Precipitation hardening stainless steels

The characteristic of these steels are the precipitation of intermetallic compounds, carbides, nitrides or copper phases, Swedish standards institute (2005). These steels may be hardened by heat treatments.

3.5 Austenitic stainless steels

Austenitic steels have an fcc-structure and have generally an excellent combination of corrosion resistance, ductility, toughness and weldability, Totten (2007). However, the austenitic structure has the ability to transform into martensite during cooling and/or plastic deformation. The stability of the austenitic structure depends on the chemical composition. Carbon and nitrogen are alloying elements that strongly promote an austenitic structure. Austenitic stainless steels that may transform into martensite during cooling and/or plastic deformation are called metastable austenitic steels.

Chapter 4

Plastic behaviour of solid polycrystals

The word "plastic" comes originally from the classical Greek meaning "to shape", Lubliner (2008). This meaning corresponds well with the remaining deformation that can be observed after plastic straining and unloading of metals and alloys. However, it is well known that the shear stress needed to cause plastic deformation of metallic materials is significant lower compare to the theoretical shear stress of a perfect crystal, Hull and Bacon (2001) and Jastrzebski (1987), and that the behaviour are to be explained by irregularity in the crystal structure disturbing the regular atom structure. The words defects or imperfections are commonly used in order to describe these irregularities. The word defect will henceforth be used. Hence, defects play an important role since they are closely related to the behaviour of the material, not always in an adversely way.

During plastic deformation an evolution of the microstructure will take place which affects the overall behaviour of the material. Hence there is a link between the so frequent mentioned stress-strain curves on the global scale and the microstructure and its evolution. Good understanding of the structure-sensitive mechanism, their interaction and evolution is indispensable for physical based material modelling. This chapter aims to give a brief introduction into plastic behaviour, strain hardening and softening mechanisms. Firstly, different kinds of defects in the crystal lattice are discussed as they play important roles in plastic deformations. Thereafter some processes or mechanisms are shortly described. Finally, the effects of these processes together with the defects and other microstructural features on the flow stress are discussed.

4.1 Defects in solid polycrystals

The atoms in a perfect crystal are arranged in a regular and repeated three-dimensional array. Several different possible arrangements of the individual atoms exist and hence, different crystal structures exist. Hexagonal close packed (hcp), body-centred cubic (bcc) and face-centred cubic (fcc) are the most common crystal structures in metals, see Figure 4.1. The regular crystal structure is usually, however, delimited in their extensions.

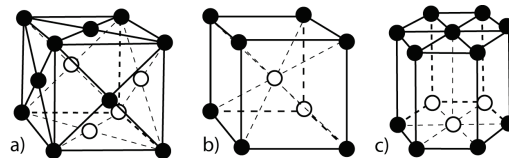


Figure 4.1 – Schematic illustration of a) fcc-structure b) bcc-structure and c) hcp-structure.

Metals and alloys are mainly an aggregate of many crystals. The original microstructure of the material is principally determined from the solidification process where different grains are formed from the crystallization characterized by solid nucleation and grows, Stouffer and Dame (1996). Nucleation starts at many different positions at the same time. The embryos that reach a critical size will continue to grow along favourable direction into crystalline aggregate where the structure of the grains can differ considerably or be more congruent. This process enables defects to be formed. In case of great diversity between adjacent grains a high-angle grain boundary is formed characterized with great misfit in crystal orientation. These grain boundaries or planar defects constitute favourable sites for diffusion, phase transformation, precipitation reactions and obstacles for dislocations and contribute to the properties of the material, Stouffer and Dame (1996) and Meyers *et al.* (2002). They may also act as sources or sinks for dislocations, Janecek and Tangri (1995). Hence this will facilitate and contribute to the different phenomenon that occur during plastic deformation and will inevitably affect the mechanical response of the material. However grain boundaries are not the only defects that may exist. Defects may also be formed during inelastic deformation. This section will focus on different kinds of defects. They are usually divided after their geometrical extension into point, line, planar defects, Jastrzebski (1987) and Babu (2008), and volume defects, Hull and Bacon (2001). Voids are examples of the latter defect.

4.1.1 Point defects

Point defects are generally associated with a small localized disturbance in the crystal structure as well as the arising stress field and can be divided into vacancies, interstitials and impurities, Hull and Bacon (2001), Jastrzebski (1987) and Dieter (1988). Vacancy is an atom site where the atom is missing and an interstitial is when an atom is occupying the space in between the atoms in the regular crystal structure. Vacancies and interstitials can be formed by self-interstitials when atoms from the crystal structure moves to interstitial sites. The concentrations of both vacancy and interstitials are affected by the temperature, increase with increasing temperature. However the formation of vacancy is generally favoured due to lower energy for formation, Hull and Bacon (2001) and Jastrzebski (1987). Worth mentioning is that clustering of vacancies creates voids.

Impurities defects are formed by substitutional or interstitial of solute atoms. The former originates when the original atom is replaced with a foreign atom in the crystal structure. The differences in size are closely related to the distortion in the crystal structure as well as the activation energy. In case of small or insignificant difference the distortion and activation energy is small. The temperature has also in this case a strong influence. Hence, increasing the temperature increases the probability of forming point defects. Irradiation, plastic deformation and quenching are other ways introducing point defects.

4.1.2 Line defects

Line defects are defects that geometrical can be characterized by a line. The so important dislocation belongs to this category. Two types of dislocations occur frequently in the literature, edge and screw dislocations, see Figures 4.2 and 4.3. Edge dislocations are disruptions in the crystal structure constituted by an extra half plane of atoms squeezed in between the regular atom sequence forming a dislocation line. When the extra plane of atoms is above the slip plane it is by convention called a positive edge dislocation. A negative edge dislocation has the extra plane of atoms below the slip plane. This extra half plane of atoms cause a distortion and affect the local stress field in a way that compression and tension stresses are created above respectively below the slip plane for a positive edge dislocation. A screw dislocation can be visualized by moving half of the upper part of the crystal to right

relative the lower part so that a hack is created on each side, see Figures 4.2 and 4.3. However dislocations do not need to form straight lines or even lie in a single plane. Both types of dislocation may occur simultaneously in a lattice and they may also appear together forming a mixed dislocation. A difference to be noted between the two types of dislocations is the distinction between the direction of propagation and the direction of the applied force.

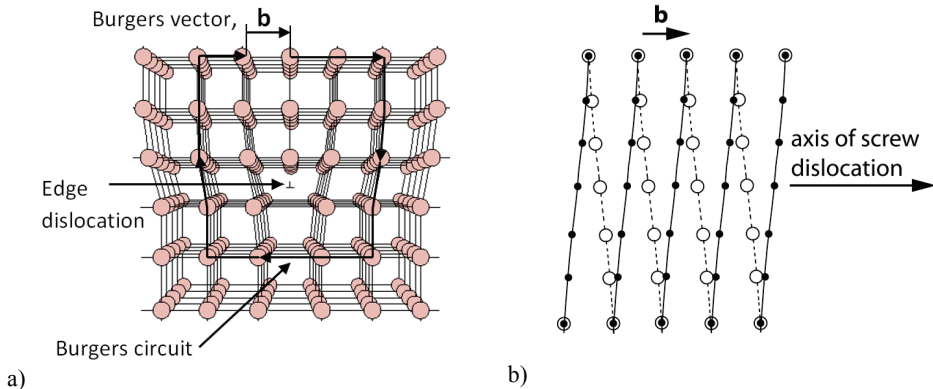


Figure 4.2 – a) edge dislocation and b) screw dislocation where the open circles and the filled circles are above and below the plane of action respectively.

There are a large number of dislocations that have become immobile during the plastic deformation. These dislocations contribute to the hardening of the material as discussed later. The density of the moving dislocations is smaller. As mentioned earlier dislocation causes a misfit in the lattice. This is a stored energy in the lattice and thus a stored energy is associated with the dislocation. In order to reduce the total stored energy due their existence dislocations may form different patterns e.g. LEDS, low energy dislocation structure. These patterns are further discussed in section 5.2.

4.1.3 Planar defects

Metals are in their usual form composed of a large number of randomly oriented grains forming a polycrystalline aggregate where each grain has an atom arrangement of a single crystal. The different crystal orientations form a grain boundary that separates the various individual grains. The created crystal structure has its source from the dispersed nucleation and following growth and therefore the extent of miss-fit between the grains may vary. Generally, the miss-fits are defined as Low Angle Grain Boundaries (LAGB) and High Angle Grain Boundary (HAGB) where the tilt and twist boundaries belong to the former group, Jastrzebski (1987) and Babu (2008). Other planar defects are twinning and stacking faults, Hull and Bacon (2001) and Lubliner (2008). The former is a mechanism where a portion of the crystal structure will form a mirror image of the unchanged crystal structure under applied shear stress. The atom movements are small but a noticeable change in the regular crystal structure appears. Stacking faults are an error in the regular stacking sequence of atom planes. The atoms are not in the expected position they would have with respect to a perfect crystal. The width of the stacking fault is closely related to the energy the stacking fault possesses, Stouffer and Dame (1996).

4.2 Deformation mechanism

Plastic deformation of crystalline metals may occur by different mechanisms, dislocation slip, twinning and phase transformation, Meyers (1994) and Vuoristo (2004). Diffusional creep is

another mechanism, Meyers *et al.* (2002), where atoms are diffusing causing plastic deformations. Plastic deformation is usually not restricted to a single isolated mechanism. Several simultaneously acting mechanisms are more likely. All these deformation mechanisms are however competing mechanisms that are activated under specific deformation conditions. Furthermore, their activation criterion is affected differently by temperature and strain rate. For example, large stacking fault makes cross slips difficult and gliding dislocations are therefore restricted in motion which may build up large stress and activate twinning. At lower temperature and higher strain rates, then slip requires a larger stress. Then it may turn out that twinning or even martensite formation may occur easier than slip. According to Hull and Bacon (2001) and Stouffer and Dame (1996) slip is the far most common manifestation of plastic deformation in crystalline solids. Different mechanisms are discussed below for completeness although all are not used in the current work.

4.2.1 Deformation by slip and climb of dislocations

Two basic types of dislocation motion exist, glide and climb, Hull and Bacon (2001). Slip is a manifestation of many dislocation glides that occurs most readily between close-packed atomic planes in specific directions. Burgers vector is a frequently used quantity defining the magnitude and direction of slip. A convenient way of defining it is by Burgers circuit, Dieter (1988). Such a circuit is illustrated in Figure 4.2. Burgers vector is the vector required to complete the atom-by-atom circuit around the dislocation, Jastrzebski (1987).

Consider the edge dislocation in Figure 4.2. Only small relative changes in position are required for the edge dislocation to shift position, dislodge from the current bonds and form bonds with the nearest atoms in the continuous plane beside it self. Hence the required applied stress is lower than the required stress needed to simultaneously move all atoms from one position to another in a perfect crystal structure, Stouffer and Dame (1996). The movement of the edge dislocation throughout the crystal lattice occurs subsequently by small interatomic distance with Burgers vector perpendicular to the dislocation line, see Figure 4.3. The lattice on each side of the slip plane is displaced relative to each other. The applied stress to overcome the lattice resistance is known as the Peierls-Nabarro stress, Hull and Bacon (2001) and Dieter (1988).

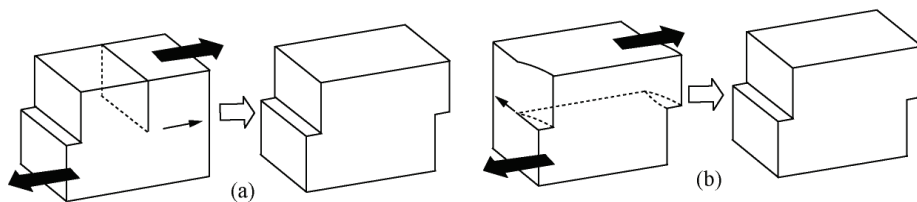


Figure 4.3 – Dislocation movements and final state of deformation for a) edge dislocation and b) screw dislocation.

Screw dislocation is the second basic type of dislocations. It does not contain any extra plane of atoms as the edge dislocation, Hull and Bacon (2001). Upon shearing the relative motion of the upper and the lower part of the crystal moves the dislocation line forward, see Figure 4.3. Hence, the movement of a screw dislocation will produce a displacement parallel to the dislocation line. Unlike the edge dislocation, Burgers vector is parallel to the dislocation line and do not define a unique plane. Therefore the motion of a screw dislocation is less restricted than the motion of an edge dislocation. Hence, screw dislocation can easily cross slip onto

another slip plane, Dieter (1988) and Hull and Bacon (2001). An edge dislocation can after all move out of its slip plane by climb i.e. via a temperature dependent diffusion process, Dieter (1988) and Hull and Bacon (2001). However, irrespective of type of dislocation the slip direction is parallel to Burgers vector, Dieter (1988). Dislocation climb is a diffusion process where vacancies or interstitials diffuse to or away from the dislocation, Dieter (1988), Hull and Bacon (2001) and Stouffer and Dame (1996). It involves mass transportations and requires thermal activation. Hence the importance of climb increases with the temperature. An edge dislocation can therefore move out of its slip plane by thermal activation. Consider a positive edge dislocation as in Figure 4.2. A positive climb is said to occur when atoms are removed from the extra half plane so that the dislocation line moves up and out of its original slip plane. A negative climb occurs if the opposite occur. However, it is highly unlikely that all atoms along the dislocation line are removed or that a complete row of atoms are added, Dieter (1988). Instead, it is more likely that climb occurs over a short segment of the dislocation line as in Figure 4.4. The resulting vertical steps are called jogs. Steps that lay in the slip plane are called kinks, Hull and Bacon (2001). Kinks or jogs do not impede the motion of an edge dislocation.

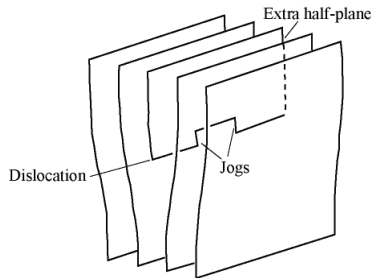


Figure 4.4 – Schematic view of a single jog on an edge dislocation, Hull and Bacon (2001).

The actual slip plane and slip direction during plastic deformation correspond to the slip system where the resolved shear stress reach the critical shear stress. These slip system are differently oriented from grain to grain. Hence the deformation is not homogenous on the microscopic scale. In fact, the deformation will even vary inside grains leading to the development of microstructural inhomogeneity, Humphreys and Hatherly (2004), characterized by different features. These different heterogeneous features are shown in Figure 4.5. Shear bands, Figure 4.5a, are a result of plastic instability manifested by narrow regions of intense shear. They occur independently of the grain structure and can extend through the grains and across their boundaries. The temperature and the size as well as the orientation of the grains have shown to influence the shear band formation. Larger grain size facilitates the formation of shear bands while increased temperatures are shown to have the opposite effect, Humphreys and Hatherly (2004). Deformation bands, Figure 4.5b, are the next feature in the hierarchy. They represent the coarsest form of grain subdivision. When the orientation change from one region to another is sharp, a deformation-induced grain boundary is formed, Humphreys and Hatherly (2004). Deformation bands are developed as a consequence of the deformation of polycrystals and are dependent of the grain orientation, grain size and the temperature. Deformation banding decreases with increasing temperature and is more easily formed in coarse grains, Humphreys and Hatherly (2004). Formation of cell structure, Figure 4.5c, is the next feature in the hierarchy followed by dislocations, Figure 4.5d. The formation of cell structure is sometimes named dislocation substructure or low energy dislocation structures (LEDS). The latter name is due to the fact that this pattern

formation reduces the stored energy compared to having uniformly distributed dislocations. Dislocation and cell formation are discussed in section 5.2.

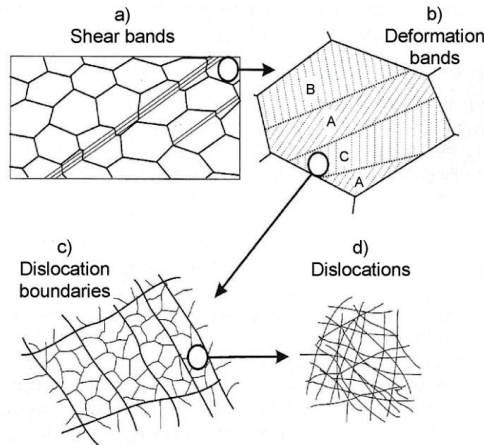


Figure 4.5 – Schematic illustration of the hierarchy of the microstructure deformed by slip a) shear bands b) deformation bands c) dislocation boundaries d) dislocations, Humphreys and Hatherly (2004).

4.2.2 Deformation by twinning

Deformation twinning is a deformation mechanism where a portion of the original crystal will take up a new orientation under shearing. The twin portion will in the simplest cases produce a mirror image of the parent crystal, Hull and Bacon (2001), see Figure 4.6. The applied shear stress is the driving force, Dieter (1988). The movements of the individual atoms are small and the resulting plastic deformation accommodated by twinning is comparably small compared to slip. The contribution to the macroscopic strain depends on the volume fraction of the twins.

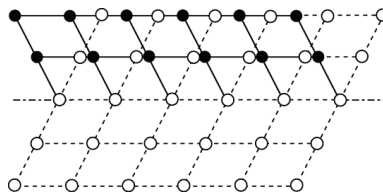


Figure 4.6 – Picture of a twinned structure where atoms have taken up a mirror image of the original structure.

According to Dieter (1988) the maximum extension a twinned zinc crystal can accommodate is only 7.39 %. The resulting orientation changes may however place new slip system in favourable orientation so that additional slip can take place. The time frame for twin formation is short, can be formed within a few microseconds. A click can sometimes be heard. Slip requires usually more time before a slip band is formed, Dieter (1988). However, deformation by twin formation is more pronounced when the slip systems are restricted to accommodate the imposed strain. Furthermore, metals with low stacking fault energy are

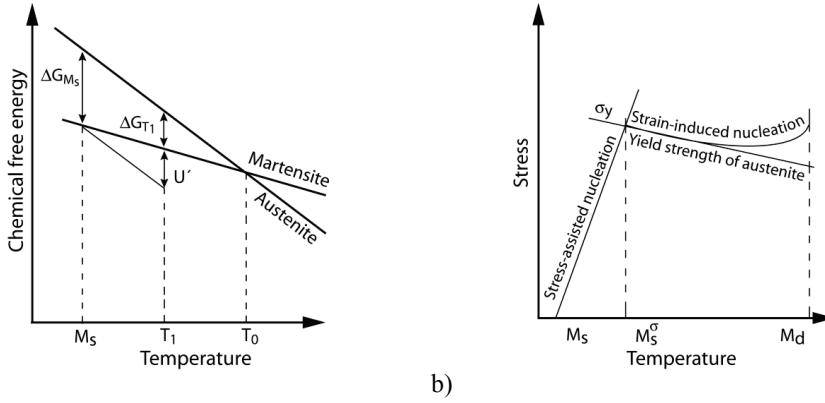
known to have restricted ability to cross slip and that restricts the plastic deformation that can be accommodated by slip alone. Hence twinning becomes easier when this energy is lower. The stacking fault energy strongly depends on the chemical composition and the temperature, Talonen and Hänninen (2007). According to Sencer *et al.* (2005), a material with low stacking fault energy is more prone to form partial dislocations giving rise to planar arrays of dislocations and related planar microstructures as twins. Twinning is thus a nucleation and growth process where the nucleation is the most critical part according to Meyers *et al.* (2001). Growth can occur at stresses far below the nucleating stress. When the critical stress is reached twins nucleate and continue to grow until the saturated thickness of the twin is reached which is related to the critical twin nucleus size, Xiao *et al.* (2008). A compilation of different results in Meyers *et al.* (2001) showed that the critical twinning stress increases with the stacking fault energy. Furthermore the twinning density was shown to further increase when subjected to stresses beyond the critical stress for nucleation. However, twins may not only be formed during plastic deformation. It may also be formed during solid state phase transformation or annealing. An annealing twin structures may be formed e.g. during recovery, primary recrystallization or during grain growth Humphreys and Hatherly (2004).

4.2.3 Deformation via martensite transformation

Martensitic transformations can be regarded as a diffusionless shear transformation characterized by co-operative movement of a relatively large number of atoms resulting in a change in the crystal structure. Unlike diffusion controlled transformations the martensitic transformation occurs instantaneously with a speed that nearly can reach the speed of sounds, Haasen (1996). The movements are usually small, less than the interatomic distances and are thus similar to twinning, Due to the ordered and the co-operative movements the transformation is sometimes said to be of a military nature, Haasen (1996), Porter and Easterling (2004). The transformation is commonly driven by a change in the temperature or by mechanical deformation. The change in the free energies of austenite and α' -martensite as function of temperature are shown in Figure 4.7a. The onset of spontaneous martensitic transformation takes place when the difference between the chemical free energies reaches the critical free energy difference ΔG_{Ms} that corresponds to the M_s -temperature. The M_s -temperature can be estimated by following equation, Marshall (1984)

$$M_s = 1305 - 61.1\%Ni - 41.7\%Cr - 33.3\%Mn - 27.8\%Si - 1667\%(C + N) \quad (^{\circ}C) \quad (4.1)$$

Quenching to cryogenic temperatures is sometimes necessary in order to reach the critical value of ΔG_{Ms} . Highly alloyed grades of austenitic stainless steels are considered to be stable and belong to this category, Hedström (2005). However, the martensitic transformation can be promoted by applied stress. This implies that the critical value of ΔG_{Ms} can be reached for temperatures above the M_s -temperature, Maalekian and Kozeschnik (2010), see Figure 4.7a. The driving force for the onset of martensitic transformation at $T > M_s$ -temperature consists of a chemical and a mechanical component, U' .



a) Figure 4.7 – a) Schematic illustration of chemical free energies of austenite and martensite as function of temperature, Maalekian and Kozeschnik (2010) and b) schematic illustration of stress-assisted and strain-induced martensitic transformation, Olson and Cohen (1972).

Olson and Cohen (1972) established a concept of stress-assisted and strain-induced martensitic transformation. Earlier had Bolling and Richman (1970) defined a temperature, M_s^σ , below which yielding can occur by means of martensitic transformation. This region between the M_s and M_s^σ temperatures, is referred as the stress-assisted transformation region, see Figure 4.7b. The required assisted stress is in the elastic range and increases with the temperature. It is generally believed that the stress-assisted martensitic transformation starts at the same sites responsible for spontaneous martensitic nucleation, Hedström (2005). Martensitic transformation above M_s^σ is referred to strain-induced martensite and involves production of new nucleation sites. The martensitic transformation ceases when the temperature has increased so much that the difference in the chemical free energies becomes too small for nucleation of martensite by means of plastic deformation. This temperature is referred as the M_d -temperature, Maalekian and Kozeschnik (2010). Estimation of the temperature for which 50 % α' -martensite are formed after a true strain of 30 % can be done by the following relationship, Hedström (2005) and Marshall (1984)

$$M_d = 413 - 9.5\%Ni - 13.7\%Cr - 8.1\%Mn - 9.2\%Si - 18.5\%Mo - 462\%(C + N) \quad (^\circ C) \quad (4.2)$$

It has been found that austenitic microstructure may transform to strain-induced ϵ -martensite and α' -martensite during plastic deformation, Talonen and Hänninen (2007), Talonen *et al.* (2005). The former has an hcp structure while the latter has a structure close to bcc. ϵ -martensite is in contrast to α' -martensite non-magnetic, Marshall (1984). The stability of the austenite and the tendency to form α' -martensite is strongly dependent on the chemical composition and the temperature, Talonen and Hänninen (2007) and Hecker *et al.* (1982). Strain rate, grain size and deformation mode are other important factors, Talonen *et al.* (2005). Co-existence of austenite, α' -martensite and ϵ -martensite has led the question regarding the sequence of formation. The sequence has according to Talonen *et al.* (2005) and Seetharaman and Krishnan (1981) been found to be $\gamma \rightarrow \epsilon \rightarrow \alpha'$ i.e. ϵ -martensite is formed directly from the austenite phase acting as an intermediate phase. Although there are works showing that formation of α' -martensite can proceed without ϵ -martensite, Murr *et al.* (1982). Talonen and Hänninen (2007) studied the interplay between the stacking fault energy SFE, shear band and α' -martensite transformation. They found that shear bands were very sensitive to chemical composition and temperature but also necessary precursor for α' -martensite as

these intersections act as the nucleation sites. The effects of the temperature and the chemical composition seem to be mostly accounted for by the variation of the SFE. Furthermore the density of ϵ -martensite was promoted by low alloying and low deformation temperatures and was observed to be higher in samples with the highest number of shear bands. Shear bands is a collective term and can be in the form of ϵ -martensite, mechanical twins or dense stacking fault bundles, Olson and Cohen (1975). Murr *et al.* (1982) studied the evolution of the strain-induced α' -martensite of AISI 304 stainless steel and found that the deformation mode influence the production of shear band intersection and the growth of α' -embryos. More shear band intersections was observed by means of biaxial tension. Thus α' -martensite grows out of the slip plane into a blocky polyhedral. They postulated that growth occurs by repeated nucleation of new embryos and coalescence and not by propagation of α' -embryos. The strain-induced transformation of two austenitic steels grades, AISI 301LN and AISI 304, was studied by Talonen *et al.* (2005). The grades showed different behaviour in α' -martensite formation. Significantly more strain-induced α' -martensite was formed in AISI 301LN which was believed to be due to its higher M_{d30} temperature. The fraction of α' -martensite increased with the true strain in accordance with a sigmoidal shape function towards a saturation value. The content of α' -martensite was also shown to influence the work-hardening behaviour especially for the AISI 301LN. The strain-induced α' -martensite was also observed to occur more rapidly in the prestrained variant of AISI 301LN. A greater amount α' -martensite has also been reported to occur in coarser grained AISI 304LN by Ganesh Sundara Raman and Padmanabhana (1994). This lead to increased ductility as the work-hardening increased and postponing the necking. Furthermore a significant increase in α' -martensite formation could be observed at an engineering strain level of around 0.6. Increased strain rate within the low strain rate range was also reported to increase the α' -martensite contents.

4.3 Intersection of dislocations

Several slip planes may be active during plastic deformation. A slip plane of one system may intersect slip planes of other slip systems. Dislocations may therefore intersect other dislocations as they move through the lattice. An intersection of one dislocation with another on an intersected slip plane can under certain condition create either jogs or kinks. The former is a step in the dislocation line out of the slip plane while the other is a step which remains in the slip plane. Consider Figure 4.8a. A moving edge dislocation CD on the slip plane P_{CD} , with Burgers vector \mathbf{b}_1 , will create a resulting jog JJ' in the edge dislocation AB after intersection. The resulting jog has an edge orientation and can readily glide with the dislocation AB. No jog is formed in the dislocation CD since the Burgers vector \mathbf{b}_2 is parallel to dislocation line CD. Hence a jog is formed when Burgers vector of the intersecting dislocation is normal to the dislocation line. The resulting formation after intersection between a moving edge dislocation AB and a screw dislocation CD is shown in Figure 4.8b. The created jogs, JJ' and QQ', have an edge orientation. However the only way the jog QQ' can move by slip is along the direction of burgers vector \mathbf{b}_2 . Hence the only way the screw dislocation CD can slip to a new position with its jog is by a non-conservative process as climb, Hull and Bacon (2001) and Dieter (1988). Since climb is a thermally activated process the motion of the screw dislocation will be impeded by the jog at low temperatures. However to move non-conservatively the jog must either create vacancies or interstitials. Jogs that produce vacancies are called vacancy jogs while jogs that produce interstitials are called interstitial jogs. This type of intersections together with intersections between two screw dislocations is the most important type of intersection regarding plastic deformation, Dieter (1988). A dislocation will encounter other dislocations during its motion through the lattice. Many intersections will occur in which vacancy jogs and interstitial jogs are produced. These

tend, according to Dieter (1988), glide along the screw dislocation and annihilate each other to a certain extent.

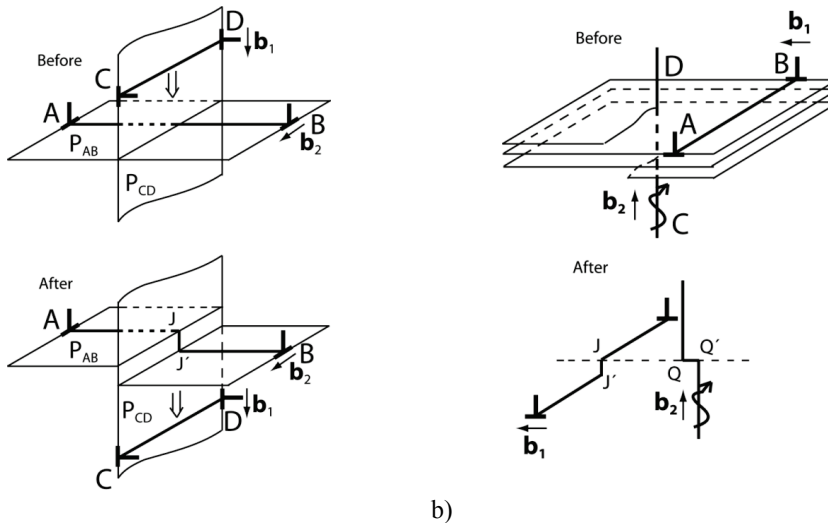


Figure 4.8 – Intersection of a) edge dislocations and b) of an edge dislocation AB with a screw dislocation CD.

4.4 Consequences of the deformation mechanisms

The different phenomena discussed in the previous sections affect the plastic deformation of polycrystals. They can either contribute to an increase in flow stress, hardening, or a decrease, softening. The competition between the hardening and the softening yields the final strengthening. Hardening and softening are discussed next.

4.4.1 Hardening

Plastic deformation may take place due to several mechanisms e.g. slip, mechanical twinning and martensite transformation. Though, dislocation and their motions have a pivotal role in plastic deformation. At temperatures lower than approximately $0.5T_m$ plastic deformation is primarily governed by slip, Stouffer and Dame (1996). Hence the required stress for the onset of plastic deformation is the stress needed to move dislocations. But as dislocations propagate through the lattice they will encounter different kind of obstacles that will either impede the motion or even obstruct the motion so they become immobilized. Higher stress is required to maintain the motion. As mentioned in the beginning mechanical twinning is a deformation mechanism but it may also contribute to hardening by impeding the dislocation motion by subdividing the grains. The same effect may also martensite transformation have. Hence, hardening is inversely related to the mobility of dislocations. In the literature one finds various types of hardening, work hardening, solid solution hardening and precipitation hardening etc. One of the most influential factors that control the movement of dislocations is the intersection with other dislocations. A crystal usually contains a network of dislocations wherein each dislocation has at least one favourable slip plane and direction. Every slip plane will therefore be threaded by dislocations. A moving dislocation will have to intersect other dislocations crossing the slip plane. The intersecting dislocations are usually called forest dislocations, Hull and Bacon (2001) and Dieter (1988). As described in section 4.3 the intersection of two dislocations may under certain conditions generate a step in the dislocation

line. The ease by which dislocations continue to move depends on the intersection process. In contrast of jogs in an edge dislocation jogs in a screw dislocation do impede the motion and may even lead to formation of vacancies and interstitials, Dieter (1988). As the plastic deformation proceeds dislocations become immobilized at obstacles or annihilated. In order to accommodate the imposed strain rate mobile dislocations are created or immobilized dislocations are remobilized. The total dislocation density increases. An important consequence of this is that the number of intersection increases. When the resistance to slip increases the required stress to maintain the plastic deformation continuously increases. The increase in the dislocation density and the intersection between dislocations are the underlying mechanisms to what is called strain hardening or work hardening. Hence, the intersection processes will influence the rate at which the crystal hardens, Hull and Bacon (2001).

In contrast to intersection of dislocations located in different slip planes, dislocations may pile up on the same slip plane at barriers such as grain boundary, twin boundary or precipitates, Stouffer and Dame (1996). The leading dislocation in the pile up is exposed not only by the applied shear stress but also by stress from the other dislocations in the pile up. The stress increases linearly with the number of accumulated dislocations, Hull and Bacon (2001). The stress on the leading dislocation can be so high that it can initiate yielding in other instances or even nucleate a crack, Dieter (1988). The back stress that occur and acts opposite to the applied stress will oppose the motion of additional dislocations in the slip direction. Furthermore, the spacing between the dislocations increases with the distance from the leading dislocation. According to Dieter (1988), break down of the barrier would either occur by slip on a new plane, dislocation climb or by a crack. When unloading and reloading in the opposite direction the back stress is in the same direction as the applied shear stress and will thus facilitates slip, Stouffer and Dame (1996). The shear stress for the onset of yielding decreases. This phenomenon is known as the Bauschinger effect.

Introduction of solute atoms into solid solvent-atom lattice contributes to hardening, solution hardening. If the solvent and solute atoms are of similar size the solute atoms will occupy lattice points in the crystal lattice. But if the solute atoms are much smaller than the solvent atoms, the solute atoms occupy the interstitial position in the lattice. The former is called substitutional solid solution while the latter is called interstitial solid solution, Stouffer and Dame (1996) and Dieter (1988). The effect of solute atom is increased resistance to dislocation motion. It arises from the disturbances in the lattice caused by the differences in size and shear modulus Sieurin *et al.* (2006) between the solute and solvent atoms. As a result the stress-strain curve will usually be lifted as a whole, Dieter (1988).

Precipitation hardening is another hardening mechanism where fine second-phase particles are distributed in the crystal. These second-phase particles also act as obstacles and impede the motion of dislocations and may even act as pile-up barriers. Their effectiveness depends on many factors as: the size, shape and density, Stouffer and Dame (1996). Dislocations must bypass the particles by Orowan looping, climb or cut through in order to move on. The required stress will in any case increase, Stouffer and Dame (1996). Other characteristic is increased resistance to the softening mechanisms recrystallization and grain growth, Dieter (1988).

4.4.2 Softening

During plastic deformation the microstructure of the material undergoes changes. Most of the work done by the external loads will dissipate as heat and only a small portion of the work will be stored in the material. The reduction of this stored energy works as driving force for restoration processes. Restoration is a concept that involves both recovery and

recrystallization. These are competing processes driven by the same stored energy. Hence the extent of recovery depends how easy recrystallization can occur, Humphreys and Hatherly (2004). Recovery is usually divided into static and dynamic recovery where the latter mechanism competes and counteracts with the hardening during plastic straining, Stouffer and Dame (1996). Recovery and recrystallization is discussed below.

Recovery involves reduction of dislocations, and thereby stored energy level, and is very much affected by the temperature. Remobilization of dislocations is also enhanced by thermal activation. Higher temperatures increase the mobility of vacancies and dislocations. Slip is however a process that likewise annihilates dislocation segments at low temperatures. Two primary processes exist, annihilation and rearrangement of dislocations, Humphreys and Hatherly (2004). Recovery is a process that consists of several events. It involves annihilation of dislocations, formation of cells (LEDS), formation of subgrains and grain growth. Climb is a process that together with glide enables annihilation of dipoles, which requires thermal activation. In the high temperature regime the climb is governed by lattice diffusion of vacancies while core diffusion is suggested to govern at intermediate temperatures Prinz *et al.* (1982). However one separates between dynamic and static recovery. Dynamic recovery is active during the deformation while static recovery operates after the deformation and when the external loads have been removed. In the former case, the external stress field due to the loads will contribute to the rearrangement of the dislocations into a lower energy structure as well as to their annihilation. Static recovery is based on internal stresses. Dynamic recovery may occur at lower temperatures than static recovery. An example of dynamic recovery is the change from dislocation tangles to cells that may occur during deformation in many materials. However, to be noted, stacking faults are important for the recovery. It affects the dislocation climb and the cross slips and hence obstructs the recovery process in metals with low stacking fault energy. Another influencing factor is solutes. Solutes may affect the stacking fault energy. But they have also a direct effect like pinning of dislocations and affecting the concentration and mobility of vacancies.

Recrystallization involves nucleation and growth of new grains, Porter and Easterling (1992), with a reduced dislocation density. The driving force is the stored energy due to the immobile dislocations interior of the grains. They form subcells that, with increasing immobile dislocation density, is defined as subgrains as their misorientations with the rest of the lattice increases. Then it may be more energy efficient for the microstructure to form new, smaller grains with a lower dislocation density in their interior. The existing immobile dislocations then go into the new grain boundaries and the reduction in stored energy is driving the process. The deformation needs to exceed a certain limit before recrystallization start. The higher dislocation density, the lower temperature is required for recrystallization Jastrzebski (1987). The sizes of the newly created grains are influenced by the existing immobile dislocation density as well as current temperature. However increased temperature increases the risk of unfavourable grain growth, which affects the ductility negatively. Otherwise, the recrystallization increases the ductility. Recrystallization occurs at temperatures above approximately $0.5 T_m$ in alloys, Jastrzebski (1987). Grain boundaries, transition bands, shear bands and twins are examples of inhomogenities that trigger recrystallization. Precipitates at the grain boundaries will on the other hand make recrystallization more difficult.

Chapter 5

Strengthening at high strain rates

Experimental tests have been conducted on a wide variety of metals and alloys in order to characterize the material responses at different strain rates and temperatures. The results have in the majority revealed a significant different behaviour between low rate deformation and high rate deformation respectively. For a given plastic strain within the low strain rate range, the flow stress increases slowly with the logarithm of strain rate. A marked increase in flow stress and strain rate sensitivity have however typically been observed at strain rates exceeding $\sim 1000 \text{ s}^{-1}$, shown later in Figures 10.3-10.5. This significant increased strain rate sensitivity has been interpreted to different mechanisms although increased dominance of dislocation drag is often cited, Guo and Nemat-Nasser (2006), Lesuer *et al.* (2001) and Regazzoni *et al.* (1987). Others argue that the observed increase in the strain rate sensitivity must be an effect of structure evolutions via for example enhanced rate of dislocation generation, twin formation and martensite formation, Follansbee and Kocks (1988) and Lee and Chiu (2006). Cell structure formation is another phenomenon that has shown to influence the strain hardening and the flow stress. Inelastic material behaviour at high deformation rates are of considerable importance when it comes to simulation of metal cutting and different effects are discussed below.

5.1 Dislocation drag

Plastic deformation, outside the range of where diffusion is dominant, occurs basically by motion of dislocation. This motion is impeded by different obstacles that has to be overcome. In the thermal activated region the obstacles may be overcome through thermal activation and the applied stress. As the strain rate increase, there is less waiting time at the obstacles for a vigorous thermal fluctuation to take place overcoming the obstacles. Hence, higher applied stress is needed in order to continue the motion of the dislocation. This results in a temperature and strain rate dependent deformation process. At very high strain rates dislocation drag processes are known to have a great influence on the motion of dislocation and the strain rate sensitivity, Kumar *et al.* (1968) and Frost and Ashby (1982). Dislocation drag has its spring from the elemental constituents of a crystal, electrons and phonons, and has a retarding effect on the moving dislocations as a Newtonian drag force according to

$$f_v = Bv \quad (5.1)$$

where f_v is the force acting on a unit length of a dislocation, B is the viscous damping coefficient and v is the dislocation velocity, Kumar *et al.* (1968) and Meyers (1994). During their motion dislocations emit and absorb phonons resulting in an additional drag process called radiation drag, B_r . Hence, the viscous damping coefficient for the total drag process may, according to Galligan *et al.* (2000), be written

$$B = B_p + B_e + B_r \quad (5.2)$$

where B_p is the phonon drag coefficient and B_e is the electron drag coefficient. The phonon drag coefficient is in contrast to the electron drag coefficient and the radiation drag coefficient temperature dependent. When the temperature decreases the phonon drag coefficient decreases. At sufficiently low temperature phonon interaction is negligible and the drag process consists only of dislocation interacting with electrons, Galligan *et al.* (2000) and Suenaga and Galligan (1971). The temperature dependent viscous drag coefficient in Frost and Ashby (1982) is written

$$B = B_e + B_p \left(\frac{T}{300} \right) \quad (5.3)$$

where T is the temperature in Kelvin.

One characteristic result from the high strain rate measurements by Ferguson *et al.* (1967), Kumar *et al.* (1968) and Kumar and Kumble (1969) was that the flow stress typically varies linearly with the strain rate over some critical level. Ferguson *et al.* (1967) examined the behaviour of aluminium single crystal in shear. They found a viscous behaviour at shear stresses higher than the thermally activated shear stress range and a proportional behaviour between shear stress and shear strain rate, approximately beyond 4000 s^{-1} , according to

$$\tau - \tau_B = \alpha \dot{\gamma} \quad (5.4)$$

where τ_B is the stress needed to overcome the long range and the short range obstacles. Kumar and Kumble (1969) investigated the dynamic behaviour of OFHC copper by means of SHPB. Their conclusion was that the strain rate behaviour could be divided into two regions, a thermally activated region for strain rates lower than 10 s^{-1} and a viscous damping region for strain rates higher than 10^2 s^{-1} . The behaviour in the latter region followed the relation above. Furthermore, the mobile dislocation density in the dynamic region was found to be independent of the strain rate and constituted only a small fraction of the forest dislocation density. Vreeland and Jassby (1971) examined the influence of viscous drag on the dislocation motion in closed packed metals and found that viscous drag has a profound effect on the dislocation motion even under obstacles controlled motions. The viscous drag reduces the kinetic energy of the dislocation which otherwise would help overcome the next obstacles. Kapoor and Nemat-Nasser (2000) performed compression tests at strain rates ranging from 10^{-4} s^{-1} to 3000 s^{-1} at various temperatures in order to investigate whether viscous drag has a profound influence on the motion of dislocations in tantalum. A linear increase in the flow stress with strain rate from 300 s^{-1} to 2300 s^{-1} , beyond which it remained constant, could be observed at 627°C . The conclusion was that viscous drag makes an important contribution to the flow stress at high temperatures. Increased density of mobile dislocation was given as the implications of the ceased increased flow stress at a strain rate of 2300 s^{-1} . The flow stress was written as

$$\sigma = \sigma_G + \sigma^* + \sigma_{drag} \quad (5.5)$$

The dislocation drag stress, σ_{drag} , was modelled as

$$\sigma_{drag} = \frac{M^2 B}{\rho_m b^2} \dot{\epsilon} \quad (5.6)$$

where M is the average Taylor factor, B is the damping coefficient, ρ_m is the mobile dislocation density and b is the magnitude of the Burgers vector. Nemat-Nasser *et al.* (2001) examined the plastic flow behaviour of the stainless steel AL-6XN, from low to high strain

rates. The strain rate and its history were reported to have a negligible effect on the microstructure evolution and the strain rate basically disappeared with increasing temperature. A physically based material model, in accordance with equation 5.5, was developed with dislocation drag included. The viscous drag shear component was written

$$\tau_{Drag} = m_0 \left[1 - e^{\frac{M^2 B}{\rho_m b^2 \tau_y} \dot{\gamma}} \right] \quad (5.7)$$

where m_0 is a material constant and τ_y is the yield stress at a temperature of 727 °C. A viscous drag resistance to the dislocation motion at high strain rates was also observed in Nitronic-50 stainless steel in the study by Guo and Nemat-Nasser (2006). Also in this case, a physically based material model with a dislocation shear drag component according to the above was used to model the material behaviour. Lesuer *et al.* (2001) used a rate equation to account for phonon and electron drag effects on moving dislocation when modelling the response of 6061-T6 and Ti-6Al-4V.

5.2 Strain rate effects on dislocation substructure

The significant increase in the flow stress and the strain rate sensitivity with increasing strain rate has been debated. Everyone does not agree that the increase strain rate sensitivity can be attributed to dislocation drag. Follansbee (1986) performed a study in order to evaluate the reason for the increased strain rate sensitivity. The conclusion were that the thermal activation controlled deformation is maintained to strain rates up to 10^4 s^{-1} and the increased strain rate sensitivity arises from the sensitivity of structure evolution rather than change in the deformation mechanisms. The history effect of Cu has been investigated by Follansbee and Kocks (1988) based on a study where the increased strain rate sensitivity shown to be an artefact of compering flow stresses at constant strain. Hence, transition from thermal activation deformation to dislocation drag control does not occur at strain rates below 10^4 s^{-1} . One conclusion was that there is a strong evidence of increased dislocation accumulation with increasing strain rates beyond $\sim 10^3 \text{ s}^{-1}$ and that this explains the increased strain rate sensitivity in Cu and other material with FCC structure. Zerilli and Armstrong (1992) concluded that dislocation drag is not responsible for the increase in the flow stress at strain rates of 10^3 - 10^4 s^{-1} . They also referred to a study where the significant increase in flow stress signifies an increased dislocation density. This is also reported by Lee and Lin (2001) for AISI 304L stainless steel. Lee and Chiu (2006) reports on a significant difference in the strain rate sensitivity and the activation volume between low and high strain rates deformation of sintered 316L stainless steel and refer to different rate controlling mechanisms. They suggest that the significant enhancement in flow stress is accounted by enhanced dislocation multiplication and accumulated and not by dislocation drag. Dislocation substructure is discussed next followed by martensite and twin formation.

Plastic deformation is primary accommodated by movements of dislocations. In a wide range of materials dislocations are found to organize themselves into an interconnected network, cell walls, that enclose comparatively dislocation free regions during plastic deformations. The driving force for cell formation has been recognized as the strain energy and its effort of finding a lower energy state, Holt (1970). It is supported by the internal stress field surrounding the dislocations and the fact that they move in response to forces acting on them. Furthermore, high mobility out of the slip plane and multiple slip may facilitate cell formation. Hence it follows that stress, temperature, elastic constant and stacking fault have

great influence, Holt (1970). Increasing the temperature will inevitably increase the possibility for dislocations to move and interact with other dislocations, even for metals with low stacking fault energy, and forming cell structures. However, cell structure has been observed to be prominent characteristics of creep, fatigue and strain hardening, Murr and Kuhlmann-Wilsdorf (1978). Results also suggests that the flow stress increases as the cell size is reduced, Lee and Lin (2001), Lee and Lam (1996) and Cheim and Duffy (1983). Other configurations of LEDS are also possible e.g. Taylor lattice or dipolar and multipolar arrays, Kuhlman-Wilsdorf (1989). It might however be argued whether dislocations are able to rearrange into an equilibrium cell configuration when the strain rate increases. Observation by Murr and Kuhlmann-Wilsdorf (1978) indicates that the time required for cell formation is in the order of $1\mu\text{s}$. Holt (1970) showed that uniformly dense distribution of dislocation is unstable with respect to periodic fluctuations in the dislocation density and therefore tends to cluster into a more energetically favoured cell structure. It was suggested that the cell diameter d is given by $d = K_c \rho^{-1/2}$ where K_c is a constant. Later on Staker and Holt (1972) found that the above relation conforms to their observation from an investigation of oxygen-free-high conductivity copper. They also found that the cell size increases while the cell wall decreases with increasing temperature. Michel *et al.* (1973) reported for AISI 316 on a gradual linear increase in the cell diameter with increasing temperature up to $\sim 0.5 T_m$ followed by a change into growing subgrains with much stronger linear increase. The dislocation density could however only be estimated for the subgrains, though it was reported to satisfy the relationship found by Holt. The two test results reported above have been conducted at low strain rates. McQueen and Hockett (1970) and Korbel and Swiatkowski (1972) performed tests in order to investigate the substructure developments in aluminium during deformation where the highest strain rate was 220 and 69 s^{-1} respectively. Both found that the cell size decreases with increasing strain rate. Results from the former also show that the cell size increases as well with increasing temperature, similar to what Staker and Holt (1972) found. Substructure developments at even higher strain rates have been studied by Cheim and Duffy (1983) and Lee and Lam (1996) in aluminium single crystal and AISI 4340 respectively. An apparent change in the strain rate sensitivity could be seen in their studies. Furthermore, the activation volume was reported to decrease with increasing strain rate. This alteration was reported as an indication of change in the dominant deformation mechanism from thermal activation to dislocation drag. Both studies show that increasing the strain rate increases the dislocation density and reduces the cell size and it was reported that both the flow stress and the strain rate sensitivity increases as the cell size reduced. Cheim and Duffy (1983) also report that the cell walls are better defined and that the cells develops into subgrains as the strain increases within the quasi-static strain rate range. Effect of strain rate on the substructure in copper was studied by Cheval and Priester (1989) by means of two strain rate level, $5 \cdot 10^{-4}$ and $2.5 \cdot 10^3\text{ s}^{-1}$. The results showed that dislocations tend to reorganize themselves into a cell structure as the strain increases. A well-defined cell structure could be seen after quasi-static compression to a strain of 10 % while just an initial stage of a cell structure was observed in case of the high strain rate loading. One reason cited is that thermally activated deformation is time-dependent which entails that dislocations will have more time to reorganize into a low energy configuration, Sil and Varma (1993). After straining to 65 % the cell structure had almost disappeared regardless of loading rate. New phenomena as recrystallization and micro-twinning were reported to occur at these high strains under high and low strain rate loading respectively. Shume *et al.* (1989) study the grain size influence on the substructure in copper at low strain rates. They found that coarser grain sizes result in larger cells but as the strain increases the difference become less pronounced. Although the strain rate influence on the cell formation was not so prominent. Though, smaller cells were reported to be expected at increased strain rates. Rao and Varma (1993), Sil and Varma (1993), and Shankaranarayan

and Varma (1995) have study the dislocation substructure at low strain rates in three different FCC metals: nickel, aluminium, copper. Unexpectedly smaller cell sizes were observed at lower strain rates in nickel. Smaller cell sizes for smaller grain sizes was also reported, contrary to what been reported for copper by Shume *et al.* (1989). An increase followed by a decrease in the cell size with increasing strain rates were reported for aluminium. The opposite tendency was found for copper. Lee and Lin (2001) report on increasing dislocation density, smaller cell sizes and increasing wall thickness with increasing strain rate in AISI 304L stainless steel. Planar dislocation arrays have at a strain rate of $4.8 \times 10^3 \text{ s}^{-1}$ and large strains been completely replaced by a cell structure. In order to study the deformation induced defects structure in aluminium, nickel and copper during really high deformation rates impact compression of thin plates was adopted by Kiritani *et al.* (2002). The strain rates in their study ranging from 10^{-2} to 10^6 s^{-1} . Characteristic finding was that during low strain rates the dislocations formed tangled groups, which further on develops into cell walls as the deformation proceeds. Somewhat better defined cell walls were observed in aluminium. In contrast, no cell walls were develops during higher strain rates regardless of strains. The dislocations distribute randomly, from the beginning to the end of the deformation. The changeover from cell structure developments to randomly distributed dislocations was observed to take place between 10^3 to 10^4 s^{-1} . An interesting observation in nickel was that the progressively increase in dislocation suddenly observed to decrease during heavy deformations. Recovery due to adiabatic heating was mentioned as underlying reason. Furthermore, the authors propose a theory for high-speed plastic deformations without involving dislocations. A high density of what is called glide elements is introduced but as the deformation progress point defects and small point defect complexes are produced. When the deformation rate decreases, as in the final stage in these tests when the projectile is retarded, dislocations are once again generated resulting in a randomly distributed dislocation structure.

5.3 Strain rate effects on martensitic transformation

As been observed, higher strain rates require higher stress for maintaining the plastic deformation and hence this may facilitate for other deformation mechanism than the usual slip e.g. twinning and martensite formation to become active. But at the same time the temperature increases due to adiabatic heating and this may have a counteracting effect. It has been found that the strain rate affects the martensite transformation in stainless steels and hence there mechanical response. However the degree of impact has been reported to strongly depend on the austenite stability, Talonen *et al.* (2005). Hecker *et al.* (1982) and Murr *et al.* (1982) found in AISI 304 stainless steel that the number of shear bands increased with strain rate at small strains causing an increased α' -martensite production. But at larger strains the α' -martensite transformation was prevented and the reason for this was said to be adiabatic heating. Also Talonen *et al.* (2005) reports on prevention of α' -martensite transformation due to adiabatic heating when the strain rate increase. Not even within the low strain range was α' -martensite formation in AISI 301LN and 304 stainless steels promoted by increased strain rate. The strain rate had a weak effect on α' -martensite formation in AISI 304, no clear differences could be observed in the α' -martensite formation at the different strain rates. In their study the strain rate increases from 3×10^{-4} to $2 \times 10^2 \text{ s}^{-1}$. The mode of deformation seems also to influence the production of shear band intersections. The amount of shear band intersections in the study by Murr *et al.* (1982) is generally higher in biaxial tension regardless of low or high deformation rate. However a significant increase in shear band intersection during high rate deformation and biaxial tension can be observed after an effective true strain of 0.25. Lee and Lin (2000) also reported on increased shear band intersections with increasing strain rate at strain rates between 800 and 4800 s^{-1} in AISI 304L stainless steel. But they also found an alternative transformation mechanism where α' -martensite is nucleated in single shear bands,

not only at intersections. Furthermore contrary to what has been reported from Hecker *et al.* (1982) and Murr *et al.* (1982) they found that the volume fraction of α' -martensite still increases with strain rates. This has also been reported by Lee and Lin (2002). α' -martensite formation has also been reported to occur during shock loading. Murr and Staudhammer (1975) observed pulse duration sensitivity in AISI 304 stainless steel. No α' -martensite was observed below 2 μ sec pulse duration at 250 kbar stress amplitude.

5.3.1 Martensitic transformation in AISI 316L

A lot of studies regarding martensitic transformation have been done on stainless steels of which AISI 304 has received considerable attention. Although some investigation have been performed on AISI 316L. However, the formation of martensite is related to the stability of the austenite, which strongly depends on the chemical composition. Chemical composition according to EN 10088-1:2005 (E) for 316L gives a M_d -temperature of -35 °C based on equation 4.2. The M_s -temperature is even lower than -273.15 °C (absolute zero) based on equation 4.1. That indicates that spontaneous transformation will not occur during cooling to absolute zero. However the chemical composition and the temperature have a strong influence on the stacking fault energy. The stacking fault may even change during deformation, increase with strain and temperature, Talonen and Hänninen (2007). This would generally reduce the M_d -temperature even more and suppress the α' -martensite formation.

Seetharaman and Krishan (1981) study the deformation characteristics of 316 stainless steel at low temperatures and found that no spontaneous martensite transformation occur on cooling down to -196 °C. Furthermore, the amount of α' -martensite formed in low strain rate tensile deformation at 25 and -70 °C was reported to be very small even at large strain levels while it increases with plastic strain at -196 °C. The transformation sequence was reported to be $\gamma \rightarrow \varepsilon \rightarrow \alpha'$ where ε -martensite initially increased and thereafter decreased with increasing strains. The study by Varma *et al.* (1994) showed that no α' -martensite is formed in AISI 316 stainless steel during tensile testing at low strain rates although the study also showed that the deformation mode is important. α' -martensite was observed after a rolling operation, increased with increasing strains. The grain size was also reported to influence during deformation by rolling. In order to investigate if any α' -martensite has been formed during high rate deformation an experimental measurement of the magnetic phase via magnetic balance was performed in this study. An insignificant increase could be observed with increasing strain and strain rate. The amount of magnetic phase increased from 0.25 %, in an undeformed specimen, to 1.20 % in a specimen deformed at an average strain rate of 8143 s⁻¹. This is even lower than been reported in Lindgren *et al.* (2008) for specimen deformed at strain rates lower than 1 s⁻¹.

5.4 Strain rate effects on twinning

Mechanical twinning can constitute a significant mode of deformation and may have a profound effect on the mechanical properties. Hence slip and twinning are competing deformation mechanisms. Twinning has according to Meyers *et al.* (2001) much lower sensitivity to temperature and strain rate than dislocation slip. However mechanical twinning may subdivide grains and thereby increase the barriers to slip by promoting accumulation and storage of dislocations. But mechanical twinning may also contribute to plastic deformation with a decrease in the work hardening rate as a consequence. Hence mechanical twinning has two opposing influence on the work hardening rate, Meyers *et al.* (2001). In order to evoke deformation twins the resolved stress needs to reach the critical stress for twinning. This means that stress concentrations at e.g. dislocation pile-ups, second phase particles and boundaries can initiate twin formation. Furthermore, the twinning stress in compression and

tension are different in presence of texture, Meyers *et al.* (2002). Byun (2003) proposed the following expression for the critical twinning stress

$$\sigma_T = \frac{2\gamma_{SFE}}{b} \frac{1}{SF} \quad (5.8)$$

where γ_{SFE} is the stacking fault energy, b is the Burgers vector and SF is the Schmidt factor. A compilation of measurements for a number of metals in Meyers *et al.* (2001) showed that the critical deformation twin stress is temperature insensitive. This issue has however been debated in the literature according to Meyers *et al.* (2001). There are results showing positive as well as negative temperature sensitivity. However, based on the Johnston-Gilman equation Meyers *et al.* (2001) derive an expression for the critical twinning stress as

$$\sigma_T = K\dot{\epsilon}^{1/m+1} e^{\frac{Q}{(m+1)RT}} \quad (5.9)$$

where m is a constant, K is a parameter, Q is the activation energy, T is the temperature and R is the gas constant. By this they showed that the critical twinning stress is strongly strain rate dependent, increases with the strain rate. According to equation 5.8 the critical twinning stress is proportional to the stacking fault energy. But stacking fault energy has been reported to be sensitive to chemical composition, temperature and plastic strain, Talonen and Hänninen (2007). It follows that increased temperature or strain increases the stacking fault energy. Hence, the critical twinning stress will increase with increasing deformation and temperature according to equation 5.8. Wu *et al.* (2006) and Rémy and Pineau (1978) reported that the critical twinning stress increases with the temperature. Experimental results from the study by Xiao *et al.* (2008) indicated that plastic deformation due to twinning is facilitated by increased straining or strain rate while increased deformation temperature shown the opposite effect. Results presented in Meyers *et al.* (2001) showed that the critical twinning stress increased with strain rate for monocrystalline iron. The critical twinning shear stress increased from approximately 170 MPa to 220 MPa at a strain rate of 10^{-3} s^{-1} and 10^3 s^{-1} respectively. Another influencing parameter is the grain size. Increasing the grain size lowers the critical stress for twinning, El-Danaf *et al.* (1999). Shock loading of metals and alloys are known to produce deformation twins. The propensity for deformation twin increases with grain size but it has also been shown that the amount of twins increases with strain and pressure, Sanchez *et al.* (1997).

Dislocation glide and deformation twinning are both straining and competing processes. Which deformation mechanism that is going to be the predominant deformation mechanism depends on which requires the least stress to be activated. Twinning has according to Meyers *et al.* (2001) much lower sensitivity to temperature and strain rate and this may activate twinning because the stress for slip increase more rapidly with increasing strain rate or decreasing temperature. According to Byun (2003) it is more probable that the flow stress at elevated temperatures is below the stress for twinning and dislocation glide becomes therefore more dominant. Investigation of the strain hardening rate in Asgari *et al.* (1997), where the compression tests were conducted in room temperature, showed that low stacking fault fcc metals exhibited a four stage response. The steadily decreasing strain hardening rate in stage A, dominated by crystallographic slip, changed into a plateau with nearly constant strain hardening rate, stage B. This change was attributed to the onset of primary deformation twins. Thereafter followed stage C with a decreasing strain hardening rate attributed to a decreased rate of primary twin formation. This followed by stage D with a nearly constant strain hardening rate associated to secondary twin formation that intersects the primary twins. It was believed that the formed twins in stage B subdivided the grains and acted as barriers for the

non-coplanar slip systems and thereby stopped up the decreasing strain hardening rate. This effect has however been reported to diminish with the temperature, Wu *et al.* (2006) and Mohammed *et al.* (2007).

5.4.1 Twin formation in AISI 316L

Metals with fcc-structure and low stacking fault energy have been reported to exhibit a four stage strain hardening response when deformed in room temperature at low strain rate, Asgari *et al.* (1997). Similar behaviour has also been reported for AISI 316L and AISI 316, Mohammed *et al.* (2007), Wu *et al.* (2006), El-Danaf *et al.* (1999) and Feaugas (1999). Feaugas (1999) reports that the portion of planar dislocation structure, like pile ups and stacking faults, increases with plastic strain and then decreases in stage B where the strain rate hardening is nearly constant. Cross slip and multiple slip become more prominent promoting formation of heterogeneous dislocation cell structure. However, Mohammed *et al.* (2007), Wu *et al.* (2006), and El-Danaf *et al.* (1999) reported that the onset of stage B coincides with initiation of deformation twins. The forgoing plastic strain signifies, according to El-Danaf *et al.* (1999), that a certain amount of dislocation density is required for twinning and thus has a direct influence on the twinning. Mohammed *et al.* (2007) reported that the critical dislocation density for twinning decreases with increasing temperature. Results have however shown that the sharp four stage strain hardening response diminishing with the temperature and is not prominent at high elevated temperatures. The reason for this is according to Wu *et al.* (2006) the strong temperature dependence of the critical stress for twinning which increases faster than the true stress. Mohammed *et al.* (2007) reported that stage B hardly existed at 400 °C while Wu *et al.* (2006) reported that activation of twinning will not take place over 200 °C. Furthermore the conclusion by Wu *et al.* (2006) was that the strain hardening is mainly controlled by dislocation-induced hardening mechanism. Sencer *et al.* (2005) investigated the influence of shock-pulse shape on the microstructure of AISI 316L. The density of twinning after 5 % quasi-statically straining was very low. The microstructure was mainly dominated by dislocations and planar slip. However twinning becomes more pronounced in the shocked samples.

Chapter 6

Constitutive material models

Constitutive material models describing the relation between the stress and strain are needed in order to analyse engineering materials and their behaviour. They are crucial for obtaining accurate results in simulation of manufacturing processes. Errors cannot be corrected by the numerical procedures. It should however be emphasised that constitutive material models are mathematical descriptions of physical phenomena and hence it follows that different models and modelling approaches exist. Traditionally, constitutive material models are formulated on a macroscopic level with variables such as strain, strain rate and temperature. These models are solely based on observed characteristics from stress-strain tests without any underlying physical interpretations and theoretical basis. Models that incorporate the underlying physics e.g. the generation and annihilation of dislocations is usually called physically based models in the current work. These physical based models are expected to have higher domain of validity since they can be extrapolated outside the range of data used for calibration of the models provided that the mechanisms included in the models are still dominating the behaviour. The interest in microstructure models with internal state variables describing features like precipitate, solutes, grain sizes, and phase fractions are increasingly used to simulate manufacturing processes. The physical based flow stress models have in some respects an advantage compared with common engineering type of models as they do have a natural connection to variables as grain size etc. as can be seen below.

6.1 Engineering models

There exist several engineering models of which some are described here.

According to Bowen and Partridge (1974), Hollomon (1945) proposed the following relation, also referred as Ludwik relation, Soussan *et al.* (1991) and Hua-bing *et al.* (2007), or the Ludwik-Hollomon relation, Bergström and Hallén (1982), between true stress and true plastic strain

$$\sigma = K \varepsilon^p{}^n \quad (6.1)$$

where ε^p is the plastic strain, K and n are material constants. Ludwigson observed however that the relation could not describe the behaviour of austenitic stainless steels at low strains well and therefore proposed a correction term Δ to account for the deviations at low strains, Soussan *et al.* (1991). The modified equation is written

$$\sigma = K_1 \varepsilon^p{}^{n_1} + \Delta \quad \text{where } \Delta = e^{(K_2 + n_2 \varepsilon^p)} \quad (6.2)$$

This equation has shown capability to describe the plastic behaviour of nickel free high nitrogen steels as well as 316L and 316 LN with different nitrogen contents at room

temperature and at a certain constant strain rate, Soussan *et al.* (1991) and Hua-bing *et al.* (2007). An extended hardening model proposed by Ludwik, Bergström and Hallén (1982), is given by

$$\sigma = \sigma_0 + K\varepsilon^p \quad (6.3)$$

where σ_0 are the yield strength, K and n are material constants.

A commonly used model, particularly for high strain rates, is the Johnson and Cook model. Temperature and strain-rate effects are included in the model. It is a multiplicative composition of a strain-hardening term, strain-rate sensitivity term and a thermal-softening term. The flow yield stress is given by

$$\sigma = \left(A + B\varepsilon^n \right) \left(1 + C \ln \dot{\varepsilon}^* \right) \left(1 - T^{*m} \right) \quad (6.4)$$

where ε is the equivalent plastic strain, $\dot{\varepsilon}^* = \dot{\varepsilon} / \dot{\varepsilon}_0$ is the dimensionless plastic strain rate, $\dot{\varepsilon}_0$ is the reference plastic strain rate, T^* is the homologous temperature defined as

$$T^* = \frac{T - T_r}{T_m - T_r} \quad (6.5)$$

where T_r is the reference temperature at which yield stress is measured and T_m is the melting temperature of the material, Johnson and Cook (1983). The five parameters, A , B , C , m and n are determined by means of curve fitting. Some optimized values from different researchers are presented in Table 6.1 for AISI 316L stainless steels, Umbrello *et al.* (2007).

Table 6.1 – Optimized values of the Johnson and Cook parameters that been presented by different researchers for the AISI 316L stainless steel, Umbrello *et al.* (2007)

	A	B	C	n	m	$\dot{\varepsilon}_0$
1	305	1161	0.01	0.61	0.517	1
2	305	441	0.057	0.1	1.041	1
3	301	1472	0.09	0.807	0.623	0.001
4	280	1750	0.1	0.8	0.85	200
5	514	514	0.042	0.508	0.533	0.001

However there exist several modifications of Johnson-Cook models. Andrade *et al* incorporated a fourth term with in order to consider dynamic recrystallization, Meyers *et al.* (2002). For increased strain rate sensitivity following modified model has according to Rule and Jones (1998) been proposed

$$\sigma = \left(A + B\varepsilon^n \right) \left(\dot{\varepsilon}^* \right)^\alpha \left(1 - T^{*m} \right) \quad (6.6)$$

where α is an empirical exponent. However, the strain rate sensitivity is not significantly enhanced so Rule and Jones (1998) proposed a revised model

$$\sigma = \left(C_1 + C_2\varepsilon^n \right) \left(1 + C_3 \ln \dot{\varepsilon}^* + C_4 \left(\frac{1}{C_5 - \ln \dot{\varepsilon}^*} - \frac{1}{C_5} \right) \right) \left(1 - T^{*m} \right) \quad (6.7)$$

for increased strain-rate sensitivity in regimes where needed while keeping the strain-rate behaviour in satisfactory regimes. Huang and Liang (2003) proposed a modification in the thermal-softening term according to

$$\sigma = \left(A + B\varepsilon^n \right) \left(1 + C \ln \dot{\varepsilon}^* \right) \left(D - ET^{*m} \right) \quad (6.8)$$

6.2 Physically based models

The physically based models are named after how they have been developed. They can be divided into explicit or implicit physical models. Explicit physical models include evolution equations for internal variables that represent some physics to predict the flow stress changes. An example of this is discussed in the next chapter. In implicit models the constitutive equation is determined based on the knowledge about the physical process but in the end only variables as strain and temperature are used in the model. Typically, the effective plastic strain is used as a variable for the flow stress evolution. A well-known implicit physical based model is the Zerilli-Armstrong model. Zerilli and Armstrong (1987) noticed a difference in the area of activation between bcc and fcc metals and proposed two different models in order to take into account the observed different behaviour of fcc and bcc metals. Both models include a thermal and an athermal term. A third term was added in order to take in account the grain size dependence. The fcc-model is given by

$$\sigma = \Delta\sigma'_G + C_2 \bar{\varepsilon}^{1/2} e^{(-C_3 T + C_4 T \ln \dot{\varepsilon}^p)} + k g^{-1/2} \quad (6.9)$$

where g is the average grain size diameter, $\Delta\sigma'_G$, k , C_2 , C_3 , C_4 is material parameters. However the derivation process of the Zerilli and Armstrong model contains some inconsistencies according to Voyiadjis and Abed (2005).

Chapter 7

Dislocation density based model

Dislocations and their movements and interaction with the microstructure have a crucial role in plastic deformation as described earlier. A dislocation density model based on assuming that this is the dominating mechanism for plastic deformation is formulated in the current chapter.

This model is also called a mechanism or phenomenological based model. The model uses the dislocation density and vacancy concentration as internal state variables for calculation of the evolution of the flow stress structure. The basic variant of the dislocation model used in papers B, C, D and E is presented below. A strain rate dependent model of subcell formation is used in paper F and also some other alternative relations are evaluated there. Kinematics hardening, twinning, recrystallization are among phenomena not accounted for in any of the models.

7.1 Flow stress

Plastic deformation of metals and alloys can be regarded as the process of motion and accumulation of dislocation under rate controlled deformation mechanisms. The distortion of the lattice due to existing dislocations and other defects makes it more difficult to move dislocations, i.e. drive a plastic deformation. The flow stress to move dislocations through the crystal lattice within the thermally activated region may be split into a long range component and a short range component. The short range component is associated with obstacles that may be overcome by thermal activation while the long range component is essentially temperature independent and is usually named athermal. Other type of phenomena as dislocation drag may also intervene the motion of dislocations. In the current work it is assumed that the macroscopic flow stress is given by three additive components according to

$$\sigma_y = \sigma_G + \sigma^* + \sigma_{drag} + \dots \quad (7.1)$$

where σ_G denotes the long range component, σ^* denotes the short range component and σ_{drag} accounts for phonon and electron drag. The dots denote other possible contributions that are ignored in the current work or accommodated via initial dislocation density. Most notable for the current work is the Hall-Petch effect due to grain size that is not assigned a separate term. The first component, σ_G , is due to the dislocation substructure. The second component, σ^* , is the explicit rate dependent stress contribution needed for the dislocation to pass through the lattice and to pass short-range obstacles where thermal activation may assist to overcome these obstacles. The opposing long-range stress component is written as

$$\sigma_G = m\alpha Gb\sqrt{\rho_i} \quad (7.2)$$

where m is the Taylor orientation factor, α is a proportionality interaction factor, G is the temperature dependent shear modulus, b is the magnitude of Burgers' vector and ρ_i is the immobile dislocation density. The proportionality interaction factor is a calibration parameter though a dislocation density dependent proportionality interaction factor is used in paper F. The basic mechanism of dislocation glide for plasticity is a shearing process. Usually, the fundamental relations used in the current model are expressed in terms of shear stress and strain. The Taylor factor translates the effect of the resolved shear stress in different slip system into an effective stress quantity for a polycrystal without texture. It depends on the kind of lattice in the metal. It does change with deformation but this is neglected in the current work.

When the dislocations are moving through the lattice, they encounter obstacles. It is assumed that the time for the dislocation to move from one obstacle to another, the flight time, is small compared to the waiting time. The frequency of successful jumps to overcome the obstacles is related to the probability that the energy level exceeds the needed activation energy for bypassing the obstacles which may be described by an Arrhenius expression. The mean velocity is therefore given by the kinetic equation, Frost and Ashby (1982)

$$\bar{v} = \beta b v_a e^{-\Delta G / kT} \quad (7.3)$$

where β is a dimensionless constant, b is the magnitude of Burgers' vector, v_a is the attempt frequency related to the oscillations in the lattice, ΔG is the activation energy, k is the Boltzmann constant and T is the absolute temperature. The plastic strain rate and the velocity of the dislocation motion is related via the Orowan equation

$$\dot{\epsilon}^p = \frac{\rho_m b \bar{v}}{m} \quad (7.4)$$

where ρ_m is the mobile dislocation density. Combining equations 7.3-7.4 gives

$$\dot{\epsilon}^p = \frac{\rho_m \beta b^2 v_a}{m} e^{-\Delta G / kT} = f(\sigma) e^{-\Delta G / kT} \approx \dot{\epsilon}_{ref} e^{-\Delta G / kT} \quad (7.5)$$

The motion of the dislocations in thermally activated glide is facilitated by the contribution of thermal activation energy. Hence, if the stress in itself is insufficient to drive the dislocation pass an obstacle thermal energy may help. The required energy to overcome an obstacle depends on its energy barrier, the magnitude and the profile. When the dislocation has reached x_1 in Figure 7.1 additional energy is needed to overcome the barrier and to reach x_2 . The required thermal energy is the total energy minus the mechanical energy.

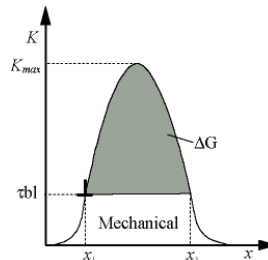


Figure 7.1 – Profile of obstacles resistance.

A general expression for the activation energy, Kocks *et al.* (1975), is given by

$$\Delta G = \Delta F_0 \left[1 - \left(\frac{\sigma^*}{\sigma_{ath}} \right)^p \right]^q \quad 0 \leq p \leq 1, \quad 1 \leq q \leq 2 \quad (7.6)$$

where ΔF_0 is the free energy in order to overcome the obstacles, σ_{ath} is the required athermal flow stress for passing the obstacles, p and q determining the shape of the barrier. The free energy and the required athermal flow stress can be written $\Delta F_0 = \Delta f_0 G b^3$ and $\sigma_{ath} = \tau_0 G$ respectively. Some guidelines regarding Δf_0 and τ_0 are given in Table 7.1 where l denotes the mean spacing between the obstacles. Combination of equation 7.5 and 7.6 gives after rewriting the short-range stress component

$$\sigma^* = \tau_0 G \left[1 - \left[\frac{kT}{\Delta f_0 G b^3} \ln \left(\frac{\dot{\epsilon}^{ref}}{\dot{\epsilon}^p} \right) \right]^{1/q} \right]^{1/p} \quad (7.7)$$

where $\dot{\epsilon}^{ref}$ is the reference strain rate.

Table 7.1. Activation energy factor and shear strength for different obstacles, Frost and Ashby (1982).

Obstacle strength	Δf_0	τ_0	Example
Strong	2	$> \frac{b}{l}$	Strong precipitates
Medium	0.2-1.0	$\approx \frac{b}{l}$	Weak precipitates
Weak	< 0.2	$<< \frac{b}{l}$	Lattice resistance

Dynamic strain aging (DSA) is a phenomenon that is commonly observed in metals containing solute atoms. It manifests as an increase in the dislocation glide resistance. Following the approach in Lindgren *et al.* (2008) the short-range component is written

$$\sigma^* = \tau_0 G f_{DSA} \left[1 - \left[\frac{kT}{f_{DSA} \Delta f_0 G b^3} \ln \left(\frac{\dot{\epsilon}^{ref}}{\dot{\epsilon}^p} \right) \right]^{1/q} \right]^{1/p} \quad (7.8)$$

where f_{DSA} is the dynamic strain aging function according to

$$f_{DSA} = \sqrt{1 + \sum_y \frac{c^y - c_0^y}{c_0^y}} \quad (7.9)$$

where y denotes the solute atom, c^y is the solute concentration in the dislocation core and c_0^y is the bulk solute concentration. Another formulation of the short-range component that not only dependent explicitly on strain and temperature but also on dislocation density is used in paper F.

Dissipative forces that counteract motion of dislocations are considered by the third component in equation 7.1. Following Frost and Ashby (1982) the viscous drag component is written

$$\sigma_{drag} = G \left(C_e + C_p \frac{T}{300} \right) \dot{\epsilon}^p \quad (7.10)$$

where C_e and C_p are coefficients related to electron and phonon drag, respectively.

7.2 Evolution of immobile dislocation density

The basic components for the yield stress in equation 7.1 are obtained from equation 7.2, 7.8 and 7.10. Additional equations for the evolution of the immobile dislocation density are however needed. These are described within this section. The evolution of the microstructure is considered to consist of a hardening and a recovery process. Hardening may be characterised by an immobilisation process and recovery may be described by re-mobilisation and annihilation processes. The used model assumes that the mobile dislocation density is stress and strain independent and much smaller than the immobile ones, Cheng *et al.* (2001) and Bergström (1983). Hence the evolution equation is written

$$\dot{\rho}_i = \dot{\rho}_i^{(+)} - \dot{\rho}_i^{(-)} \quad (7.11)$$

where index i denotes the immobile dislocations.

7.2.1 Hardening

The mobile dislocations may during their movements become immobilized or annihilated. In this context they are assumed to move an average distance Λ (mean free path) before immobilization or annihilation. The mean free path depends on the distribution of the obstacles as well as their types. It is well known that grain boundaries acts as both obstacles and sinks but subcells may also act as obstacles and prevent the motion of dislocations. Here the mean free path is assumed to be a combination of the distance between grain boundaries, g , and dislocation subcell diameter, s , as

$$\frac{1}{\Lambda} = \left(\frac{1}{g} + \frac{1}{s} + \text{others} \right) \quad (7.12)$$

where "others" denotes possible contributions from varying types of obstacles like precipitates. Holt (1970) showed that energetically clustering into cell structure is favoured and suggested that the cell diameter is given by

$$s = K_c \frac{1}{\sqrt{\rho_i}} + s_\infty \quad (7.13)$$

where K_c is a calibration parameter and s_∞ is an added term for the lowest limit. This measure can advantageously be interpreted as an average measure of the effect of the LEDS on the mean free path than just a geometric measure of subcells. Results from the literature e.g. by McQueen and Hockett (1970) and Korbel and Swiatkowski (1972) have however shown that the cell size is affected by the strain rate. An alternative formulation is addressed in article F. The density of mobile dislocations is via Orowan's equation related to the plastic strain rate. Therefore, the increase of the immobile dislocation density is assumed to be proportional to the plastic strain rate, Bergström (1983), according to

$$\dot{\rho}_i^{(+)} = \frac{m}{b} \frac{1}{\Lambda} \dot{\epsilon}^p \quad (7.14)$$

7.2.2 Recovery

Recovery is associated with annihilation of dislocation, reduction in stress and reduction in energy level. A mobile dislocation may for example be annihilated by other mobile or immobile dislocation or through interaction with grain boundaries, Bergström (1970). Vacancies have also an influence on the recovery process since they may diffuse towards dislocations where annihilation and/or remobilization of dislocations may occur by e.g. climb. However, different processes may contribute to the reduction in dislocation density. Bergström (1983) formulated a relation where the remobilization of dislocations is proportional to the immobile dislocation density according to

$$\dot{\rho}_i^{(-)} = \Omega \rho_i \dot{\epsilon}^p \quad (7.15)$$

where Ω denotes a recovery function which may be dependent on temperature and strain rate. A temperature and strain rate dependent formulation is used in paper F based on Bergström (1983).

Diffusions of vacancies influence the recovery. Militzer *et al.* (1994) used following formulation, which also is similar to the formulation in Siwecki and Engberg (1996), for recovery by climb

$$\dot{\rho} = 2D_v^* \frac{Gb^3}{kT} \rho^2 \quad (7.16)$$

where D_v^* denotes the effective diffusivity coefficient. The recovery process in Li (1966) was formulated according to

$$\dot{\rho}_i^{(-)} = \Omega(\rho_i^2 - \rho_{eq}^2) \quad (7.17)$$

where ρ_{eq} is an equilibrium value towards the density goes to. Based on equation 7.16 and 7.17 the recovery equation by climb, used here, is written as

$$\dot{\rho}_i^{(-)} = 2c_\gamma D_v \frac{c_v}{c_v^{eq}} \frac{Gb^3}{kT} (\rho_i^2 - \rho_{eq}^2) \quad (7.18)$$

where c_v^{eq} is the thermal equilibrium vacancy concentration, c_v is the fraction of vacancies, D_v is the self-diffusion coefficient and c_γ is a calibration parameter. The self-diffusion coefficient can according to Reed-Hill and Abbaschian (1992) be written as

$$D_v = a^2 \nu e^{\frac{\Delta S_{vm} + \Delta S_{vf}}{k}} e^{-\frac{Q_{vm} + Q_{vf}}{kT}} = D_{v0} e^{-\frac{Q_v}{kT}} \quad (7.19)$$

where a is the lattice constant, ν is the lattice vibration frequency, ΔS_{vm} is the increase in entropy due to motion of vacancy, ΔS_{vf} is the increase in entropy when forming a vacancy, Q_{vm} is the energy barrier for vacancy motion and Q_{vf} is the activation energy for vacancy formation.

7.2.3 Generation and migration of vacancies

Vacancies are important in that sense it enables random shift of atoms in a close packed structure and by this way render diffusions and non-conservative motion of jogs and hence

may by this both obstruct and facilitate motion of dislocations. Vacancy is considered to be the predominant mechanism for diffusions, Jastrzebski (1987), which is the most fundamental processes that controls the rate at which transformation occurs, Porter and Easterling (1992).

By the proposed model by Militzer *et al.* (1994) the excess vacancy can be modelled based on a generation and an annihilation component. Rewriting the equation where the temperature changes and the subcell evolution are considered gives

$$\dot{c}_v^{ex} = \dot{c}_v - \dot{c}_v^{eq} = \left[\chi \frac{\sigma b}{Q_{vf}} + \zeta \frac{c_j}{4b^2} \right] \frac{\Omega_0}{b} \dot{\bar{\epsilon}} - D_{vm} \left[\frac{1}{s^2} + \frac{1}{g^2} \right] \left(c_v - c_v^{eq} \right) + c_v^{eq} \left(\frac{Q_{vf}}{kT^2} \right) \dot{T} \quad (7.20)$$

where D_{vm} is the diffusion coefficient for vacancy migration, Ω_0 is the atomic volume, χ is amount of the mechanical work spent on vacancy generation and ζ is the neutralization effect by vacancy emitting and absorbing jogs with the following restrictions

$$\begin{cases} 0.5 - \zeta_0 c_j & \text{if } c_j \leq 0.5 / \zeta_0 \\ 0 & \text{if } c_j > 0.5 / \zeta_0 \end{cases} \quad (7.21)$$

Militzer *et al.* (1994) assumed $\chi = 0.1$ and $\zeta = 10$. The concentration of thermal jogs is given by

$$c_j = e^{-\frac{Q_{fj}}{kT}} \quad (7.22)$$

where the activation energy of jog formation, Q_{fj} , is approximately given by

$$Q_{fj} = \frac{Gb^3}{4\pi(1-\nu)} \quad (7.23)$$

The diffusion coefficient for vacancy migration is given by

$$D_{vm} = D_{vm0} e^{-\frac{Q_{vm}}{kT}} \quad (7.24)$$

where D_{vm0} is the frequency factor.

The rate of change in equilibrium concentration is only due to change in temperature as

$$\dot{c}_v^{eq} = c_v^{eq} \left(\frac{Q_{vf}}{kT^2} \right) \dot{T} \quad (7.25)$$

The equilibrium concentration of point defects as mono-vacancy at a certain temperature may by Haasen (1996) be written as

$$c_v^{eq} = e^{\frac{\Delta S_{vf}}{k}} e^{-\frac{Q_{vf}}{kT}} = c_{v0} e^{-\frac{Q_{vf}}{kT}} \quad (7.26)$$

where ΔS_{vf} and Q_{vf} is the increase in entropy during creation of a vacancy and the activation energy for vacancy formation respectively.

7.2.4 Diffusion of solutes

A number of diffusional processes can arise at elevated temperatures e.g. diffusion of solutes towards or away from dislocations, grain boundaries and free surfaces. But diffusion may also

take place along defects and defects are intimately related to plastic deformation. The diffusivity has shown be impressionable by the degree of deformation and according to Kothari and Vook (1992) the mass transport by diffusion is directly related to the density of dislocation and grain boundaries. In general, the grain boundary diffusivity is larger than the dislocation diffusivity which in turn is larger than lattice diffusivity, Kothari and Vook (1992), According to the model used here for the DSA phenomena the effect of solutes on mobile dislocations is only assumed to depend on lattice diffusion of Ni and Cr. The lattice diffusion coefficient is written

$$D_l^y = D_{l0}^y e^{-\frac{Q_x^y}{kT}} \quad (7.27)$$

where y denotes the diffusing atom, D_{l0}^y is the pre-exponential factor and Q_x^y is the activation energy for diffusion. Following Lindgren *et al.* (2008), the ratio in the DSA function is written

$$\frac{c^y - c_0^y}{c_0^y} = \left(\frac{c_s^y}{c_0^y} - 1 \right) \left(1 - e^{-\left(h^y \frac{D_l^{y*} \dot{\epsilon}_{ref}}{b^2 \dot{\epsilon}^p v_a} \right)^\xi} \right) \quad (7.28)$$

where c_s^y is a saturation value, c_0^y is the bulk concentration of the solute, h^y is a calibration parameter and ξ is 1/3 for pipe diffusions and 2/3 for lattice diffusion. The latter value is used here. The non-equilibrium lattice diffusion coefficient is assumed to be proportional to the equilibrium concentration of vacancies according to

$$D_l^{y*} = \frac{c_v}{c_v^{eq}} D_l^y \quad (7.29)$$

7.3 Stress update algorithm

Plastic strain is not used as an internal state variable in this model, as in most plasticity models. Instead the material model has two rate dependent state variables, the immobile dislocation density and the vacancy concentrations, that takes into account microstructural evolution and hence refer to past history. The subcell size was used as a third variable in paper F. Hence, we have a rate-dependent yield surface in context of rate-independent plasticity. The stress state should always stay on the yield surface during plastic deformation. This consistency condition is used to compute the increment in effective plastic strain in the radial-return stress update algorithm. It requires calculation of the yield stress and the hardening modulus for the current iteration of the plastic strain and the internal state variables. This section intends to describe how these are solved and how the hardening modulus for good convergence towards the yield surface can be computed.

The evolution of the internal state can be summarised by the following set of two coupled differential equations:

$$\dot{\rho}_i = \left(\frac{m}{b\Lambda} - \Omega \rho_i \right) \dot{\epsilon}^p - 2c_\gamma D_v \frac{c_v}{c_v^{eq}} \frac{Gb^3}{kT} (\rho_i^2 - \rho_{eq}^2) \quad (7.30)$$

$$\dot{c}_v = \left[\chi \frac{\Omega_0}{Q_{vf}} (\sigma_y) + \varsigma \frac{c_j}{4b^2} \frac{\Omega_0}{b} \right] \dot{\bar{\epsilon}}^p - D_{vm} \left(\frac{1}{s^2} + \frac{1}{g^2} \right) (c_v - c_v^{eq}) + c_v^{eq} \left(\frac{Q_{vf}}{kT^2} \right) \dot{T} \quad (7.31)$$

Assuming a constant strain rate, $\dot{\bar{\epsilon}} = \Delta \bar{\epsilon}^p / \Delta t$, during the increment the evolution equation can be written as

$$H_1 = \Delta \rho_i - \left(\frac{m}{b\Lambda} - \Omega \rho_i \right) \Delta \bar{\epsilon}^p + 2c_\gamma D_v \frac{c_v}{c_v^{eq}} \frac{Gb^3}{kT} (\rho_i^2 - \rho_{eq}^2) \Delta t = 0 \quad (7.32)$$

$$H_2 = \Delta c_v - \left[\chi \frac{\Omega_0}{Q_{vf}} (\sigma_y) + \varsigma \frac{c_j}{4b^2} \frac{\Omega_0}{b} \right] \Delta \bar{\epsilon}^p + D_{vm} \left(\frac{1}{s^2} + \frac{1}{g^2} \right) (c_v - c_v^{eq}) \Delta t - c_v^{eq} \left(\frac{Q_{vf}}{kT^2} \right) \Delta T = 0 \quad (7.33)$$

This set can be written in a vector form as

$$\mathbf{H} = \mathbf{0} \quad (7.34)$$

Linearization of the system gives

$$\mathbf{H}_{(i)} + \frac{\partial \mathbf{H}_{(i)}}{\partial \mathbf{q}} \cdot \delta \mathbf{q} = \mathbf{0} \quad (7.35)$$

Where the subscript i is an iteration counter and \mathbf{q} is a vector containing the internal state variables

$$\mathbf{q}^T = (\rho_i \ c_v) \quad (7.36)$$

The iterative changes in the internal state variables can now be computed as

$$\delta \mathbf{q} = - \left[\frac{\partial \mathbf{H}_{(i)}}{\partial \mathbf{q}} \right]^{-1} \cdot \mathbf{H}_{(i)} \quad (7.37)$$

When the iterative changes are small enough the iterations are terminated and the internal state variables are updated as

$$\mathbf{q}_{(i+1)} = \mathbf{q}_{(i)} + \delta \mathbf{q} \quad (7.38)$$

The hardening modulus, used for the iteration towards the yield surface in the radial-return logic as well in the consistent tangent matrix, is defined as

$$H' = \frac{d\sigma_y(\mathbf{q})}{d\bar{\epsilon}^p} = \frac{\partial \sigma_y}{\partial \mathbf{q}} \cdot \frac{d\mathbf{q}}{d\bar{\epsilon}^p} \quad (7.39)$$

Chapter 8

Determination of mechanical properties at high strain rates

Evaluation of the mechanical behaviour of metals and alloys are important and can be done by different methods and machines. Machines for mechanical testing have been available for a long time. Already in 1886 was the first commercially machine introduced, ASM handbook (2000). The machines have since then been gradually developed from pure mechanical machines to more advance electromechanical and servo hydraulic machines with advanced control system in order to meet the changing demands. Furthermore, sensors and software has also been developed. Today there exist several different methods with different range of applications and limitations. This section will briefly describe some of the available methods used for high strain testing.

Available techniques are summarized in Figure 8.1. Quasi-static testing and creep testing belongs to the category with isothermal conditions and where the inertia forces are negligible. Special servo hydraulic machines, Split-Hopkinson techniques and light gas gun driven impact belongs to the group for testing at higher strain rates where inertia forces become more significant and where adiabatic conditions arise. However, the inertia effects become more pronounced as the loading rate increases, increasing strain rates. The basic and important distinction between quasi-static testing and testing at high strain rates is the prominent inertial and wave propagation effects at the latter. The area where the inertial forces are important to consider is according to Hokka (2008) and Vuoristo (2004) divided into intermediate strain rates, high strain rates and very high strain rates. Conventional testing with screw or servo hydraulic machines are mainly used for quasi-static tests in strain rates range 10^{-4} - 1 s^{-1} Hokka (2008) while Taylor tests, Split Hopkinson Pressure Bar tests (SHPB) and expanding ring tests are used for high strain rates where inertial forces most likely needs to be accounted for. Machines for conventional testing are usually designed with a moving crosshead and an immobile load cell. How the load is applied to the crosshead differs but it is usually applied through a hydraulic cylinder or a screw. Irrespective of load-applying mechanism the speed and the force of the crosshead are limited due to different reasons. Designs for increased crosshead speeds make it more difficult to extract sufficient force. Though servo hydraulic machines equipped with adapted high-capacity valves can reach strain rates of 200 s^{-1} , ASM handbook (2000), or strain rates up to even 500 s^{-1} can be reached with special servo hydraulic machines, Hokka (2008) and Vuoristo (2004). Dynamic tensile test with strain rates up to 200 s^{-1} has successfully been performed with a new special developed dynamic servo hydraulic machine, Boyce and Dilmore (2009). Tests at these dynamic strain rates are difficult and challenging since the inertial and wave propagation effects become more prominent. The elastic stress wave propagates through the specimen, load cell and the frame with the effects

that several phenomena as inhomogeneous and time dependent oscillations stress field in the specimen and time dependent oscillations in measured force can appear, Boyce and Dillmore (2009).

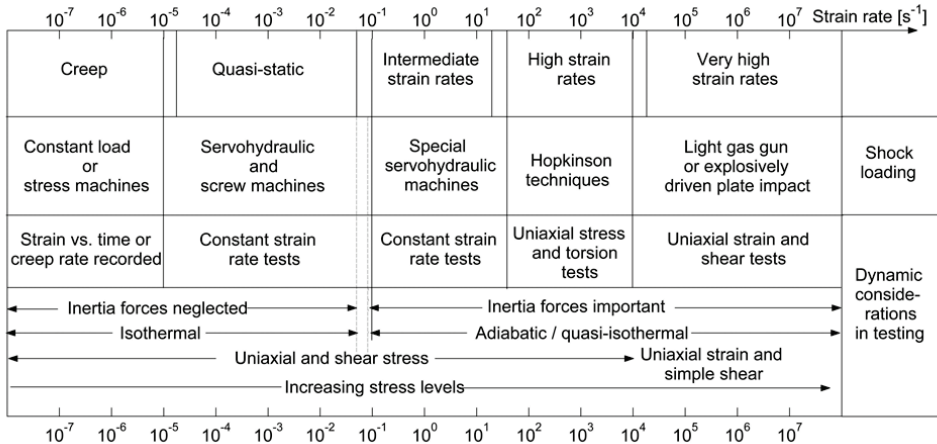


Figure 8.1 – Strain rate region, suitable testing technique and conditions for experiments, ASM handbook (2000).

8.1 Expanding ring test

Expanding ring test is a method for determine the tensile stress-strain relation at strain rates of $\sim 10^4 \text{ s}^{-1}$ or more. As the name implies the method is based on expanding a ring in its radial direction. Explosive or electromagnetic loading is placed in the centre of the ring and used to accelerate and expand the ring, see Figure 8.2. High-speed cameras or laser interferometers can be used to record the deformation. The advantage of the method is the ability of generating stress-strain data at really high strain rates. However to continuously keep the strain rate has shown to be difficult. The strain rate is high at the beginning when the strain is small but as the strain increases the strain rate decreases. Another drawback of the method is the radial compressive load, which in certain cases may be so large affecting the stress-strain results, ASM handbook (2000). The method is naturally limited to tensile strains.

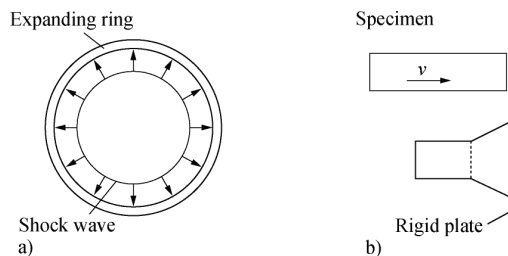


Figure 8.2 – a) Expanding ring test and b) classic Taylor test.

8.2 Taylor impact tests

The Taylor test is a test method where a cylindrical specimen is accelerated and impacts a rigid plate. The specimen undergoes a plastic deformation that is nonuniform, see Figure 8.2. During the impact with the stiff plate the highly deformed region emits elastic and plastic stress waves. The subsequent analysis is based on one-dimensional rigid-plastic analyses, where the waves propagate with different velocities and the interaction of the generated waves forms a transition area like a truncated cone. By knowing the fractional change of the length of the specimen the dynamic yield strength can be determined.

However, the obtained deformation pattern of the rod after the impact does not always correspond to the simplified theory, especially for a high velocity impacts. The deformed part in the front part shows a mushroom shape. Furthermore, the transition zone from the plastically deformed and the undeformed area may not be sharp and obvious, Meyers (1994). However, Wilkins and Guinan refined the analysis and were able to predict the relation between the deformed geometry and the plastic properties with better correspondence to experimental data, Meyers (1994). Erlich *et al* developed the classical Taylor technique even further by introducing improvements which lead up to a better method for obtaining the stress-strain flow curve under high strain rate, 10^4 - 10^5 s⁻¹, loading ASM handbook (2000).

8.3 Machining tests

Different approaches have, according to Sartkulvanich *et al.* (2005), been proposed in order to determine the flow stress data via machining tests. Guo (2003) used, for example, cutting tests for estimation of average flow stress at a range of large strains and high strain rates by use of Merchant's and Oxley's theories and conventional compression tests in order determine flow stress at moderate strains and strain rates. By this he overcame the difficulties of using cutting tests to determine flow stress data at moderate strains and strain rates. The Johnson-Cook plasticity model was then calibrated to fit the data from both the compression tests and the cutting tests. Özel and Altan (2000) used a FEM-based iterative approach in order to simultaneously determine the flow stress of the workpiece material and the friction conditions at the chip-tool contact. Flow stress at computed average strain rates and temperatures was determined by an iterative procedure until the difference between the calculated and measured cutting forces were small enough. The unknown friction coefficients were determined simultaneously using an additional iterative procedure.

8.4 Split-Hopkinson

The SHPB method is of particular interest in the current work as it has been used to evaluate the dynamic stress-strain behaviour of AISI 316L stainless steels. The results have thereafter been used for calibration of the material models in papers B, C, D, E and F. Split-Hopkinson technique for compression and tension testing is a method based on longitudinal elastic stress wave propagations through bars where the stress wave usually has been produced by a mechanical impact. Varying designs of respectively type exist. Devices for tensile testing are according to Hokka (2008) more challenging, especially high temperature testing. A tensile stress wave must be introduced and the specimen must be tightening to the bars without significantly influence the stress wave and in a way which render tensile deformation. Here follows a short history survey. The patent lawyer Bertram Hopkinson, eldest son of John Hopkinson who studied dynamic strength of wires, decided to carry on this father work, which tragically died in an accident in 1898, Clausen and Auestad (2002) and Professor Bertram Hopkinson. The work was extended to include impact on elastic bars. In 1914 he presented a technique to measure the shape of the stress pulse in an elastic bar, Split Hopkinson Pressure Bar Apparatus (2006). The idea of placing a specimen between two bars

and then impact it came much later. Hubert Kolsky was a man with a huge interest and a great influence in the research regarding characterization and quantitative measurements of material properties under sudden applied loads, Kinra and Wolfenden (1992). Shortly after the World War II, 1949, he invented a test equipment based on the idea of compressing a specimen between two bars by introducing a propagating compressive stress wave at one end, Split Hopkinson Pressure Bar Apparatus (2006). The test equipment is referred as the Kolsky bar but the far more common name is the Split-Hopkinson bars. Several variants have been developed during the following years. Ulric Lindholm was one of them that improved the technique in the early 1960 by for example modifying the length of the bars, the position of the strain gages and the launch of the striker, Split Hopkinson Pressure Bar Apparatus (2006). The Split-Hopkinson Pressure Bars is probably the far most common variant. It has been modified to generating tensile stresses as well shear stresses. The latter via a torsional Split-Hopkinson bars. An example of a design is shown in Cheim (1983). Harding *et al.* (1969) seems to be the first to describe a design for tensile testing, Clausen and Auestad (2002). The idea is to transform a compression wave into a tensile wave with the aim of accomplish the deformation work. A similar design but with an increased rise time of the tensile stress wave was proposed by Nicholas (1981), Clausen and Auestad (2002). Another approach where the tensile stress wave was introduced by pre-stressing part of the incident bar was proposed by Albertini and Montagnani (1976) and Staab and Gilat (1991), Clausen and Auestad (2002). The overall designs of the specimens are generally the same for compression testing and tensile testing respectively. Lindholm and Yeakley (1969) developed however a different design adjusted to a compressive stress wave in the incident bar. They introduced a hat-formed specimen, Clausen and Auestad (2002).

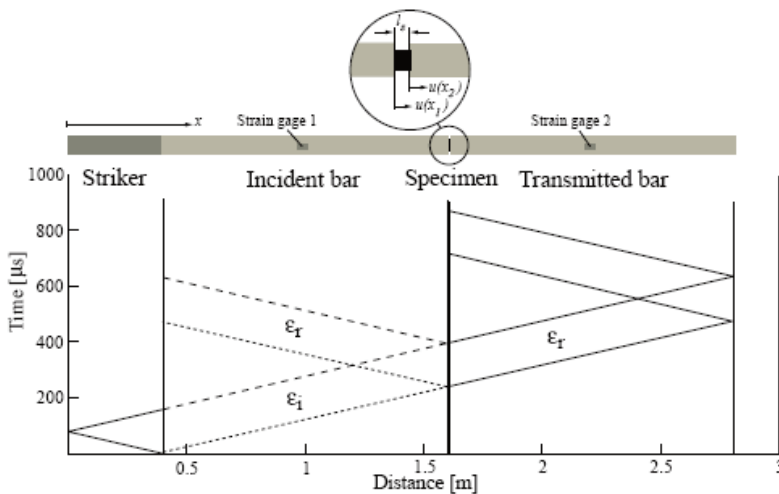


Figure 8.3 – Schematic sketch over a SHPB equipment showing wave propagation of the incident, reflected and transmitted waves.

A schematic configuration of compression testing is shown in Figure 8.3. The basic components are a striker, an incident bar, a transmitted bar and in some designs a third momentum trap bar. The latter is added to trap the reflected stress wave and prevent it to propagate back to interface between the specimen and the transmitted bar, Hokka (2008). The design is rather unpretentious at first sight. No gripping device, moving cross heads or load cell etc. The specimen is placed and sandwiched between two long bars, the incident and the

transmitted bar. A striker bar is accelerated to a certain velocity, impacting the incident rod and a compression stress wave is generated. Compressed air system is frequent used for accelerating the striker piston. The wave propagates through the incident bar towards the interface between the bar and the specimen, where the wave is partly reflected back while the remaining part is transmitted to the specimen and to the next interface for reflection and transmission to the transmitter bar. The propagating incident, reflected and the transmitted strain waves are measured via strain gages on the incident and the transmitter bars. The strain can then be translated into stress by Hooke's uniaxial law. Therefore and also for avoiding dispersion of the wave, these bars must behave elastic during the deformation. The distribution between reflected and transmitted energy depends on the acoustic impedance of the test specimen. In the case of ideal conditions, specimens of same material and diameter together with perfect alignment and contact conditions, then no reflections will appear at the interface between the different parts. The theory for evaluation of the measurements is given below.

8.4.1 Split Hopkinson - One dimensional wave equation

The displacement field in the bar is described by the well-known one-dimensional wave equation

$$\frac{\partial^2 u}{\partial x^2} = \frac{1}{c_0^2} \frac{\partial^2 u}{\partial t^2} \quad (8.1)$$

where x is the coordinate along the rod, u is the longitudinal displacement, t is time and c_0 is the wave propagation velocity, Graff (1975). The latter is defined as

$$c_0 = \sqrt{\frac{E}{\rho}} \quad (8.2)$$

where E is Young's modulus and ρ is the density. The solution of the wave equation is given by D'Alembert's solution according to

$$u(x, t) = f(x - c_0 t) + g(x + c_0 t) \quad (8.3)$$

where $f(x - c_0 t)$ and $g(x + c_0 t)$ correspond to a traveling wave in the increasing respective decreasing x -direction. Hence, the longitudinal displacement at a certain coordinate along the bar is given by superposition of two waves. The strain and the particle velocity in the bar may be derived from the expression for the displacement according to

$$\varepsilon(x, t) = \frac{\partial u}{\partial x} = f'(x - c_0 t) + g'(x + c_0 t) \quad (8.4)$$

respectively

$$v(x, t) = \frac{\partial u}{\partial t} = c_0 [-f'(x - c_0 t) + g'(x + c_0 t)] \quad (8.5)$$

The stress state in the bar, under elastic conditions, may be given by

$$\sigma(x, t) = E[f'(x - c_0 t) + g'(x + c_0 t)] \quad (8.6)$$

Evaluation of the equations for the displacement and the stress under assumption of only one propagating wave gives that a negative particle velocity corresponds to a positive stress wave according to

$$\sigma(x, t) = -\frac{E}{c_0} v(x, t) \quad (8.7)$$

Recall that reflection of waves may occur at discontinuities for e.g. at instantaneous cross section changes as in the case of a SHPB. Thus the incident stress wave is reflected and transmitted at the transition between the incident bar and the test specimen. Then one transmitted wave, moving in positive direction, and one reflected wave, moving in the negative direction, exists. A principled description of wave propagations in a transition is shown in Figure 8.4.

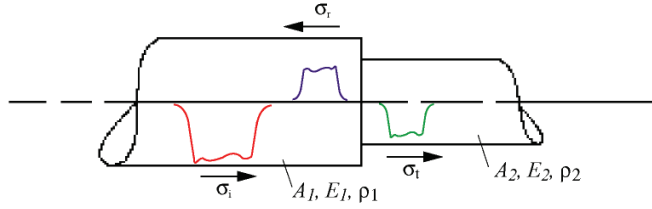


Figure 8.4 – Incident, reflected and transmitted waves at a transition.

Recall from equation 8.4 that the resulting strain field in a rod is based on two propagating waves in opposite direction. Hence the strain and the velocity in the incident rod at the left interface of the specimen, see Figure 8.3, is given by

$$\varepsilon(x_1, t) = \frac{\partial u}{\partial x} = f'(x_1 - c_0 t) + g'(x_1 + c_0 t) = \varepsilon_i + \varepsilon_r \quad (8.8)$$

respectively

$$v(x_1, t) = \frac{\partial u}{\partial t} = c_0 [-f'(x_1 - c_0 t) + g'(x_1 + c_0 t)] = c_0 (-\varepsilon_i + \varepsilon_r) \quad (8.9)$$

where index i and r denote incident and reflected wave. Integrating equation 8.9 gives the displacement at x_1 according to

$$u(x_1, t) = c_0 \int_0^t (-\varepsilon_i + \varepsilon_r) d\tau \quad (8.10)$$

Applying the same procedure for the transmitted bar gives the following relations for the right interface of the specimen

$$v(x_2, t) = -c_0 \varepsilon_t \quad (8.11)$$

$$u(x_2, t) = -c_0 \int_0^t \varepsilon_t d\tau \quad (8.12)$$

where index t denote the transmitted wave. The strain, strain rate and stress in the deforming specimen are given by

$$\varepsilon_s = \frac{u(x_1, t) - u(x_2, t)}{l_s} = \frac{c_0}{l_s} \int_0^t (-\varepsilon_i + \varepsilon_r + \varepsilon_t) d\tau \quad (8.13)$$

$$\dot{\varepsilon}_s = \frac{c_0}{l_s} (-\varepsilon_i + \varepsilon_r + \varepsilon_t) \quad (8.14)$$

$$\sigma_s = \frac{F(x_2, t)}{A_s} = \frac{E_0 A_0}{A_s} \varepsilon_t \quad (8.15)$$

where s is index for the specimen, l_s is length of specimen and A_s is area of the specimen. Introducing $-\varepsilon_i + \varepsilon_t = \varepsilon_r$ gives

$$\varepsilon_s = 2 \frac{c_0}{l_s} \int_0^t \varepsilon_r d\tau \quad (8.16)$$

$$\dot{\varepsilon}_s = 2 \frac{c_0}{l_s} \varepsilon_r \quad (8.17)$$

Equation 8.13 or 8.16 and 8.15 are used to compute the strain and stress in the specimen based on the recorded strains. Examples of recorded strains are shown in Figure 8.5.

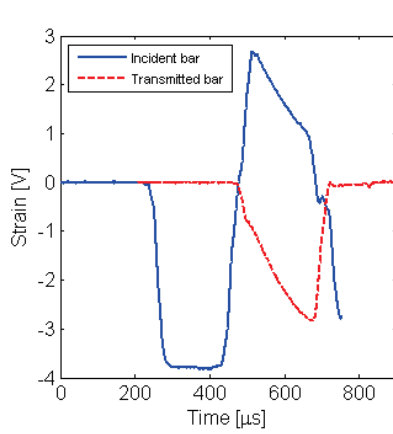


Figure 8.5 – Measured strain gages signal in the incident and transmitted bar.

8.4.2 Dispersion effects and corrections to the one-dimensional wave equation

The previous section showed the one-dimensional wave equation that is often used to evaluate SHPB. The created and propagating elastic stress wave from the impact of the striker and the incident slender bar would be expected to have a shape of a rectangular pulse of length $2L$ from this theory. In this case, L denotes the length of the striker. Strain gage measurements reveal however that a perfectly shaped rectangular pulse doesn't appear. The measured pulses do have a shape of a rectangular pulse but with significant oscillations, rounded corners and increased rise time. The one-dimensional wave theory ignores the radial expansions and contradiction of the bars. These lateral displacements influence the cross section and the stress distribution through the cross section. Radial constraint from the friction in the interface may also change the stress distribution. Also other types of elastic waves, e.g. spherical dilatational and surface waves, may be created due to the existing boundary conditions. The amplitude of the dilatational wave decreases however with the distance to such a degree that it vanish after a length of 10 diameter of the bar, Follansbee and Frantz (1983). Therefore, it is advantageous to place the strain gages at locations away from the ends. The generated surface waves trail behind the main wave caused by the impact and interacts continuously with it causing fluctuations in particle velocity, stress and strain and contribute to the oscillation in the measured pulse, Meyers (1994).

The created stress pulse is composed of a spectrum of frequencies, Meyers (1994), Hokka (2008), Vuoristo (2004) and Follansbee and Frantz (1983), where each frequency component travels at different velocity. It is known that low frequency components travel much faster than higher components. This results in retardation of the higher frequency components and a change of the propagating pulse during the propagation due to different velocities of the frequency components, i.e. dispersion occurs. The equation of motion for propagation of a sinusoidal wave in an infinitely long cylinder was independently solved by Pochhammer and Chree, Follansbee and Frantz (1983). The solution is in the literature mentioned as the Pochhammer and Chree solution but may also be referred as the frequency or dispersion equation, Follansbee and Frantz (1983). On basis on the theory from Pochhammer-Chree the ratio between the phase velocity c and the longitudinal wave velocity c_0 as function of the ratio between the bar diameter d_{bar} and pulse length Λ_{pulse} has been computed by Bancroft respectively Davies, Meyers (1994) and Vuoristo (2004). The results reveal that $c/c_0=1$ when the ratio d_{bar}/Λ_{pulse} coincides to 0, see Figure 8.6. But as the wavelength decreases the ratio c/c_0 decreases towards a plateau which coincides with Rayleigh waves. Thus, higher frequencies lead to higher degree of dispersion effects. The ratio d_{bar}/Λ_{pulse} has also an influence on the displacement field through the cross section. The longitudinal displacement profile is flat when the ratio $<< 1$, Follansbee and Frantz (1983).

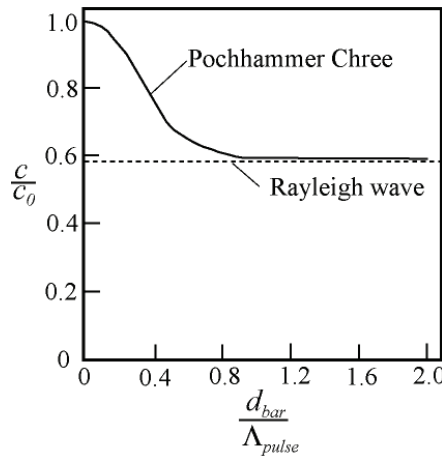


Figure 8.6 – Phase velocity as function of the ratio between the diameter of the bar and the wavelength.

The strains are usually measured some distance from the specimens for practical reasons. The pulse will change in shape as it travels due to the dispersion effect. Different methods are available for dispersion corrections e.g. the methods proposed by Bacon, Follansbee or Gorman, Hokka (2008). Basically the dispersion correction requires that the measured pulse at position z_0 is transformed from time domain to the frequency domain by a Fast Fourier Transform, FFT. The correction for dispersion for each frequency component is done in the frequency domain by a suitable operation. The measured pulse is thereafter transformed back to the time domain with an inverse FFT. The dispersion correction performed in Follansbee and Frantz (1983) lead to a smoother stress strain curve. The stress and strain within the specimen are directly related to the measured strains. If the dispersion corrections are not performed on the measured pulses the calculated stress-strain curves in the specimen may not reflect the true state. The curves may contain oscillations that are not representative.

Dispersion correction should be used in connection of evaluating the measured pulses in SHPB, Follansbee and Frantz (1983).

8.4.3 Geometric constraints on dimensions of test specimen in SPHB

The evaluation of the stress, strain and strain rate in the specimen in the SHPB method according to the one-dimensional theory described in section 8.4.1 assumes a homogenous uniaxial stress state in the test specimen. This also implies that it static equilibrium exists in the specimen. However the action from a force is not momentary transmitted to the rest of the body with the result that stress equilibrium is not immediately achieved. Stress waves propagate with finite velocities. But force equilibrium is usually obtained after the reflected wave has travel forth and back in the specimen some times. A short specimen compared to the wave length of the impact wave is a condition for assuming force equilibrium in the test piece. However, the friction in the interface between the bars and specimen and the inertia effect are besides the geometry other influencing factors.

The geometry of the specimen is important for reliable data in compression as well as tensile testing. If the specimen is to slim, high l_s/d_s ratio, buckling arise easily in compression testing. Shearing, double barrelling, barrelling and rapid localized expansion due to work softening are other deformation modes that can appear, ASM handbook (2000). Eccentric loading from e.g. non parallel end or die surfaces will leads to shearing. When the specimen is compressed it will expand but the friction in the interface will prevent the lateral flow at the loading surface. The material in midplane is not constrained, it expands and a barrelling shape occurs. Severe barrelling will occur if the frictional forces are too large. This causes an undesired multiaxial stress state in the specimen, Vuoristo (2004) and Hartley *et al.* (2007). The assumption of uniaxial homogenous stress states does no longer correspond to the actual stress state. Therefore the friction should be minimized since frictionless conditions lead to uniform radial and circumferential expansion with a homogenous stress state in the direction of the compression. Eliminating the friction and selection of a suitable l_s/d_s ratio are essential for obtaining a homogeneous uniaxial stress state. Friction can be minimized by appropriate lubricants. The film is however squeezed out when the force is high and metal to metal contact appears. Several designs have been utilized trying to maintain the film in the interface e.g. concentric circular grooves and a pocket ASM handbook (2000). l_s/d_s ratios less than 2.0 are often mentioned for reliable results and avoidance of buckling and shearing. When it comes to minimizing the friction errors the l_s/d_s ratio should according to ASTM E9, ASM handbook (2000), be within the interval $1.5 < l_s/d_s < 2.0$. The optimum ratio for SHPB test is however one-half of the most favourable ratio for test at low strain rates. Malinowski and Klepaczko found that the optimum ratio could be found from

$$\left(\frac{l_s}{d_s} \right)_{opt} = \left[\frac{2\mu\sigma_z}{\rho_s d_s^2 (\dot{\epsilon}^2 + \ddot{\epsilon})} \right]^{1/3} \quad (8.18)$$

where σ_z is the measured stress, ρ_s the density of the specimen, μ friction coefficient, Vuoristo (2004). High strength aluminium alloys and titanium should have a ratio of 1-1.5 while copper, nickel and aluminium should have a ratio of 0.5 to 1. Material with low strength should have a ratio less than 0.5.

The initial response of the specimen affects the stress results. A study by Bertholf and Karnes, Vuoristo (2004), regarding inertia and friction effects in SHPB tests showed that the inertia effects become more severe at high strain rates. This appears as increasing oscillations in the measured stress-strain curve. These oscillations can be reduced by increasing the rise time of the incident pulse, Vuoristo (2004) and Warren and Forrestal (2009). A pulse shaping material

is usually placed between the striker and the incident bar in order to increase the rise time. Davies and Hunter also studied the inertia effects, Vuoristo (2004). Following equation was presented taking the inertia effects into account

$$\sigma(t) = \sigma_m(t) + \rho_s \cdot \left(\frac{l_s^2}{6} - \nu_s \cdot \frac{d_s^2}{8} \right) \cdot \frac{\partial^2 \varepsilon(t)}{\partial t^2} \quad (8.19)$$

where σ_m is the measured stress, ρ_s the density, ν the Poisson's ratio, l_s the length of the specimen, d_s the diameter of the specimen, ASM handbook (2000) and Vuoristo (2004). The first term in bracket represents the correction for radial inertia effects while the second term accounts for the longitudinal inertia effects. Equation 8.19 shows that the inertia effects cancel out when the strain rate is constant or when the terms in bracket are zero. The latter gives the relation

$$\frac{l_s}{d_s} = \sqrt{\frac{3 \cdot \nu_s}{4}} \quad (8.20)$$

which for $\nu_s=0.3$ results in a ratio of $l_s/d_s=0.47$ for minimum inertia effects. Warren and Forrestal (2009) have recently studied the radial inertia effects for incompressible specimens. They found out that radial inertia effects can be neglected for steel specimens provided that dynamic force equilibrium is fulfilled. Radial inertia effects can however be important in soft materials.

Chapter 9

Distribution of work and summary of appended papers

This thesis consists of six papers, all in co-operation with other researchers. The author of this thesis had the main responsibility for planning, performing and evaluation of the experimental work including cutting force measurements, quick-stop measurements, microstructural examinations and high strain testing via SHPB. The author has taken part of writing in all articles and has also participated in and performed simulations and evaluations. **Paper A** was planned by Professor Lars-Erik Lindgren and he was the main responsible for writing. **Paper B** was planned in collaboration with co-authors, PhD Ales Svoboda was the main responsible for the simulations and the writing. **Paper C** was planned together with PhD Vahid Kalhori and he was the main responsible for the simulations and the writing. **Paper D** was planned by the author which also was main responsible for the theoretical work, calibration, evaluation and writing. **Paper E** was planned in collaboration with co-authors, PhD Ales Svoboda was the main responsible for the simulations while the author was the main responsible for calibration, evaluation and writing. **Paper F** was planned in collaboration with Professor Lars-Erik Lindgren, though the author was the main responsible for the theoretical work, calibration, evaluation and writing. A summary of the appended papers are given below.

9.1 Paper A

Verification and validation of machining simulations for sufficient accuracy
International Conference on Computational Plasticity 2009

Lars-Erik Lindgren, Dan Wedberg, Ales Svoboda

Simulation of metal cutting is known to be challenging in terms of numeric and physics. Any created model is supposed to reflect the real world phenomenon of interest with certain accuracy within the scope of the model. Therefore, verification and validation are essential. This is addressed in this article. Validation means checking of the accuracy of the model with respect to the real world behaviour. In the case of machining validation is usually done by studying the chip morphology from quick stop test, measurements of cutting forces and/or residual stresses and comparing with simulated results. Validation with respect to measured cutting forces is the most common and straightforward methods but far from trivial. For example, variations in material properties of the workpiece materials and the cutting edge radius of the cutting tools cause variations in the measured forces for nominally the same cutting case. An agreement between simulated and measured cutting forces within 10 % must therefore be deemed as good considering the common variations in real machining applications.

9.2 Paper B

Simulation of metal cutting using a physically based plasticity model
Modelling and Simulation in Materials Science and Engineering, 18, 2010

Ales Svoboda, Dan Wedberg, Lars-Erik Lindgren

A physically based dislocation density model (DD) and an empirical Johnson & Cook plasticity model (JC) are compared in this paper when used to simulate orthogonal cutting of SANMAC 316L. The latter model is one of the most commonly used material models for simulations of metal cutting. A sensitivity study was performed in order to examine the heat transfer contact coefficient. A value of $5 \times 10^6 \text{ W/m}^2\text{°C}$ showed to be realistic and subsequently used. A Coulomb friction model with a friction coefficient of $\mu = 0.5$, estimated as an average value from the whole range of cutting experiments, was used. The results from the simulations with the two models were compared with measured cutting forces and chip morphology. Quick-stop tests were evaluated with respect to shear plane angle and chip thickness. The predicted feed force was underestimated by the DD model of about 10 % compared to 15 % by the JC model. Largest deviation in prediction for the JC model was 20 % and 16 % for the DD model. The cutting forces were predicted slightly better by the DD model. The DD model also predicted the shear plane angle and chip thickness better.

9.3 Paper C

Simulation of mechanical cutting using a physical based material model
International Journal of Material Forming, 3, 2010

Vahid Kalhori, Dan Wedberg, Lars-Erik Lindgren

In this paper a physical based material model of SANMAC 316L stainless steel, as in paper B, is now also implemented in a finite element program AdvantEdge specialized for metal cutting simulations. This program is based on an explicit time stepping algorithm for solving the equation of motion. The interface between the cutting tool and the chip is divided into a sticking and a slipping region. A sensitivity study of the friction coefficient was performed. It turned out that there was no significant difference in force level for friction coefficients above 0.6. A value of 0.6 was therefore chosen. The predicted results were then compared with experimental measured results of cutting forces and chip morphology. The latter through comparison of shear plane angle and the ratio between cut and uncut chip thickness. The predicted cutting forces correspond well with the measured except for the feed force at a cutting speed of 100 m/min where the simulated feed force was 30 % lower. This deviation is believed to be due BUE. The same good agreement was not obtained regarding chip thickness ratio. One possible explanation of this may be that thermal softening is not sufficient to describe the chip formation adequately. A segmented chip form was however obtained. Results indicate of further investigation regarding influence of hardening rules.

9.4 Paper D

Predictive capability of constitutive model outside the range of calibration
International Conference on Computational Plasticity 2011

Dan Wedberg, Lars-Erik Lindgren

The chip formation process is associated with localized severe deformations accompanied by high local temperatures rise and the strain rate may reach values $> 50000 \text{ s}^{-1}$. Calibration of any material model is usually done by material testing covering the range of loading conditions relevant for the intended application. However, the maximum strain rate in machining is far beyond what can be reached with conventional mechanical material tests.

Therefore, reliable extrapolation outside the range of calibration is a highly wanted feature. It is known that, in many metals and alloys, the material behaviour at high strain rate differs considerably from that observed at low strain rates. The observed increased strain rate sensitivity has been interpreted to different mechanisms e.g. increased dominance of dislocation drag. An attempt to improve the predictability of a dislocation density model throughout the entire calibration range, which includes strain rates and elevated temperatures up to 9000 s^{-1} and $950 \text{ }^{\circ}\text{C}$ respectively, dislocation drag has been implemented. The predictive abilities outside as well as inside the calibration range of the empirical Johnson-Cook plasticity model (JC) and the dislocation density based model with dislocation drag (DD-drag) were compared and discussed with reference to AISI 316L stainless steel. The results showed that the JC model did not show the same good ability to reproduce the material data as the DD-drag model in the low strain rate region, with temperatures from room to $1300 \text{ }^{\circ}\text{C}$. Inclusion of dislocation drag improved the accuracy in the high strain rate, but still far from satisfactory, without any major changes within the low strain rates. Calibrated models, within high strain rate data, where also extrapolated to a strain rate range of $10000\text{-}50000 \text{ s}^{-1}$. The DD-drag model showed significant higher strain rate sensitivity than the J-C plasticity model. The results clearly show the difficulty of obtaining a comprehensive material model that predicts the material behaviour across the loading conditions that can occur in machining with good accuracy.

9.5 Paper E

Modelling high strain rate phenomena in metal cutting simulation

Modelling and Simulation in Materials Science and Engineering, 20, 2012

Dan Wedberg, Ales Svoboda, Lars-Erik Lindgren

The magnitude of strains and strain rates involved in metal cutting are extreme and are several orders higher than those generated from conventional material testing. Therefore extrapolation outside the calibration range without losing the accuracy is highly desirable. Two variants of a dislocation density based material model are used in this study to simulate orthogonal cutting of AISI 316L stainless steel. The calibration coefficients in the short range component were treated as temperature dependent in the first variant in order to fit the material behaviour up to 9000 s^{-1} . The other variant included instead dislocation drag in order to accommodate these high strain rates. The predicted material behaviour at low strain rates is good regardless of the variant. The dislocation drag component has a negligible contribution to flow stress at low strain rates. It was found that addition of dislocation drag improves the simulated results, cutting forces and chip morphology, somewhat but the addition of this phenomenon still does not make it possible to extrapolate reliably outside its calibration range. It was necessary to limit the used strain rate in the model to the highest value used in the calibration, else the drag term give a too large contribution to the cutting forces. This significant increase in flow stress resulting from the dislocation drag is likely to be counteracted by other softening mechanisms, e.g. recrystallization that is missing in the model. It was also found that the temperatures and strain rates in the primary deformation zone lie outside the region where dynamic strain ageing, DSA, occurs.

9.6 Paper F

Modelling flow stress of AISI 316L at high strain rates

Dan Wedberg, Lars-Erik Lindgren

An existing dislocation density model for AISI 316L, based on a coupled set of evolution equations for dislocation density and mono vacancy concentration, is extended into the high

strain rate regimes. The objective is to derive a constitutive material model of AISI 316L stainless steel covering the low and high strain regimes up to $\dot{\epsilon} \approx 10000 \text{ s}^{-1}$ at temperatures that can be obtained in machining, $\leq 900 \text{ }^{\circ}\text{C}$. Two mechanisms are evaluated with respect to their contribution in this respect. One is rate dependent cell formation. The other is dislocation drag due to phonon and electron drag. Furthermore, a temperature and strain rate dependent recovery and a proportionality interaction factor and a short range component that both depends on the dislocation density are also considered. High strain rate compression tests are performed using Split-Hopkinson technique at various initial temperatures. Experimental results are then used to calibrate the models via an optimization procedure. The main outcome of the evaluation of various flow stress models is that the flow stress behaviour of 316L is best modelled using the DD2 model with a rate dependent cell formation but without dislocation drag. Extrapolation to high strain rates based on the drag mechanism is not recommended until twinning and dynamic recrystallization are included.

Chapter 10

Results

The main research works in this thesis have focused on: (1) developing a dislocation density material model of AISI 316L stainless steel from a physical perspective that covers a temperature range and a strain rate range of 20-950 °C and 0.01-9000 s⁻¹ respectively. (2) FE-simulation of orthogonal cutting of AISI 316L where the usefulness of the calibrated material models was evaluated. Modelling is closely connected to theory and experiments and this work is no exception. This research work is based on a framework of experimental measurements for calibration and validation. They include SHPB-measurements, cutting force measurements, quick-stop measurements and some microstructural examinations. Some of the results are summarized below.

10.1 Results – material testing experiments

Dynamic compression tests were conducted of AISI 316L stainless steels at room and elevated temperatures by means of SHPB in order to characterize the material behaviour. It is easily seen in Figure 10.1 that the flow stress increases rapidly with increasing strain. Naturally, strain rate and temperature also affects the flow stress. The strain effects can be visualised using a plot of work-hardening rate vs. strain. An example is shown in Figure 10.2 for some selected stress-strain curves. It is observed that the strain-hardening rate is very high at the onset of deformation but it decreases immediately with increasing strain. The most prominent differences are the difference in work hardening rate at room temperature and elevated temperatures. Though the difference decreases and converges at a strain of ~0.45. The strain rate effects are better visualized in Figure 10.3-10.5 via a semi-logarithmic plot of flow stress at different constant plastic strain versus strain rate at different test temperatures. It is clear that the strain rate influences the flow stress response and that the influence is more evident under dynamic loading. Hence, two characteristic regions can be distinguished, regardless of temperature, with different strain rate sensitivities. The strain rate sensitivity in the high strain rate regions is much greater. The flow stress increases slowly first but then at strain rates >1000 s⁻¹ it increases much faster. Similar behaviour has been reported for other material as well. The temperature effect at a strain rate of ~3000 s⁻¹ and different strains can be seen more clearly in Figure 10.6. The temperature was not measured during the SHPB tests. Although, the reported temperature includes the temperature rise calculated assuming adiabatic heating. It was assumed that 90 % of the plastic work contributes to the increase in temperature. The results show that the flow stress decreases with increasing temperature without any visible weakening or peaks. Hence the effect of DSA seems to be non-existent at the strain rate of 3000 s⁻¹. Lindgren *et al.* (2008) performed tests at low deformation rates where they observed dynamic strain aging. It seems that solute atoms at their deformation rates and temperatures, have sufficient time to diffuse and thus impede the dislocation motion.

As the strain rate increases, higher temperatures are required to drive the solute atoms to the dislocations at sufficient speed. It can also be seen that the stress increase with strain, i.e. the hardening, decreases with temperature. The increase in the flow stress at room temperature is 67 % versus 49 % at an initial temperature of 950 °C when the plastic strain increases from 0.10 to 0.50. Figures 10.1-10.5 shows that the strengthening effect in the tested material varies with strain, strain rates and temperature.

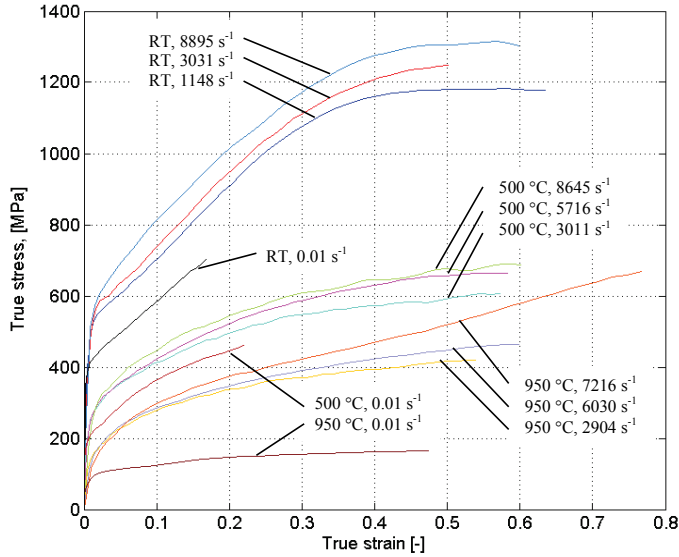


Figure 10.1 – True stress- strain curves.

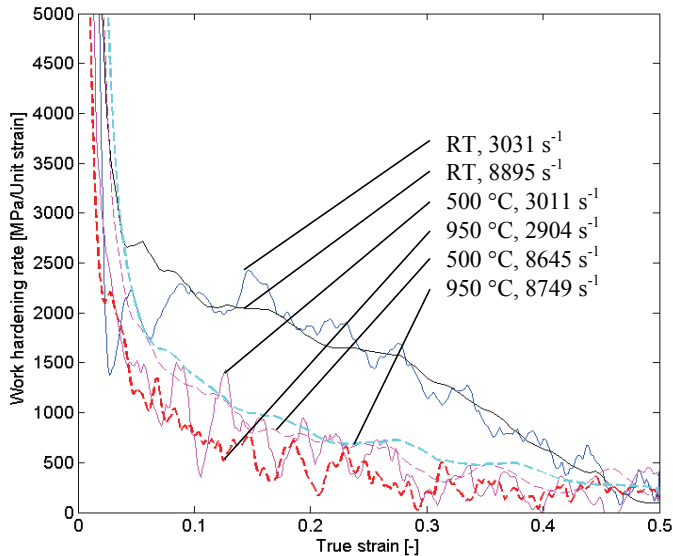


Figure 10.2 – Variation of work hardening rate as function of strain and strain rate.

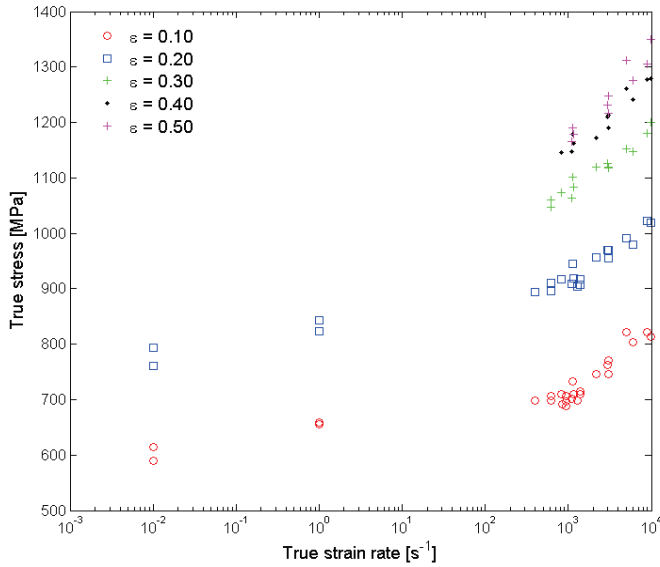


Figure 10.3 – Influence of strain rate on flow stress at various plastic strains at room temperature as initial temperature.

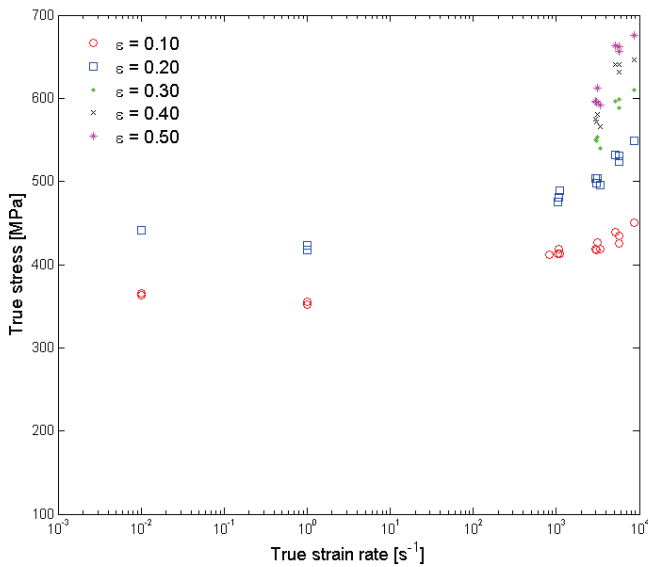


Figure 10.4 – Influence of strain rate on flow stress at various plastic strains at 500 °C as initial temperature.

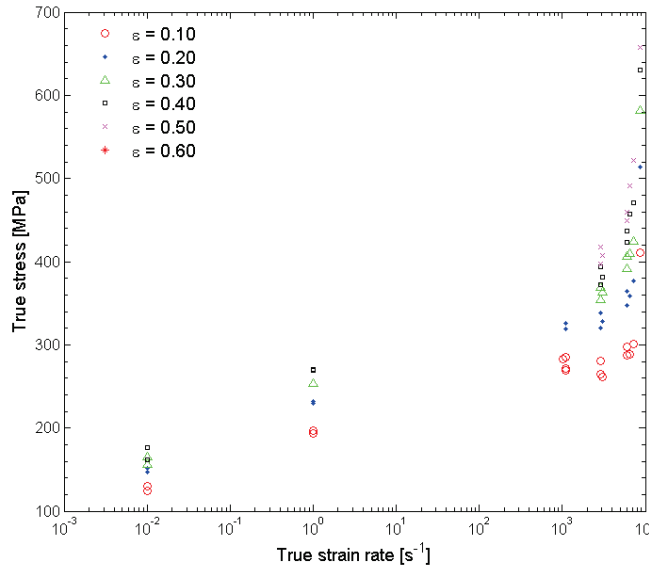


Figure 10.5 – Influence of strain rate on flow stress at various plastic strains at 950 °C as initial temperature.

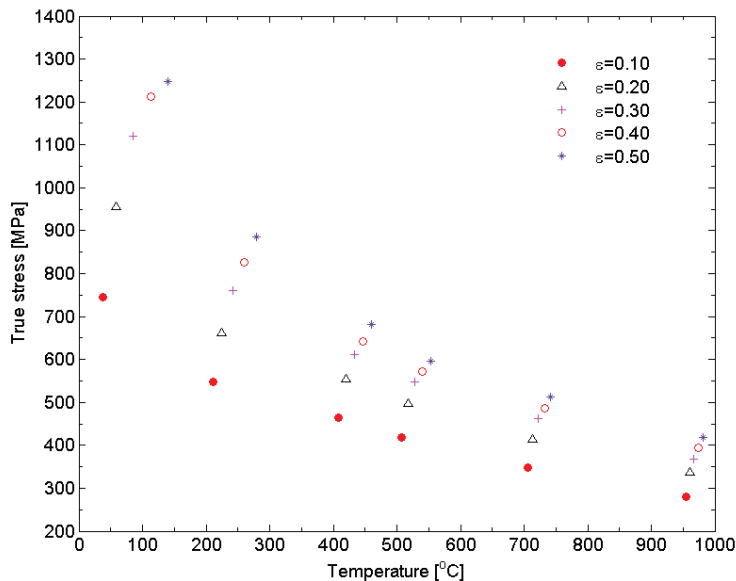


Figure 10.6 – Influence of temperature on flow stress for indicated strains at a strain rate of $\sim 3000 \text{ s}^{-1}$. Temperature rise due to adiabatic heating is taken into account.

The tendency to form α' -martensite depends highly on the chemical composition, temperature and strain rate. It is well known that austenitic stainless steels have a tendency of forming α' -martensite during deformation. This may enhance the work hardening. Experimental

measurements of the magnetic phase via magnetic balance were therefore preformed. The results are shown in Table 10.1. The proportion was lower than found in Lindgren *et al.* (2008) at low strain rates and room temperature. Though the nucleation of α' -martensite becomes more difficult when SFE increases, as it does with increasing temperature, the magnetic fraction seemed to increase somewhat with the temperature rise.

Table 10.1 – Measurement of magnetic phase

Test temperature	Strain rate	Strain	Fraction of magnetic phase	Temperature increase
(°C)	(s ⁻¹)	(-)	(%)	(°C)
22	-	-	0.254 ¹⁾	-
22	1406	0.25	0.483	44
22	2939	0.50	1.011	119
22	5582	0.62	1.191	139
22	8137	0.62	1.202	137
200	2942	0.55	0.251	88
400	2975	0.57	0.247	66

¹⁾ undeformed specimen

10.2 Results – material modelling

Metal cutting is a manufacturing process associated with large and rapid deformation. The strain and the strain rate can rise to more than 1 and 50000 s⁻¹ respectively in the primary and secondary deformation zones while the rest of the work-piece material deforms under more normal conditions. There is therefore a need for reliable material models that can predict the thermo-mechanical behaviour within a wide range of strains and strain rates. Earlier work by Lindgren *et al.* (2008) has shown that the dislocation density model reproduces the material behaviour of AISI 316L with an overall good agreement in the strain rate range from 0.01 to 10 s⁻¹ and from room temperature up to 1300 °C. Results within this work showed that the same good consistency is not obtained if this calibrated dislocation density model is extrapolated and compared with measured high strain rate data. This result indicates that new deformation mechanism enters and dominates as the strain rate increases. The so frequently used J-C plasticity model and its predictability has also been evaluated and compared within this work. It did not show the same consistency and hence predictability as the dislocation density model within the entire low strain rate data. The prediction of the thermo-mechanical behaviour at high strain rates was not good either when it was extrapolated. Re-calibration based on only high strain rate data resulted in a better agreement within this range but still not good and at the expense of poor conformity within the low strain rate range. This is shown in **paper D** together with results from a variant of the dislocation density model where dislocation drag is considered. The presence of dislocation drag effects at strain rates that occurs in metal cutting has been well established. Hence a model of this phenomenon was implemented followed by a re-calibration. The results showed that the results for high strain rates improved, but it is still unsatisfactory. It is although possible to get relatively good consistency within the high strain rate range if only this range is considered during the calibration. A much better agreement within the whole loading range was obtained when the dislocation density model was re-calibrated and where the calibration parameters in the short range term were made temperature dependent. The results are shown in Figure 10.7

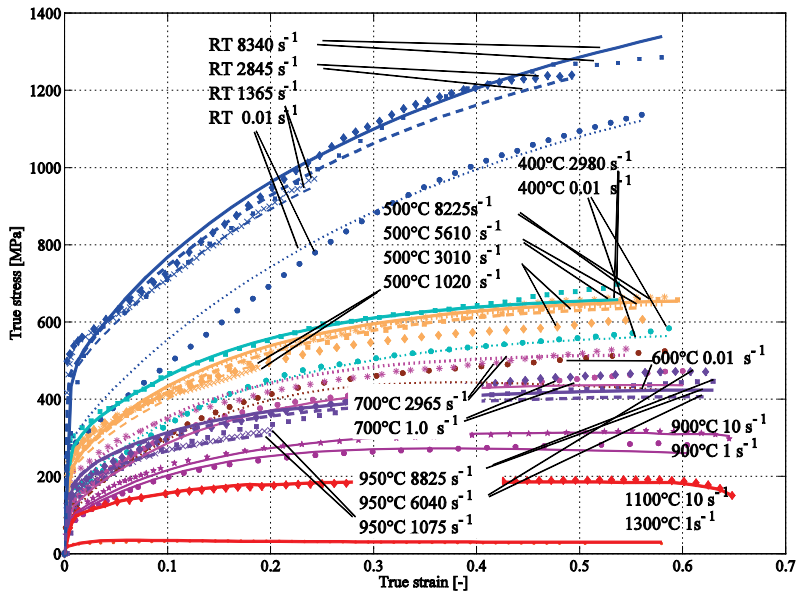


Figure 10.7 – Comparison between measured and predicted flow stress when the obstacle strength parameters were assumed to be temperature dependent.

The microstructure evolves during deformation. A three-dimensional cell structure is commonly observed where dislocations organize themselves into an interconnected network, cell walls, that enclose comparatively dislocation free regions. With this as background an equation for the cell size evaluation has been applied assuming that cell sizes decrease with increasing strain rate and dislocation density. Furthermore, evaluation of other mechanisms with respect to their contribution to the plastic deformation at high strain rates has been done in **paper F**. For instance, the arrangement of the dislocations has shown to affect the proportionality interaction factor. Therefore a dislocation density dependence proportionality interaction factor has also been considered. The recovery function has so far been temperature dependent. However, this also indicates of a strain rate dependency. Hence, a temperature and a strain rate dependent recovery function have been evaluated. An alternative description of the thermally activated stress component has also been considered where the short-range stress depends on the dislocation density. These phenomena together with dislocation drag have been evaluated in **paper F**. Best agreement proved the model where the cell size depends on temperature and strain rate, see Figures 10.8-10.9. The stress-strain curves agreed well within the high strain rate range. The predicted temperature sensitivity at $\sim 3000 \text{ s}^{-1}$ was also found to correlate well with experiment results shown in Figure 10.6. Though, it does also have problem, like the model in Lindgren *et al.* (2008), to accurately predict the behaviour in the DSA region, at 700 and 900 °C and low strain rates. Furthermore, along with increasing dislocation density the model predicts a corresponding decrease in cell size. More specifically the inverted subcell size increases proportionally with the square root of dislocation density, Figure 10.10a. It also implies that reduction in cell size will increase the flow stress. Figure 10.10b shows the cell size prediction with increasing strain rate within the dynamic strain rate range. The predictability did not change much if a dislocation density dependent proportionality interaction factor also was implemented. Adding a temperature and

a strain rate dependent recovery function did not improve the model. Neither did the model where dislocation drag in combination with a strain rate dependent function of the cell size, regardless if the thermally activated stress component was influenced or not of the dislocation density, was used. Though, dislocation drag has in **paper D** and **F** have a strong influence on the flow stress and the strain rate sensitivity outside the range of calibration, see Figure 10.11. This figure also shows a large discrepancy between the predicted flow stresses. This indicates that the reliability of extrapolation is uncertain as long as softening mechanisms like twinning and recrystallization are not included in the model as discussed in **paper F**. This is the reason why the strain rate used to evaluate the flow stress in **paper E** had to be limited.

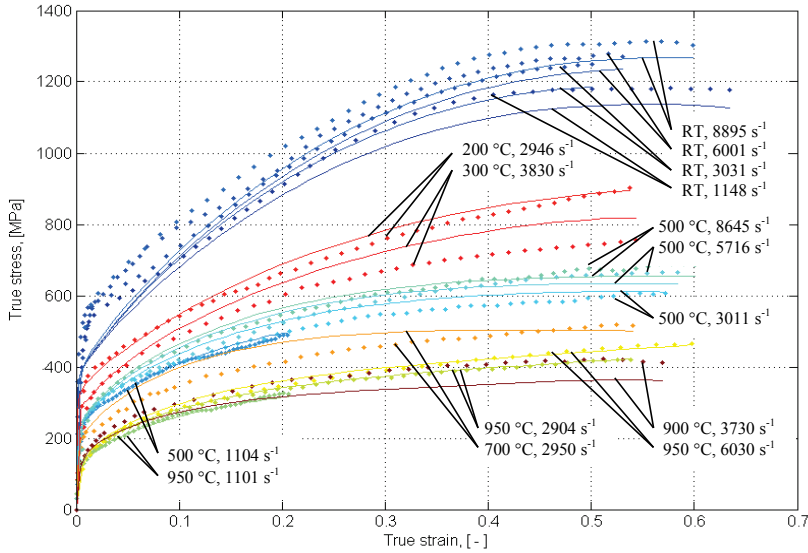


Figure 10.8 – Comparison between measured and predicted flow stress when a strain rate dependent model of cell size is used.

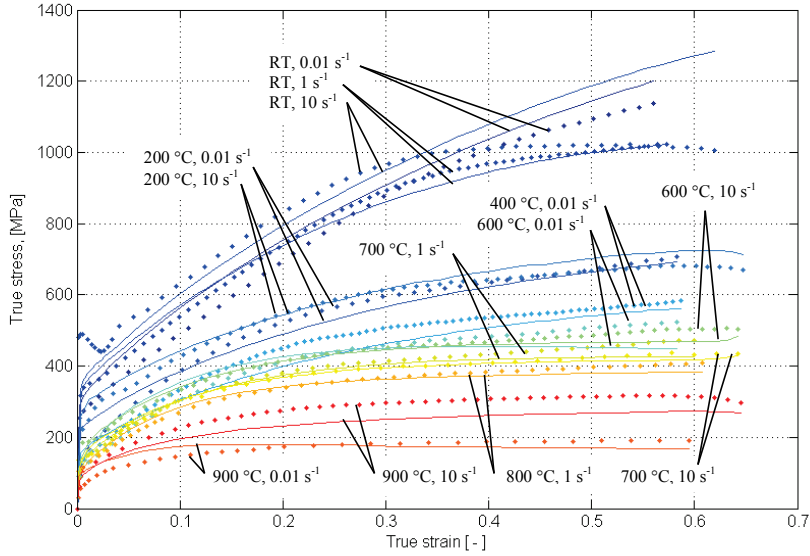
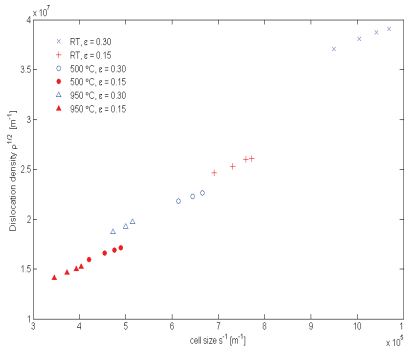
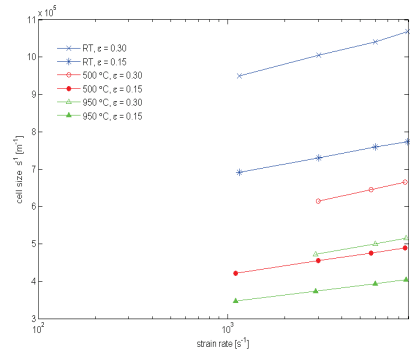


Figure 10.9 – Comparison between measured and predicted flow stress when a strain rate dependent model of cell size is used.



a)



b)

Figure 10.10 - Predicted response of model with integrated strain rate dependent function of the cell size, model DD2 in paper F, where a) shows how the root of dislocation density vary with the inverse of cell size and b) shows how the inverted cell size increases with logarithm of strain rate.

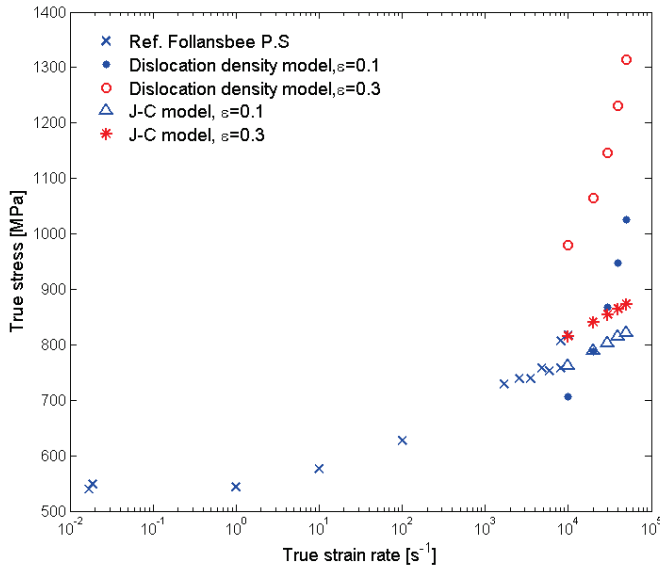


Figure 10.11 – Measured flow stress, Follansbee (1986), and predicted flow stress of the dislocation density model where dislocation drag is considered and the J-C plasticity model as function of strain rate at true strain of 0.10, 0.30 and room temperature. The dislocation density model and the J-C model are based on calibration at high strain rate data.

10.3 Results – simulation of metal cutting

Engineering material models such as J-C plasticity model are commonly used for description of workpiece material behaviour in commercial FE codes. Easy accessible data, easy to handle and simplicity are advantages frequently mentioned. This work shows, however, that physically based plasticity models can be implemented into FE-codes for simulation of orthogonal cutting. **Paper B**, **C** and **E** are all papers where orthogonal cutting has been analysed by means of an implemented variant of the dislocation density flow stress mode in either the finite element software MSC.Marc or AdvantEdge. The former uses an implicit time integration scheme while the latter uses an explicit. **Paper B** compares simulated cutting forces and chip morphology with experimental measurements when using a dislocation density model where the calibration parameters in the short range term were made temperature dependent and a J-C plasticity model. The calibrated dislocation density model is in **paper C** implemented in the software AdvantEdge. Two variants of the dislocation density based flow stress model are used in **paper E** in order to simulate orthogonal cutting. The first model has temperature dependent calibration parameters in the short-range component while instead dislocation drag is included in the other to better reproduce the workpiece material behaviour. Best agreement between simulated and measured cutting forces were obtained when using an updated Lagrangian formulation and an explicit time integration scheme in combination with a dislocation density model where the calibration parameters in the short range term were made temperature dependent. Furthermore the time stepping procedure in combination with the mesh refinement seems to be able to capture the chip segmentation quite well without damage evolution included. The results in **paper B** showed that the cutting forces were generally slightly better predicted by the dislocation density model compared to the J-C plasticity model although the feed forces were significantly better predicted. The

results from these simulations also showed that prediction of the chip morphology is somewhat more difficult than cutting forces. Furthermore because of large plastic strain and very high strain rate there is a significant temperature rise. DSA is a phenomenon that appears with a certain combination of strain rate and temperature. Results in **paper E** showed that the strain rate and temperature within the primary deformation zone lie outside the region where DSA occurs.

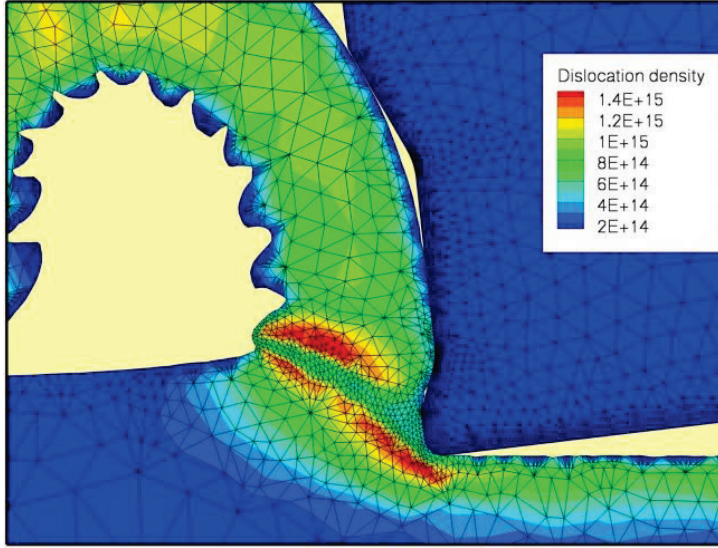


Figure 10.12 – Simulated results from paper C, $v_c=100$ m/min and $f_n=0.25$ m/min, showing dislocation density.

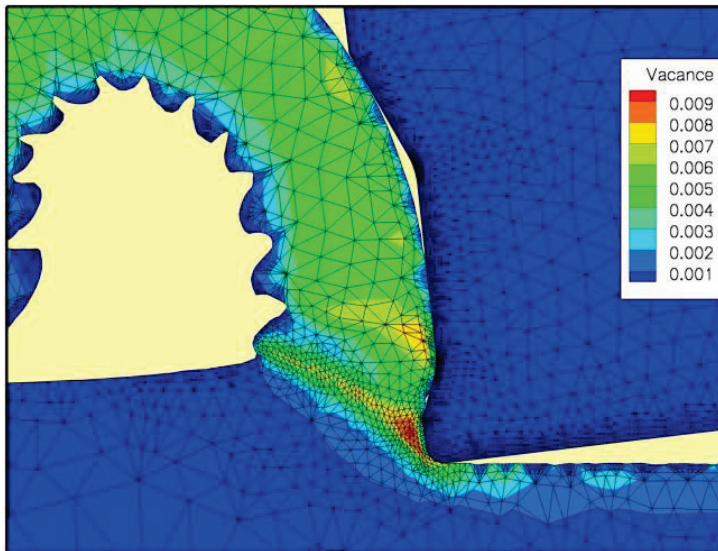


Figure 10.13– Simulated results from paper C, $v_c=100$ m/min and $f_n=0.25$ m/min, showing concentration of vacancies.

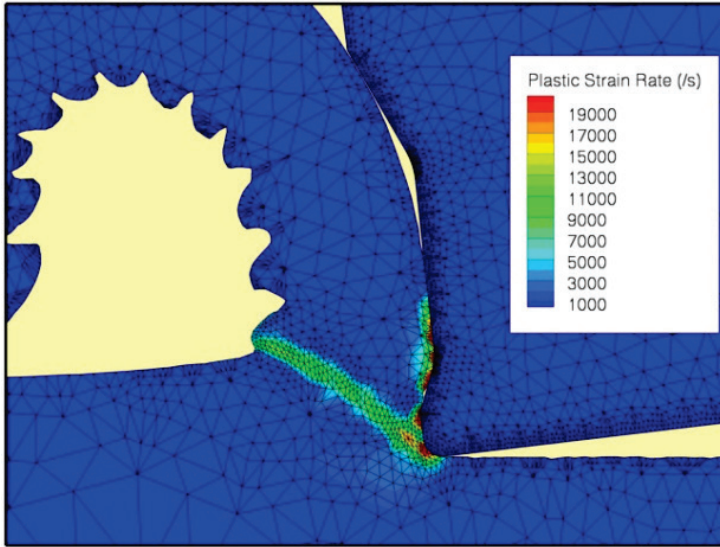


Figure 10.14 – Simulated results from paper C, $v_c=100$ m/min and $f_n=0.25$ m/min, showing strain rate.

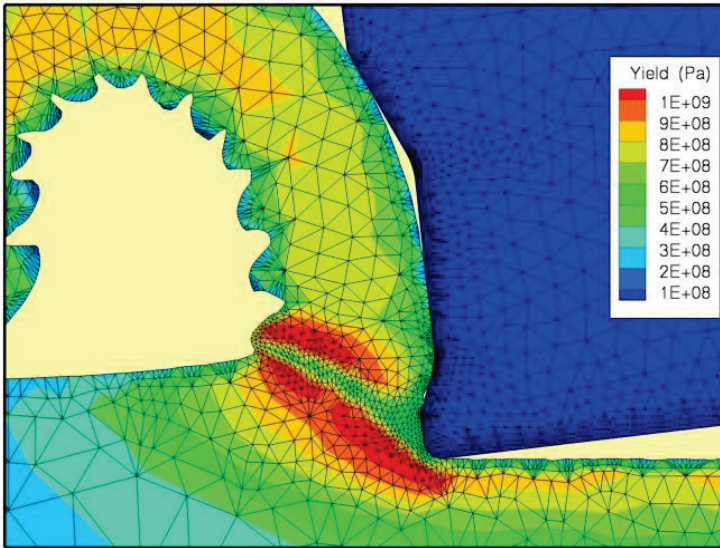


Figure 10.15 – Simulated results from paper C, $v_c=100$ m/min and $f_n=0.25$ m/min, showing yield stress.

10.4 Results – sufficient accuracy of models

Experimental measurements often serve to calibrate and validate models and needs therefore to be robust. Important properties and features for the outcome may vary in one way or another and hence influence it. For instance, properties of the work-piece material as well as geometric properties of the cutting insert may vary and influence the validation process. But simulations need also to be robust. Obtaining converged results from simulations with respect to the element size and time stepping can sometimes be difficult. Though using mesh and convergence criteria that capture local effects are important for the accuracy and hence will

inevitably affect the validation process. **Paper A** addresses these circumstances, viz, how variations in the work-piece properties for nominally the same material and the variation in edge radius due to tolerances in production influence the measured as well as computed cutting forces. This does also have a bearing on the validation process and the question about sufficient accuracy of models. The results showed, with respect to differences in work-piece material and cutting edge radius, that the cutting forces might vary within 1-24 %. Therefore the requirements to consider a model to be validated must consider the process variation within the industry.

Chapter 11

Conclusions

The noteworthy main conclusions from this thesis are:

- The experimental compressive tests of 316L stainless steel show typical features for variations with strain, strain rate and temperatures. Additional phenomena that have been observed may be due to dynamic strain aging and twinning. These phenomena together with recrystallization affect the flow stress also. The magnetic balance measurements indicate small or negligible martensite transformation and thus its effect is insignificant for temperatures from room temperature and higher.
- Modelling, calibration and validation have been carried out with an engineering Johnson-Cook (JC) plasticity model and various dislocation density (DD) based models. The most complete model, **paper F**, includes strain rate and temperature cell formation together with phonon drag. However, this model cannot be used outside the calibration range as the contribution to the flow stress due to drag increases too much with strain rate as found in **paper E**. Therefore, the recommended model excludes the drag mechanism.
- Advanced material models with several parameters can be calibrated, provided computer based tools are used in this process.
- Machining simulations can be done using the dislocation density model using commercial finite element codes with good agreement with measured forces and chip geometry.
- Validations are important and require robust experimental methods and simulations. The requirements to consider a model to be validated must consider the process variation within the industry. A deviation between the predicted and measured cutting forces of around 10 % is in this respect quite good.

Chapter 12

Future work

Within this work an existing dislocation density model for AISI 316L, based on a coupled set of evolution equations for dislocation density and mono vacancy concentration, is enhanced in order to accommodate plastic deformation at high strain rates. This comprises evaluation of different mechanisms with respect to their contribution in this respect. Furthermore, experimental work, thereof high strain rate compression via Split-Hopkinson technique, has been done to calibrate and validate these models. Still, extrapolation is needed when using the models in metal cutting simulations due to the extreme conditions in the primary and secondary deformation zone with large strain, $> 100\%$, and high strain rates, $> 50 \cdot 10^3 \text{ s}^{-1}$. At this very high strain rates viscous retarding effect, that impedes the motion of dislocations, has shown to have a great influence. However, dynamic recrystallization is a counteracting softening effect that has been observed in metal cutting. The twinning tendency has also been shown to be more prosperous at these very high strain rates. Furthermore, the observed difference in strain hardening rate, from the high strain rate testing, between the RT case and the higher temperatures is most probably due to mechanical twinning. Therefore the following is the recommendation for future work.

- a) Twinning is a competing deformation mechanism to slip and has shown to be more propensities to occur in low SFE materials. A model for the evolution of mechanical twinning and its influence on the flow stress should be developed and appended to the dislocation density model.
- b) Dynamic recrystallization is a softening effect that should be implemented.
- c) Material properties commonly vary between different batches. Evaluate robustness of processes by including statistical information on variation of material properties would be of interest.
- d) It is vital to have an understanding of the underlying physics in order to develop models. Hence, experimental tests as well as characterization of the microstructure evolution under relevant conditions are important. These experiments together with machining experiments are also important for calibration and validation of material and machining models.

13 References

- Asgari S., E. El-Danaf, S.R. Kalidindi and R.D. Doherty, 1997, Strain hardening regimes and microstructural evolution during large strain compression of low stacking fault energy fcc alloys that form deformation twins, *Metallurgical and Materials Transaction* **28A** 1781-1795.
- ASM handbook, Mechanical testing and evaluation, volume 8. Materials Park Ohio, 2000.
- Babu B., Physical Based Model for Plasticity and Creep of Ti-6Al-4V, Licentiate thesis, Department of Applied Physics and Mechanical Engineering, Luleå University of Technology, Luleå, 2008.
- Balaji A.K., G. Sreeram, I.S. Jawahir and E. Lenz, 1999, The effects of cutting tool thermal conductivity on tool-chip contact length and cyclic chip formation in machining with grooved tools, *Annals of the CIRP* **48** 33-38.
- Bergström Y., and H. Hallén, 1982, An improved dislocation model for the stress-strain behavior of polycrystalline α -Fe, *Materials Science and Engineering* **55** 49-61.
- Bergström Y., 1969/1970, A dislocation model for the stress-strain behaviour of polycrystalline α -Fe with special emphasis on the variation of the densities of mobile and immobile dislocations, *Materials Science and Engineering* **5** 193-200.
- Bergström Y., 1983, The plastic deformation of metals – a dislocation model and its applicability, *Reviews on powder metallurgy and physical ceramics* 79-265.
- Bolling G.F. and R.H. Richman, 1970, The plastic deformation-transformation of paramagnetic f.c.c Fe-Ni-C alloys, *Acta Metallurgica* **18** 673-681.
- Boothroyd G. and W.A. Winston, Fundamentals of machining and machine tools, third edition, CRC Press, Taylor & Francis Group, 2006.
- Bowen A.W. and P.G. Partridge, 1974, Limitations of the Hollomon strain-hardening equation, *Journal of Physics D: Applied Physics* **7** 969-978.
- Boyce B.L. and M.F. Dilmore, 2009, The dynamic tensile behavior of tough, ultrahigh-strength steels at strain rates from 0.0002 s^{-1} to 200 s^{-1} , *International Journal of Impact Engineering* **36** 263-271.
- Byun T.S., 2003, On the stress dependence of partial dislocation separation and deformation microstructure in austenitic stainless steels, *Acta Materialia* **51** 3063-3071.
- Cheim C.Y. and J. Duffy, 1983, Strain rate history effects and observations of dislocation substructure in aluminium single crystals following dynamic deformation, *Materials Science and Engineering* **57** 233-247.
- Cheng J., S. Nemat-Nasser and W. Guo, 2001, A unified constitutive model for strain-rate and temperature dependent behavior of molybdenum, *Mechanics of Materials* **33** 603-616.
- Chern G.-L., 2005, Development of a new and simple quick-stop device for study on chip formation, *International Journal of Machine Tools & Manufacture* **45** 789-794.
- Cheval F. and L. Priester, 1989, Effect of strain rate on the dislocation substructure in deformed copper polycrystals, *Scripta Metallurgica* **23** 1871-1876.
- Christian J.W. and S. Mahajan, 1995, Deformation twinning, *Progress in Materials Science* **39** 1-157.

Clausen A. H. and T. Auestad, Split-Hopkinson tension bar: experimental set-up and theoretical considerations. Report no. R-16-02, Norges Tekniska Naturvetenskapliga Universitet, Trondheim, 2002.

Dieter G.E. Mechanical Metallurgy, McGraw-Hill, 1988.

El-Danaf E., S.R. Kalidindi and R.G. Doherty, 1999, Influence of grain size and stacking-fault energy on deformation twinning in fcc metals, *Metallurgical and Materials Transactions* **30A** 1223-1233.

Fang N., I.S. Jawahir and P.L.B. Oxley, 2001, A universal slip-line model with non-unique solutions for machining with curled chip formation and a restricted contact tool, *International Journal of Mechanical Sciences* **43** 557-580.

Feaugas X., 1999, On the origin of the tensile flow stress in the stainless steel AISI 316L at 300 K: back stress and effective stress, *Acta Materialia* **47** 3617-3632.

Ferguson W.G., A. Kumar and J.E. Dorn, 1967, Dislocation damping in aluminum at high strain rates, *Journal of Applied Physics* **38** 1863-1869.

Follansbee P.S., 1986, High-strain rate deformation of FCC metals and alloys Metallurgical Applications of Shock-Wave and High-Strain-Rate Phenomena (edited by Murr K.P., Staudhammer K.P. and Meyers M.A.) 451-479 Marcel Dekker New York.

Follansbee P.S. and C. Frantz, 1983, Wave propagation in the Split Hopkinson pressure bar, *Journal of Engineering Materials and Technology* **105** 61-66.

Follansbee P.S. and U.F. Kocks, 1988, A constitutive description of the deformation of copper based on the use of the mechanical threshold stress as an internal state variable, *Acta Metallurgica* **36** 81-93.

Frost H.J. and M.F. Ashby, 1982, Deformation mechanism maps – The plasticity and creep of metals and ceramics, Pergamon Press (Oxford).

Galligan J.M., T.J. McKrell and M.T. Robson, 2000, Dislocation drag processes, *Materials Science and Engineering* **A287** 259-264.

Ganesh Sundra Raman S. and K.A. Padmanabhan, 1994, Tensile deformation-induced martensitic transformation in AISI 304LN austenitic steel, *Journal of Materials Science Letter* **13** 389-392.

Graff K.F., Wave motion in elastic solids, Oxford University Press, 1975.

Guo W.-G. and S. Nemat-Nasser, 2006, Flow stress of Nitronic-50 stainless steel over a wide range of strain rates and temperatures, *Mechanics of Materials* **38** 1090-1103.

Guo Y.B., 2003, An integral method to determine the mechanical behavior of materials in metal cutting, *Journal of Materials Processing Technology* **142** 72-81.

Haasen P., Physical Metallurgy, third edition. Cambridge University Press, 1996.

Hartley R.S., T.J. Cloete and G.N. Nurick, 2007, An experimental assessment of friction effects in the split Hopkinson pressure bar using the ring compression test, *International Journal of Impact Engineering* **34** 1705-1728.

Hecker S.S., M.G. Stout, K.P. Staudhammer and J.L. Smith, 1982, Effects of strain state and strain rate on deformation-induced transformation in 304 stainless steel: Part 1. Magnetic measurements and mechanical behaviour, *Metallurgical transactions* **13A** 619-626.

- Hedström P., Deformation induced martensitic transformation of metastable stainless AISI 310, Licentiate thesis, Department of Applied Physics and Mechanical Engineering, Luleå University of Technology, Luleå, 2005.
- Hokka M., Effects of strain rate and temperature on the mechanical behavior of advanced high strength steels, PhD thesis, Tampere University of Technology, Tampere, 2008.
- Holt D.L., 1970, Dislocation cell formation in metals, *Journal of Applied Physics* **41** 3197-3201.
- Honeycombe R.W.K and H.K.D. H. Bhadeshia, Steels microstructure and properties, second edition, R.W.K Honeycombe and H.K.D. H. Bhadeshia, 1995.
- Hua-bing L., J. Zhou-hua, Z. Zu-rui, X. Bao-yu, L. Fu-bin, 2007, Mechanical properties of nickel free high nitrogen austenitic stainless steels, *Proceedings of Sino-Swedish Structural Materials Symposium* 330-334.
- Huang Y. and S.Y. Liang, 2003, Cutting forces modeling considering the effect of tool thermal property-application to CBN hard turning, *International Journal of Machine Tools & Manufacture* **43** 307-315.
- Hull D. and D.J. Bacon, Introduction to dislocations, Butterworth-Heinemann, 2001.
- Humphreys F.J. and M. Harherly, Recrystallization and related annealing phenomena, second edition. Elsevier Ltd, 2004.
- Janecek M. and K. Tangri, 1995, The influence of temperature and grain size on substructure evolution in stainless steel 316L, *Journal of Materials Science* **30** 3820-3826.
- Jastrzebski Z. D., The nature and properties of engineering materials, third edition. John Wiley & Sons, Inc, 1987.
- Johnson G.R. and W.H. Cook, 1983, A constitutive model and data for metals subjected to large strains, high strain rates and high temperatures, *Seventh International Symposium on Ballistics* The Hague The Netherlands.
- Kaapor R. and S. Nemat-Nasser, 2000, Comparison between high and low strain-rate deformation of tantalum, *Metallurgical and Materials Transactions* **31A** 815-823.
- Kalhor V., Modelling and simulation of mechanical cutting, PhD thesis, Department of Mechanical Engineering, Luleå University of Technology, Luleå, 2001.
- Kinra V. K. and A. Wolfenden, M³D: Mechanics and mechanisms of material damping. American society for testing and materials, 1992.
- Kiritani M., T. Sota, T. Taware, H. Arimura, K. Yasunaga, Y. Matsukawa, M. Komatsu, 2002, Defect structures introduced in fcc metals by high-speed deformation, *Radiation Effects and defects in Solids* **157** 53-74.
- Kocks U.F., A.S. Argon and M.F. Ashby, Thermodynamics and Kinetics of slip, Progress in Material Science 19, Pergamon Press, 1975.
- Korbel A. and K. Swiatkowski, 1972, The role of strain rate in the formation of dislocation structure and its influence on the mechanical properties of aluminium, *Metal Science Journal* **6** 60-63.
- Kothari R. and R.W. Vook, 1992, The effect of cold work on surface segregation of sulfur on oxygen-free high conductivity copper, *Wear* **157** 65-79.

- Kuhlman-Wilsdorf D., 1989, Theory of plastic deformation:- properties of low energy dislocation structures, *Materials Science and Engineering* **A113** 1-41.
- Kumar A, F.E Hauser and J.E Dorn, 1968, Viscous drag on dislocations in aluminum at high strain rates, *Acta Metallurgica* **16** 1189-1197.
- Kumar A. and R.G. Kumble, 1969, Viscous drag on dislocations at high strain rates in copper, *Journal of Applied Physics* **40** 3475-3480.
- Lee W.-S. and C.-F. Lin, 2000, The morphologies and characteristics of impact-induced martensite in 304L stainless steel, *Scripta Materialia* **43** 777-782.
- Lee W.-S. and C.-F. Lin, 2001, Impact properties and microstructure evolution of 304L stainless steel, *Materials Science and Engineering* **A308** 124-135.
- Lee W.-S. and C.-F. Lin, 2002, Comparative study of the impact response and microstructure of 304L stainless steel with and without prestrain, *Metallurgical and Materials Transaction* **33A** 2801-2810.
- Lee W.-S. and C.-C. Chiu, 2006, Deformation and fracture behavior of 316L sintered stainless steel under various strain rate and relative sintered density conditions, *Metallurgical and Materials Transactions* **37A** 3685-3696.
- Lee W.-S. and H.-F. Lam, 1996, The deformation behaviour and microstructure evolution of high-strength alloy steel at high rate of strain, *Journal of Materials Processing Technology* **57** 233-240.
- Lesuer D. R., G.J. Kay and M.M LeBlanc, 2001, Modeling large-strain, high-rate deformation in metals, *Third Biennial Tri-Laboratory Engineering Conference Modeling and Simulation (Pleasanton)*.
- Li, J., Recrystallisation, Grain Growth and Texture. 1966: ASM.
- Lindgren L.-E., K. Domkin and S. Hansson, 2008, Dislocations, vacancies and solute diffusion in physical based plasticity model for AISI 316L, *Mechanics of Materials* **40** 907-919.
- Lubliner J., Plasticity theory, Dover Publications, 2008.
- Maalekian M. and E. Kozeschnik, 2010, Modeling the effect of stress and plastic strain on martensite transformation, *Materials Science Forum* **638-642** 2634-2639.
- Marshall P., Austenitic stainless steels – Microstructure and mechanical properties, Elsevier applied science publisher LTD, 1984.
- McQueen H. and J. Hockett, 1970, Microstructure of aluminium compressed at various rates and temperatures, *Metallurgical Transactions* **1** 2997-3004.
- Meyers M.A, Dynamic behavior of materials, John Wiley & Sons Inc, 1994.
- Meyers M.A., O. Vöhringer and V.A. Lubarda, 2001, The onset of twinning in metals: a constitutive description, *Acta Materialia* **49** 4025-4039.
- Meyers M.A., D.J. Benson, O. Vöhringer, B.K. Kad, Q. Xue, H.-H. Fu, 2002, Constitutive description of dynamic deformation. Physically-based mechanism, *Materials Science and Engineering* **A322** 194-216.
- Michel D., J. Moteff and J. Lovell, 1973, Substructure of type 316 stainless steel deformed in slow tension at temperatures between 21° and 816°C, *Acta Metallurgica* **21** 1269-1277.

- Militzer M., W.P. Sun and J.J. Jonas, 1994, Modelling the effect of deformation-induced vacancies on segregation and precipitation, *Acta Metallurgica et Materialia* **42** 133-141.
- Mohammed A.A.S, E.A. El-Danaf and A-K.A. Radwan, 2007, Equivalent twinning criteria for FCC alloys under uniaxial tension at high temperatures, *Materials Science and Engineering* **A457** 373-379.
- Moore D. F., Principles and application of tribology, A. Wheaton Co., Exeter, 1975.
- Murr L.E. and D. Kuhlmann-Wilsdorf, 1978, Experimental and theoretical observations on the relationship between dislocation cell size and dislocation density, residual hardness, peak pressure and pulse duration in shock-loaded nickel, *Acta Metallurgica* **26** 847-857.
- Murr L.E. and Staudhammer K.P., 1975, Effect of stress amplitude and stress duration on twinning and phase transformation in shock-loaded and cold-rolled 304 stainless steel, *Materials Science and Engineering* **20** 35-46.
- Murr L.E, K.P. Staudhammer and S.S Hecker, 1982, Effects of strain state and strain rate on deformation-induced transformation in 304 stainless steel: Part II. Microstructural study, *Metallurgical Transactions* **13A** 627-635.
- Nemat-Nasser S., W.-G. Guo and D.P. Kihl, 2001, Thermomechanical response of AL-6XN stainless steel over a wide range of strain rates and temperatures, *Journal of the mechanics and Physics of Solids* **49** 1823-1846.
- Porter D.A. and K.E. Easterling, Phase transformations in metals and alloys, second edition. CRC Press, 1992.
- Professor Bertram Hopkinson. Available from <http://www-g.eng.cam.ac.uk/125/1900-1925/hopkinson.html>.
- Olson G.B. and M. Cohen, 1972, A mechanism for the strain-induced nucleation of martensite transformation, *Journal of Less-Common Metals* **28** 107-117.
- Olson G.B. and M. Cohen, 1975, Kinetics of strain-induced martensitic nucleation, *Metallurgical Transactions* **6A** 791-795.
- Prinz F., A.S. Argon and W.C. Moffatt, 1982, Recovery of dislocation structures in plastically deformed copper and nickel single crystals, *Acta Metallurgica* **30** 821-830.
- Rao J.G. and S.K. Varma, 1993, The effect of grain size and strain rate on the substructures and mechanical properties in nickel 200, *Metallurgical Transaction* **A24** 2559-2568.
- Reed-Hill R.E. and R. Abbaschian, Physical metallurgy principles, PWS Publishing Company, 1992.
- Regazzoni G., U.F. Kocks and P.S. Follansbee, 1987, Dislocation kinetics at high strain rates, *Acta Metallurgica* **35** 2865-2875.
- Rémy L. and A. Pineau, 1978, Temperature dependence of stacking fault energy in close-packed metals and alloys, *Materials Science and Engineering* **36** 47-63.
- Ring Groth M., Adhesive bonding and weldbonding of stainless steel. Licentiate thesis, Department of Materials and Manufacturing Engineering, Luleå University of Technology. Luleå, 1998.
- Rule W.K. and S.E. Jones, 1998, A revised form for the Johnson-Cook strength model, *International Journal of Impact Engineering* **21** 609-624.

Sanchez J.C., L.E. Murr and K.P. Staudhammer, 1997, Effect of grain size and pressure on twinning and microbanding in oblique shock loading of copper rods, *Acta Materialia* **45** 3223-3235.

Saoubi R.M., J.C. Outeiro, B. Changeux, J.L. Lebrun, A.M. Dias, 1999, Residual stress analysis in orthogonal machining of standard and resulfurized AISI 316 steels, *Journal of Materials Processing Technology* **96** 225-233.

Sartkulvanich P, T. Altan and J. Soehner, 2005, Flow stress data for finite element simulation in metal cutting: A progress report on MADAMS, *Machining Science and Technology* **9** 271-288.

Seetharaman V. and R. Krishnan, 1981, Influence of the martenite transformation on the deformation behaviour of an AISI 316 stainless steel at low temperatures, *Journal of Materials Science* **16** 523-530.

Sencer B.H., S.A. Maloy and G.T. Gray III, 2005, The influence of shock-pulse on the structure/property behaviour of copper and 316L austenitic stainless steel, *Acta Materialia* **53** 3293-3303.

Shankaranarayan H. and S.K. Varma, 1995, Strain-rate and grain-size effects on substructures and mechanical properties in OFHC copper during tension, *Journal of Materials Science* **30** 3576-3586.

Shaw C.M., *Metal Cutting Principles*, Oxford Science Publications, 1997.

Shume A.J., Y.J. Chang and M.N. Bassim, 1989, A study of the effect of initial grain size and strain rate on dislocation structures in copper, *Materials Science and Engineering* **A108** 241-245.

Sieurin H., J. Zander and R. Sandström, 2006, Modelling solid solution hardening in stainless steels, *Materials Science and Engineering* **A415** 66-71.

Sil D. and S.K. Varma, 1993, The combined effect of grain size and strain rate on the dislocation substructure and mechanical properties in pure aluminium, *Metallurgical Transactions* **24A** 1153-1161.

Siwecki T. and Engberg G., 1996, Recrystallisation controlled rolling of steels *Thermomechanical Processing in Theory, Modelling & Practise* [TMP]² ed. B Hutchinson et al (Stockholm: The Swedish Society for Materials Technology), 121-44.

Soussan A., S. Degallaix and T. Magnin, 1991, Work-hardening behavior of nitrogen-alloyed austenitic stainless steels, *Materials Science and Engineering* **A142** 169-176.

Split Hopkinson Pressure Bar Apparatus. An historic mechanical engineering landmark. Designated by the American Society of Mechanical Engineers. Designation Ceremony Southwest Research Institute, Texas, 2006.

Staker M.R. and D.L. Holt, 1972, The dislocation cell size and dislocation density in copper deformed at temperatures between 25 and 700°C, *Acta Metallurgica* **20** 569-579.

Stouffer D.C. and L.T. Dame, *Inelastic deformation of metals: models, mechanical properties and metallurgy*. John Wiley & Sons, Inc, 1996.

Suenaga M and J.M. Galligan, 1971, The effect of the superconducting state on stress relaxation in lead-temperature dependence, *Scripta Metallurgica* **5** 63-70.

Swedish standards institute, SS-EN 10020: Definition and classification of grades of steel, SIS, 2000.

Swedish standards institute, SS-EN 10088-1:2005- Stainless steels-Part 1: List of stainless steels, SIS, 2005.

Talonen J. and H. Hänninen, 2007, Formation of shear bands and strain-induced martensite during plastic deformation of metastable austenitic stainless steels, *Acta Materialia* **55** 6108-6118.

Talonen J., P. Nenonen, G. Pape and H. Hänninen, 2005, Effect of strain rate on the strain-induced $\gamma \rightarrow \alpha'$ -martensite transformation and mechanical properties of austenitic stainless steels, *Metallurgical and Materials Transactions* **36A** 421-432.

Totten G.E., Steel heat treatment handbook -Steel heat treatment: metallurgy and technologies, second edition, CRC Press, Taylor & Francis Group, 2007.

Trent E.M., Metal cutting, third edition, Butterworth Heinemann Ltd, 1991.

Umbrello D., R. M'Saoubi and J.C. Outerio, 2007, The influence of Johnson-Cook material constants on finite element simulation of machining of AISI 316L steel, *International Journal of Machine Tools & Manufacture* **47** 462-470.

Varma S.K., J. Kalyanam, L.E. Murr and V. Srinivas, 1994, Effect of grain size on deformation-induced martensite formation in 304 and 316 stainless steels during room temperature tensile testing, *Journal of Materials Science Letters* **13** 107-111.

Vaz Jr. M., D.R.J. Owen, V. Kalhori, M. Lundblad, L.-E. Lindgren, 2007, Modelling and simulation of machining processes, *Arch. Comput. Methods Eng.* **14** 173-204.

Voyiadjis G.Z. and F.H. Abed, 2005, Effect of dislocation density evolution on the thermomechanical response of metals with different crystal structures at low and high strain rates and temperatures, *Archives of Mechanics* **57** 4 299-343.

Vreeland J. and K.M. Jassby, 1971, Temperature dependent viscous drag in close-packed metals, *Materials Science and Engineering* **7** 95-102.

Vuoristo T., Effect of strain rate on the deformation behavior of dual phase steels and particle reinforced polymer composites, PhD thesis, Tampere University of Technology, Tampere, 2004.

Warren T.L. and M.J. Forrestal, 2009, Comments on the effect of radial inertia in the Kolsky bar test for an incompressible material, *Experimental Mechanics*.

Wu X, X. Pan, J.C. Mabon, M. Li and J.F. Stubbins, 2006, The role of deformation mechanisms in flow localization of 316L stainless steel, *Journal of Nuclear Materials* **356** 70-77.

Xiao G.H., N.R. Tao and K. Lu, 2008, Effects of strain, strain rate and temperature on deformation twinning in Cu-Zn alloy, *Scripta Materialia* **59** 975-978.

Zerilli A. and R.W. Armstrong, 1992, The effect of dislocation drag on the stress-strain behavior of FCC metals, *Acta Metallurgica et Materialia* **40** 1803-1808.

Zerilli F.J. and R.W. Armstrong, 1987, Dislocation-mechanics-based constitutive relations for material dynamic calculations, *Journal of Applied Physics* **61** 1816-1825.

Özel T. and T. Altan, 2000, Determination of workpiece flow stress and friction at the chip-tool contact for high-speed cutting, *International Journal of Machine Tools & Manufacture* **40** 133-152.